Methods and Applications of Extreme Ultraviolet Multi-Wavelength Ptychography in Nanoscale Imaging

Fengling Zhang

promotor:	prof.dr. S.M. Witte
copromotor:	prof.dr. K.S.E. Eikema
promotiecommissie:	prof.dr. M.L. Groot prof.dr. A.J. den Boef dr. A. Grubisic-Cabo dr. S.F. Pereira dr. G.S.M. Jansen

The work described in this thesis was carried out at the Advanced Research Center for Nanolithography (ARCNL), a public-private partnership between the University of Amsterdam (UvA), the Vrije Universiteit Amsterdam (VU), the University of Groningen (RUG), the Netherlands Organisation for Scientific Research (NWO), and the semiconductor equipment manufacturer ASML. Funding for this research was provided by the European Research Council (ERC-CoG project 3D-VIEW, 864016).

Contents

— List of Symbols & Abbreviations

NA	Numerical Aperture
EUV	Extreme UltraViolet source
CDI	Coherent Diffractive Imaging
PIM	Ptychographical Information Multiplexing
SXR	Soft X-Ray
HHG	High Harmonic Generation
OPCPA	Optical Parametric Chirped-Pulse Amplification
OAM	Orbital Angular Momentum
SPM	Self-Phase Modulation
GDD	Group Delay Despersion
PIE	Ptychographic Iterative Engine
PWFS	Ptychographic Wavefront Sensor
AFM	Atomic Force Microscopy
SEM	Scanning Electron Microscopy
TEM	Transmission Electron Microscopy
FRC	Fourier Ring Correlation
FTH	Fourier-Transform Holography
FTS	Fourier-Transform Spectroscopy
FTSH	Fourier-Transform Spectroscopic Holography

Chapter 1

Introduction

1.1 From microscopy to computational imaging

1.1.1 Diffraction limit

Photolithography is the core process in miniaturization of semiconductor devices, directly determining both the process node and performance level of the chip [1, 2]. The resolution of photolithography systems is fundamentally determined by the diffraction limit, as described by Abbe's resolution theory [3], which defines the minimum resolvable feature size of an optical system as:

$$d = \frac{\lambda}{2NA} \tag{1.1}$$

where λ is the wavelength of the light source and NA is the numerical aperture of the imaging system. The critical challenge in photolithography lies in achieving higher resolution, which requires either shorter illumination wavelengths or higher numerical apertures.

The development of EUV lithography, utilizing laser-produced plasma source with 13.5 nm wavelength, represents a major milestone in the progression of semiconductor manufacturing, enabling the large-scale production of integrated circuits at process nodes of 5 nm and even down to 3 nm [4]. However, the implementation of EUV lithography introduces significant challenges, including the requirement for specialized materials and optical components that are compatible with such short wavelengths, as well as increased complexity in inspection and metrology techniques.

As semiconductor devices continue to scale down in size and increasingly adopt three-dimensional architectures, the diffraction limit presents crucial challenges for semiconductor metrology, such as optical inspection technologies. As shown in Fig. 1.1, the critical dimensions and overlay requirements have reached values well below the resolution limits of conventional optical microscopy, as well as the demand for three-dimensional imaging. In response to these limitations, the semiconductor research community has explored

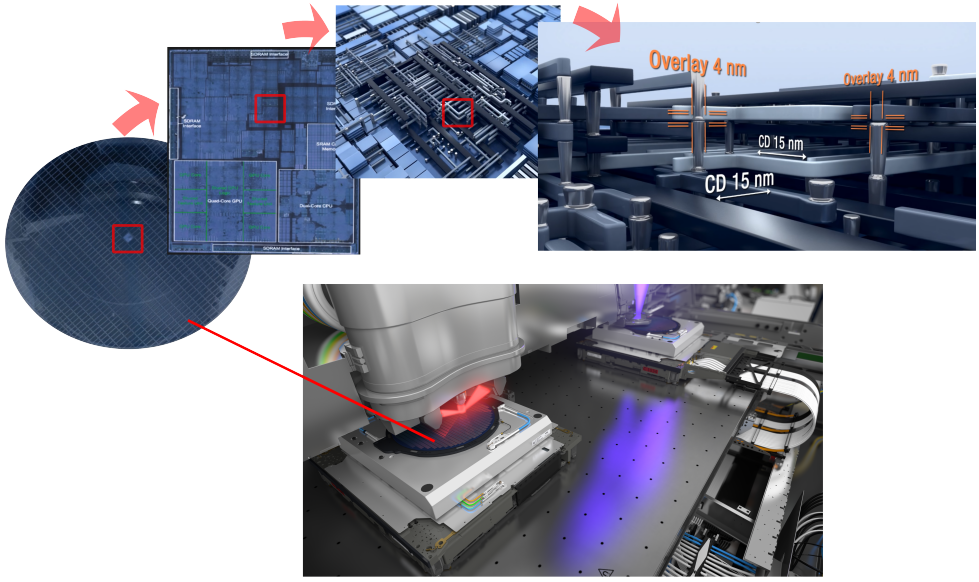

Figure 1.1: A wafer is measured before exposure inside ASML NXE3400. And, a close look at a modern CPU chip. The construction of this chip is simplified on the close look drawing. Silicon integrated circuit layers of various materials are printed on top of each other and the product quality is determined by parameters like overlay (OV) and critical demension (CD). Illustrations by ASML.

advanced measurement solutions to meet the strict requirements of the International Technology Roadmap for Semiconductors (ITRS) and Integrated Device Manufacturers (IDM) [5]. Beyond limitations in photolithography pattering, the diffraction limit also challenges the accuracy and reliability of inspection and metrology at advanced technology nodes. The work presented in this thesis is motivated by the constraints imposed by the diffraction limit, aiming to explore the development and application of EUV lensless imaging.

1.1.2 Emergence of lensless imaging

The development of semiconductor technology, nanoscience, and quantum technology has pushed the boundaries of optical microscopy. Modern applications now require not only nanoscale resolution for complex three-dimensional (3D) structures but also the capability to monitor their physical, chemical, and quantum properties dynamically.

Traditional high-resolution imaging techniques depend on sophisticated and expensive optical lens systems, and are usually supplemented by high-precision 3D scanning mechanisms. These approaches face several significant limitations: (1) The numerical

aperture of the imaging optics limits the acquisition of high-spatial frequency information, thereby limiting imaging resolution [6]; (2) Overcoming the inherent aberrations of optical systems requires considerable cost and complexity in system design [7]; (3) Because the frequency of the optical field reaches the petahertz range, conventional photodetectors cannot respond to rapid oscillations of the electromagnetic field, and only record intensity information. As a result, phase information is lost, which prevents direct acquisition of 3D information of the sample.

Various strategies have been developed to overcome the resolution limitations of conventional imaging systems. One approach involves increasing the effective numerical aperture by employing liquid or immersion lenses composed of high-refractive or negative-refractive index materials [8, 9]. Another strategy utilizes short-wavelength illumination, such as in X-ray microscopy [10]. Additionally, a series of advanced optical imaging techniques has been developed to go beyond the classical diffraction limit, such as stimulated emission depletion microscopy (STED)[11], scanning near-field optical microscopy (SNOM)[12], and stochastic optical reconstruction microscopy (STORM)[13]. While these methods offer sub-diffraction-limited resolution, most rely on fluorescence labeling, such as STED and STORM, which limits their applicability in non-biological sample like semiconductor metrology. Although SNOM does not require fluorescence, it relies on near-field scanning with a nanoscale tip or fiber, resulting in slow acquisition and requiring complex scanning mechanisms. Moreover, techniques such as two-photon and multi-photon microscopy[14, 15], while valuable for deep tissue imaging, do not fundamentally surpass the diffraction limit and also depend on fluorescence excitation. Consequently, these methods face significant limitations in non-invasive, label-free, and high-throughput applications in semiconductor inspection.

In order to extend imaging application into semiconductor fields, coherent diffraction imaging (CDI) [16, 17] offers a simpler and more accessible solution. CDI is a lensless imaging system, and reconstructs both the amplitude and phase of an object from these coherent diffraction patterns. The resulting images are free of aberrations, with resolution limited only by the wavelength of the incident radiation and the spatial frequency of the diffracted waves. Therefore, the resolution of CDI imaging systems can be easily improved by reducing the sample-to-detector distance, expanding the detector size to enhance the numerical aperture, and employing light sources with short wavelength. This implies that CDI can achieve resolution at the diffraction limit level without sophisticated or expensive optical components.

1.2 High-resolution computational imaging

1.2.1 Multidisciplinary applications

Short wavelength radiation in the EUV and soft x-ray spectral regions provides significant advantages for CDI [18–20]. Especially, coherent short wavelength sources based on high-order harmonic generation (HHG) have recently gained attention [21, 22]. With

wavelengths ranging from a few to several tens of nanometers, CDI enables spatial resolutions at the nanometer scale. Moreover, penetration depths in solids in EUV regime enable nondestructive imaging of underlying structures of micrometer thick objects [23]. The presence of element-specific absorption edges further enables high-contrast imaging without the need for external staining or labeling. When combined with quantitative, phase-sensitive reconstruction algorithms, these methods can even facilitate material identification at the nanoscale. This section provides an overview of the development and application of diffractive imaging techniques in EUV region.

In 2007, Sandberg et al. first applied 29 nm HHG source for CDI experiments [24], achieving a spatial resolution of 214 nm. Over the past two decades, extensive experimental studies have demonstrated the feasibility of CDI with HHG illumination, showing its potential for high-resolution imaging. A major advantage of CDI is the ability to perform single-shot diffractive imaging by capturing the diffraction pattern before the sample is destroyed [25, 26]. Furthermore, the use of plane-wave illumination ensures that the diffraction pattern remains translation invariant with the sample, greatly simplifying the sample alignment process during image reconstruction. However, CDI is inherently constrained by the need for isolated objects or a finite illumination beam to define the sample size [27, 28]. The convergence of the CDI iterative phase retrieval algorithm also remains a persistent challenge.

Fourier transform holography (FTH) [29] is a lensless imaging technique closely related to CDI. By recording the interference pattern between the wave scattered by a sample and the reference wave originating from a source in the same plane, FTH enables image reconstruction through a single Fourier transform of the hologram. Unlike CDI, which relies on iterative phase retrieval algorithms, FTH achieves direct reconstruction. This approach enhances robustness and simplifies the imaging process, particularly for applications requiring rapid or damage-free imaging. Moreover, FTH can be integrated with CDI to enhance object field reconstruction. A common approach employs employs FTH to generate an initial low-resolution estimate of the object field, which serves as a starting point for iterative refinement using CDI algorithms [17, 30]. For example, in 2017, Kfir et al. [31] employed circularly polarized HHG to perform FTH-assisted CDI imaging of a multilayer Co/Pd magnetic film, successfully resolving its worm-like magnetic domain structure. In 2021, they incorporated pump–probe techniques into this magnetic imaging framework [32], enabling the observation of the magnetic dynamics under femtosecond laser excitation.

Compared to traditional CDI and FTH, ptychography has advanced rapidly due to its high fidelity and high robustness [18–20, 22]. By recording diffraction patterns at multiple overlapping illumination positions across the sample, ptychography introduces strong redundancy to ensure the uniqueness and stability of phase retrieval solutions. This redundancy is critical for overcoming the convergence instability inherent in CDI and the precise reference wave alignment required by FTH, making ptychography a versatile tool for high-resolution imaging. In 2020, Baksh et al. introduced the Orthogonal Probe Relaxation (OPR) method to address probe instability in ptychographic reconstruction [33]. This method applies singular value decomposition (SVD) to to extract dominant

orthogonal modes from the set of probe functions across all scan positions, projecting them onto a reduced orthogonal basis after each iteration of the ptychographic engine. The OPR technique has been successfully applied to biological imaging, including the high-resolution visualization of pyramidal neurons in the mouse hippocampus [34].

Illumination with a commonly employed Gaussian beam profile often produces dominant zeroth-order diffraction, and in the case of periodic samples, the first-order diffraction components can also be strong. Due to the limited dynamic range of typical detectors, avoiding overexposure of these low-order diffraction spots often leads to a significant suppression of high-order diffraction signals. In contrast, structured illumination distributes the far-field diffraction energy more uniformly by reducing central intensity concentration, enabling the acquisition of high signal-to-noise ratio data through extended exposure times without detector saturation. Structured illumination can be combined with HHG ptychography as well. For instance, using a spiral phase mask impart orbital angular momentum (OAM) to the high-harmonic beam [35–37]. The resulting structured illumination pattern significantly enhanced imaging performance. By integrating the OPR method with mixed-state ptychographic algorithms [38], researchers successfully reconstructed images of solid-state memory circuits and quantified material composition using scattering quotient analysis [35]. Subsequently, the same methodology has also been extended to biological imaging, facilitating high-resolution analysis of samples such as Aspergillus nidulans and Escherichia coli [39, 40].

In 2015, Zhang et al. [41] first performed HHG reflective ptychography experiments, addressing the curvature of diffraction patterns induced by oblique incidence through a tilted-plane correction model. They successfully reconstructed the three-dimensional surface topographies with a spatial resolution of 10 nm vertically and 25 nm horizontally. Notably, the superior vertical resolution was attributed to the high sensitivity of the reconstructed object phase to height variations. Building on this, Karl et al. [42] integrated HHG reflective ptychography with pump-probe techniques to investigate the dynamic propagation of acoustic waves in nanoantenna arrays, advancing the study of time-dependent nanoscale phenomena. Tanksalvala et al. [43, 44] utilized reflective ptychography to map the thickness distribution of chemically etched electronic device layers with a precision of 0.3 nm. By varying incident angles during scanning, they resolved doping concentration variations across device components, demonstrating the technique's versatility in material characterization [43]. Most recently, Lu et al. [45] even applied this reflective ptychographic imaging to characterize and calibrate surface defects in multilayer mirror systems.

In recent years, ptychographical information multiplexing (PIM) [46] has been used for broadband EUV ptychography, demonstrating that spectroscopic sample information can be obtained from a single ptychography measurement [47, 48]. Furthermore, PIM enables high-resolution retrieval of the spectrally resolved illumination wavefront [49]. For instance, the PIM algorithm has been employed to investigate the spatiotemporal properties of HHG beams [49–51].

We highlighted several milestones of EUV imaging techniques in transmission imaging,

reflection imaging, and wavefront sensing. Nevertheless, numerous promising developments and applications remain to be explored in the future. A summary of prospective directions is provided in Fig 1.2.

Transmission ptychography is closely tied to specific material resonances and spectral transmission windows. For example, the EUV transmission windows of lithium and silicon facilitate micrometer-scale penetration depths, making this technique well-suited for characterizing lithium- and silicon-based battery materials [52]. Additionally, the spectral region known as the water window provides unique opportunities for high-resolution imaging of hydrated and live biological specimens, enhancing the study of biological structures in their native state [34, 39, 53, 54].

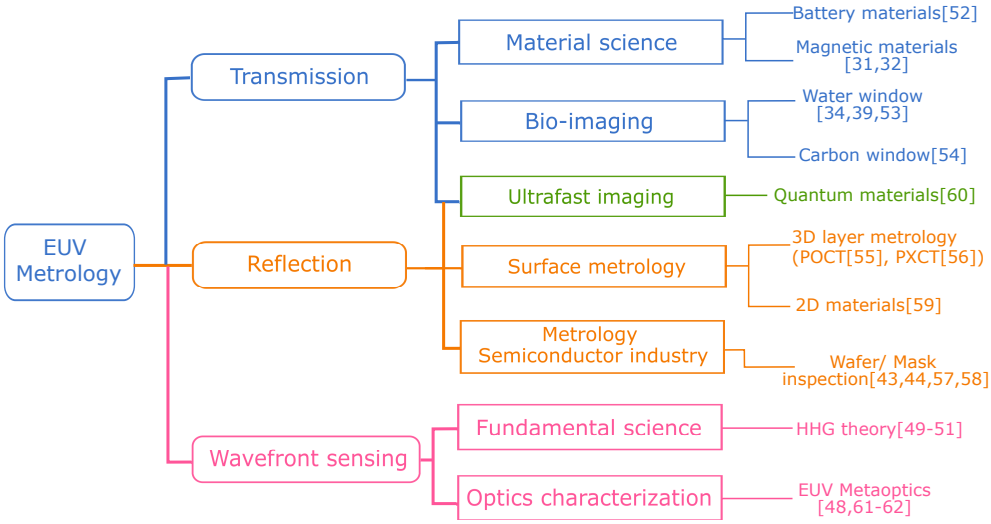

Figure 1.2: Schematic illustration of applications of coherent EUV metrology. Future applications are divided into transmission, reflection, and wavefront measurements.

In reflection geometry, EUV radiation demonstrates superior sensitivity to surface parameters, including topography [55, 56], multilayer structure [43, 44, 57], roughness [58], and compositional variation [43]. Coherent EUV imaging at the nanoscale also provides an experimental platform for validating theoretical models in solid-state physics and advancing the characterization of two-dimensional materials [59], and spatially heterogeneous quantum systems [60].

For wavefront sensing applications, ptychography offers precise characterization and optimization of optical components, including broadband diffractive optical elements [48, 61] and, potentially, innovative high-NA EUV meta-optics [62].

1.2.2 Challenges in EUV-based ptychography

EUV ptychography has emerged as a new force in the field of microscopic imaging. However, the practical implementation faces significant challenges that must be addressed to realize its full potential:

1) Achieving a bright and stable EUV illumination source is critical for high-quality ptychographic reconstructions. The illumination must maintain consistent power, position, and wavefront to produce accurate diffraction patterns. Tabletop EUV sources, often based on HHG, struggle to provide the necessary brightness and stability compared to large-scale facilities like synchrotrons or free electron lasers, limiting reliability and reproducibility.

2) High-quality ptychographic reconstructions critically depend on highly structured illumination beams, which enhance the information content of the recorded diffraction patterns. However, the use of such structured beams is often accompanied by a significant reduction in photon flux, posing challenges for signal-to-noise ratio and imaging throughput.

3) EUV ptychography is ideally suited for obtaining material-specific and thickness information with high resolution. Phase and amplitude noise limit sensitivity to internal structural changes in multilayered structures.

4) HHG sources are intrinsically broadband, consisting of discrete harmonic orders or a quasi-continuous wavelength spectrum. This broadband nature poses challenges for lensless imaging, as it limits temporal coherence, resulting in blurred diffraction patterns and degraded spatial resolution.

1.3 Thesis outline

The thesis is structured as follows. Chapter 2 introduces the principles and experimental setups for EUV ptychographic imaging, emphasizing the role of structured illumination and element-specific contrast for enhanced resolution and material analysis. Chapter 3 details the development of post-compression techniques for high-intensity ultrashort laser pulses, utilizing nonlinear spectral broadening to achieve significant pulse shortening while preserving beam quality, thereby preparing the driving laser for efficient HHG. Chapter 4 addresses challenges in broadband EUV ptychography, demonstrating how spatial diversity in polychromatic illumination improves reconstruction quality for multi-wavelength imaging. Chapter 5 focuses on spectrally resolved lensless imaging of dispersive samples, comparing diffractive shearing interferometry and ptychography to extract material composition and layer thickness with high precision. Finally, Chapter 6 presents an interferometric approach integrating Fourier transform spectroscopy with holography, leveraging phase-locked HHG pulses to achieve rapid, high-resolution spectro-microscopic imaging of nanostructured materials.

Chapter 2

Imaging using Coherent Extreme Ultraviolet Radiation: Principles and Experimental Methods

This chapter introduces nanoscale coherent diffraction imaging techniques based on HHG sources in the EUV and soft X-ray spectral ranges. We start with the principles and experimental setup for generating coherent EUV radiation using table-top HHG systems driven by high-intensity femtosecond lasers. Next, we outline the fundamentals of ptychographic algorithms, which offer robust solutions to the phase problem, and discuss how structured illumination improves algorithmic convergence and spatial resolution. Furthermore, we show the extraordinary ability of EUV imaging in enabling element-specific contrast and material analysis, due to the light-matter interaction in the short-wavelength region. Finally, we show the design and key components of the EUV ptychographic imaging setup, with a focus on the diffraction pattern acquisition system in vacuum, as well as the collection and processing of both transmission and reflection experimental data.

2.1 EUV source: high harmonic generation

2.1.1 Coherent EUV radiation via high harmonic generation

In comparison to conventional large-scale scientific X-ray sources, such as synchrotrons and X-ray free-electron lasers, HHG light sources offer the advantages of lower cost, simpler implementation, and compact size [63]. In order to achieve high-speed, high-resolution CDI that is readily adoptable, the ideal illumination source must possess key characteristics, including a short wavelength, high coherence, high brightness, compact design, and user-friendly operation. Early CDI relied on synchrotron radiation sources, which suffered from low imaging efficiency and limited resolution [17, 64]. Subsequent advancements in synchrotron radiation sources and the development of X-ray free-electron lasers significantly improved these limitations [20, 56]. However, these large-scale facili-

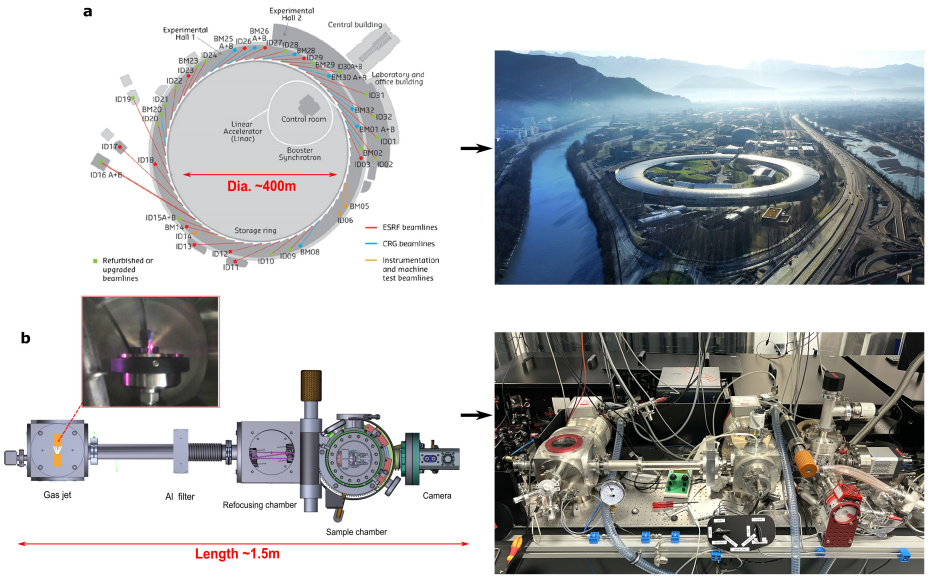

Figure 2.1: (a) ESRF accelerator complex and beam lines (image courtesy of the ESRF communication group). (b) Our table-top HHG-EUV source.

ties are structurally complex, physically huge, costly, and require long construction periods. Moreover, their limited capacity to accommodate multiple simultaneous users substantially restricts the widespread adoption and application of the advanced CDI technology. Figure 2.1a shows the design and a photograph of the European Synchrotron Radiation Facility (ESRF) in France [65]. The facility has a diameter of approximately 400 m and an annual operating budget of around 100 million euros. In contrast, Figure 2.1b shows a table-top HHG laser source designed in our laboratory, only occupying an optical table of approximately 6 x 1.5 m in length. Compared to large-scale facilities, the table-top

HHG source greatly reduces cost, size, and energy consumption. In addition, the HHG light source can generate beams in the spectral range of 1-200 nm, surpassing large-scale light sources in coherence and stability, with optical power in certain wavelength bands approaching levels comparable to synchrotron radiation facilities and X-ray free-electron lasers [32].

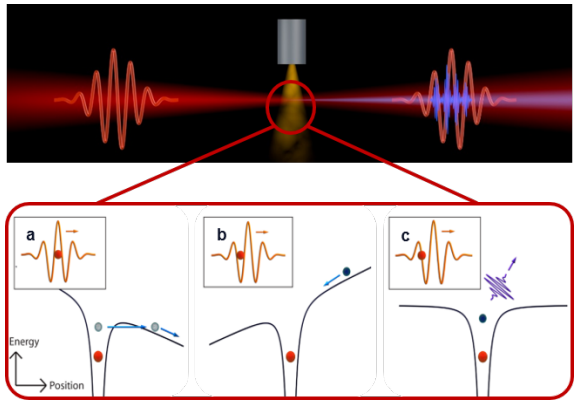

Figure 2.2: The illustration of the three-step model. (a) Tunnel ionization. (b) Acceleration by the laser field. (c) Recombination and photon emission.

HHG was first demonstrated in 1987 by McPherson et al. [66], who used infrared picosecond pulses focused into a noble gas to produce short-wavelength radiation. Initially, the phenomenon received limited attention due to the absence of a clear theoretical framework. In 1993, Krause et al. [67] and Corkum [68] provided a semiclassical model based on atomic ionization dynamics, now widely known as the "three-step model", illustrated in Fig. 2.2:

a. Tunnel ionization: The Coulomb potential of the atom is modified by the laser field, creating a suppressed and asymmetric potential barrier. Then, an electron can tunnel through this barrier out of the atom. This process is described quantitatively by the Ammosov–Delone–Krainov (ADK) theory [69].
b. Acceleration by the laser field: Once ionized, the electron oscillates and accelerates in the laser field, gaining additional kinetic energy. The electron's trajectory depends on the phase of the laser field at the moment of ionization. Electrons ionized at different times follow distinct trajectories. Some electrons drift away from the parent ion and do not return, while others, ionized at specific phases, are driven back toward the parent ion when the laser field reverses direction.
c. Recombination and photon emission: As the laser field reverses direction, certain electrons are accelerated back to the parent ion. During recombination, the electron releases its accumulated kinetic energy plus the ionization

potential of the atom as a high-energy photon. These photons correspond to odd harmonics of the fundamental laser frequency due to the symmetry of the laser field and the atomic potential.

Numerical simulations indicate approximately one-third of ionized electrons recombine with the parent ion. The actual probability of recombination, however, is governed by additional factors such as the energy-dependent recombination cross section [68]. The maximum kinetic energy is $3.17U_p$, where the ponderomotive energy U_p is defined as:

$$U_p = \frac{e^2E^2}{4m_e\omega_0^2} \tag{2.1}$$

Here, E is the peak electric field amplitude of the linearly polarized laser, m_e is the electron mass, and ω_0 is the angular frequency of the driving laser. The three-step model describes the HHG process with high spatial coherence, arising from the high-order nonlinear interaction between intense laser fields and atomic electrons. The model also successfully explains the the distinctive features of the HHG spectrum. The spectrum is characterized by two primary regions: a plateau region, where harmonic conversion efficiency remains nearly constant across orders, and a cutoff region, where efficiency diminishes rapidly with increasing harmonic order. The cutoff frequency ω_c is given by:

$$h\omega_c \approx I_p + 3.17U_p \tag{2.2}$$

where I_p is the ionization potential.

The three-step model shows the single atom response, which depends on the driving laser intensity and wavelength [70], and on the atomic species. To some extent, the efficiency of the single atom response can be boosted by multicolour schemes, at the cost of more complex optical setups [71, 72]. While the three-step model captures the microscopic mechanism of HHG, efficient HHG in practice requires careful control of macroscopic propagation in a gas medium composed of many atoms. To enhance the overall conversion efficiency and produce HHG beams with low divergence and high spatial coherence, both microscopic and macroscopic processes must be carefully managed.

A key macroscopic factor is phase matching, which ensures constructive interference of harmonics generated at different positions in the medium. Optimizing the focusing geometry, gas pressure, and interaction length is essential to maximize conversion efficiency and achieve high spatial coherence and low beam divergence. In addition to phase matching, system design must also account for EUV absorption in the gas medium and the material-specific limits on the achievable HHG wavelength range [73, 74].

To optimize phase matching for HHG and produce coherent X-ray radiation, various techniques have been explored, including high-pressure gas jets [75], low-pressure cells [76], semi-infinite cells [77] or capillaries [78], and gas-filled waveguides [79]. Among these, free-space focusing drive laser into gas jet stands out as the simplest to implement experimentally and is employed in our laboratory. It is worth noting that this approach

confines the peak intensity of laser to a narrow region around the focal point, limiting HHG production to a similarly restricted spatial range.

We adapt a series of targeted strategies to improve phase matching in our case. For enhancing conversion efficiency specifically, we utilize a compact, high-pressure gas jet (∼1 mm length, ∼5–6 bar), as illustrated in the inset of Fig. 2.1b. The efficiency of HHG is limited by the intensity and pulse duration of driving laser. These factors determine the cutoff energy, as given by Eq. 2.2, beyond which harmonic yield drops significantly. Additionally, exceeding the critical ionization threshold inhibits effective phase matching [80]. By employing short, high-intensity pulses, high-photon-energy harmonics can be generated, even with near-infrared driving wavelengths, through a mechanism known as non-adiabatic self-phase matching [63].

In the following section, we present the high-intensity femtosecond laser systems employed in our lab to drive HHG with optimized conversion efficiency, stable output power and beam profile, as well as high spatial and temporal coherence essential for coherent imaging applications.

2.1.2 High-intensity femtosecond laser systems

High peak power ultrafast sources are key enabling tools for numerous disciplines ranging from fundamental science to medical applications [81]. High-intensity femtosecond laser systems are essential to drive the high-harmonic process to make short wavelength available in lab-scale. Simultaneously amplifying ultrashort pulses and shortening pulse duration represent a major challenge [82]. The most prevailing ultrashort high-power lasers are titanium:sapphire (Ti: Sa) [83] and ytterbium (Yb) ion-doped lasers [84, 85]. The Ti:Sa lasers generate extremely broadband pulse, which have been prevailing since the 1990s for sub-50-fs pulse durations and high intensity applications [83, 86]. Compared to Ti: Sa lasers, lasers using Yb-doped gain media are found to have better average power scalability but a narrower emission bandwidth [84, 87].

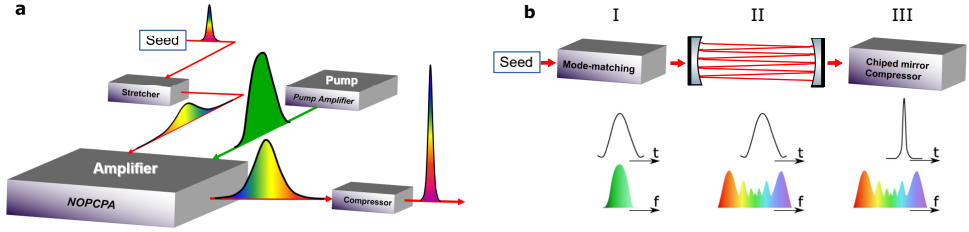

Figure 2.3: (a) Concept of amplifying seed lasers based on OPCPA. (b) Concept of the most common implementation of multi-pass cells with bulk or gas nonlinear medium for spectral broadening. At each step, the frequency and time domain profiles are illustrated. Step I, mode-matching; step II, spectral broadening in a nonlinear medium inside the multipass cell; step III, temporal compression using chirped mirrors or transmission gratings.

There are commonly two methods employed to produce high peak and average power laser pulses with a duration shorter than achievable with the laser bandwidth itself: optical parametric chirped-pulse amplification (OPCPA) and post-compression, as shown in Fig. 2.3. First, OPCPA offers a method to amplify a super-continuum pulse over a large bandwidth by pumping it with narrow-band but high-energy laser pulses [81, 88]. The stretched seed beam is temporally and spatially overlapped with the high-intensity pump beam inside a birefringent nonlinear optical crystal. Optical parametric amplification (OPA), a key nonlinear process to amplify the stretched seed beam, involves the conversion of the pump laser frequency into pairs of lower "signal" and "idler" photon energy in the nonlinear crystal. Of the lower energy photons, the signal photon matches the photons from the seed oscillator pulses in energy and momentum, while the idler photon carries the excess energy and momentum. This process effectively transfers energy from the pump beam to the seed beam. The second approach is post-compression by nonlinear spectral broadening of a high-energy pulse and subsequent compression using chirped mirrors. Such methods directly broaden the spectral width of the high-power pulses through nonlinear interactions, appealing for power-scaling applications due to its efficiency in reducing losses [89–92]. As most pulse post-compression methods, the multipass cell scheme employs nonlinear self-action effects that occur when high-intensity pulses travel through a medium, leading to spectral broadening via self-phase modulation (SPM). A more detailed discussion of the nonlinear interactions will be given in Chapter 3. Similar to an optical cavity, a Herriott-type multipass cell [93] forms transverse eigenmodes and preserves the Gaussian beam q-parameter of a beam mode matched to the MPC eigenmode. Typical multipass cell setups [94] employed for post-compression resemble in Fig. 2.3b. (I) The laser beam is mode-matched to the eigenmode to ensure identical beam properties per pass through the cell. (II) The beam is coupled to the multipass cell. After the targeted number of round trips has been reached, the spectrally broadened output beam is coupled out via the same scraper or hole in the mirror or via an output-coupling mirror. (III) The Self-phase modulation induced chirp is subsequently removed by an external compressor to obtain a temporally compressed pulse.

Inspired by the CASCADE concept [95], we explore the ability to compress high-energy pulses by loose focusing in noble gas cells to induce nonlinear spectrum broadening, while limiting unwanted nonlinear effects such as self-focusing. Figure 2.4 shows the two-stage post compression setup. Pharos (PH2-06-2000-02-A4-SP, Light Conversion, UAB) is a compact high repetition rate femtosecond laser, which employs directly diode-pumped Yb:KGW (ytterbium doped potassium gadolinium tungstate) as an active medium. The PHAROS laser system delivers 2 mJ, 170 fs at 1030 nm pulses, with a repetition rate of 1 kHz. The 1030 nm pulses are spectrally broadened through two cascade noble gas-filled stages. In the first stage, the pulses are first focused into a 700 mbar argon-filled tube using a curved mirror with a 2.5 m focal length. To compensate for the nonlinear phase accumulated during spectrum broadening, 5 bounces on the chirped mirrors (GDD=-500 fs^2, UltraFast Innovations, CM39) are applied. The resulting 94 fs pulses are refocused using the same optical geometry into the second 700 mbar argon tube for further spectral broadening. Subsequently, six additional bounces on the same chirped mirrors are applied

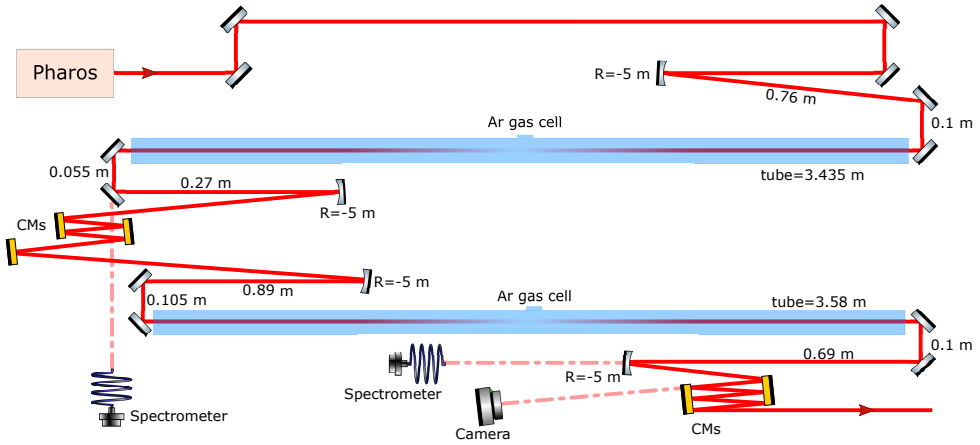

Figure 2.4: Schematic overview of the two-stage post compression setup. The spectrometers measure the spectral broadening after each pass by monitoring the residual transmission through a mirror after each cell.

to further compress the pulses by removing the accumulated nonlinear phase in the time domain, resulting in a pulse duration down to 35 fs.

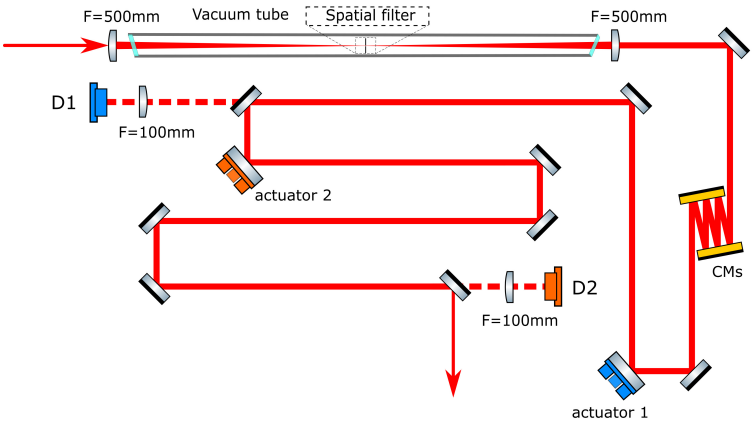

Figure 2.5: The 4-axes stabilization system. The leakage of the beam are focused in to detector D1 and D2 by an f=100 mm lens, and actuator 1 and 2 are two steering mirrors.

Following the CASCADE post-compression stage, a spatial filter with a 200 μm diameter aperture in a 5 mm boron nitride disk is placed at the focus of relay-imaging lenses to refine the beam profile, attenuating approximately 10% of the pulse energy. To ensure sufficient pointing stability of the EUV beam, active stabilization of the driving IR laser is

implemented, achieving a pointing stability better than 1 μrad at the vacuum chamber entrance. A compact laser beam stabilization (MRC systems, GmbH) compensates for undesired fluctuations of the laser beam pointing direction. As shown in Fig. 2.5, the 4-axes system combines two PSD detectors (D1, D2) and two steering mirrors (actuator 1, actuator 2) in order to detect the laser beam at two distant positions. Thereby, both position and direction are fixed. The detectors are both placed behind high-reflection mirrors. They are very sensitive and can work with the leakage behind the mirrors. The advantage is that no additional components are required in the beam path. Detector 1 stabilizes the beam position on actuator 2, while detector D2 ensures the beam's position at a separate point, thus fixing its direction. A closed-loop controller continuously corrects deviations, driving the fast actuators to maintain the laser beam's desired position via the steering mirrors.

2.2 Coherent EUV imaging techniques

2.2.1 Principle of wave propagation and diffraction imaging

Scalar diffraction theory [96] provides a simplified framework for analyzing the propagation and diffraction of light by treating the electromagnetic field as a scalar quantity, neglecting vector properties like polarization. The theory originates from the scalar wave equation and employs the Huygens-Fresnel principle, which asserts that every point on a propagating wavefront can be considered a source of secondary spherical wavelets. The superposition and interference of these wavelets determine the resultant optical field at any observation point, giving rise to the observed diffraction pattern.

Consider the propagation of light field with wavelength λ, from the plane $z = 0$ to a parallel plane at distance z, as shown in Fig 2.6. The field distribution $U(x^{'}, y^{'}, 0)$ incident on the first plane can be considered to be mapped by the propagation phenomenon into a new field distribution $U(x, y, z)$. Under the optical far-field approximation $z >> k(x^{'2} + y^{'2})_{max}/2$, the far-field distribution $U(x, y, z)$ can be expressed by:

$$U(x,y,z) = \frac{e^{ikz}}{i\lambda z} e^{i\frac{k}{2z}(x^2+y^2)} \int U(x^{'}, y^{'}, 0) e^{-i\frac{k}{z}(xx^{'}+yy^{'})} dx^{'} dy^{'} \tag{2.3}$$

Here, the wave number is $k = 2\pi/\lambda$. the observed complex field $U(x, y, z)$ at the destination plane can be expressed as the product of a phase factor and the Fourier transform of the complex field at the source plane. The corresponding frequencies are:

$$k_x = k\frac{x}{z}, k_y = k\frac{y}{z} \tag{2.4}$$

According to the Fraunhofer propagation (Eq 2.3), the complex wavefront function in the detector plane is given by the Fourier transform of the exit surface wave at the sample plane. The exit surface wave is determined by the probe $P(x, y, 0)$ and the sample

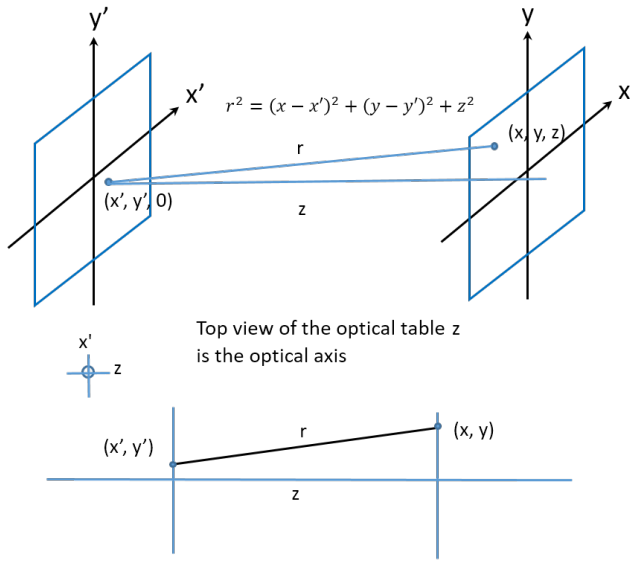

Figure 2.6: Electric field propagation through parallel planes. z is the propagation distance, and $z = 0$ is the source plane.

$O(x, y, 0)$:

$$E(x, y, 0) = P(x, y, 0) \cdot O(x, y, 0) \tag{2.5}$$

By using the Fresnel-Kirchhoff diffraction integral, we can derive the complex amplitude distribution of the optical wavefield $g(u, v, z)$ at the detector (diffraction) plane. In the far-field limit, the integral simplifies significantly and can be approximated by

$$g(u, v, z) = \frac{e^{ikz}}{i\lambda z} e^{i\frac{k}{2z}(u^2+v^2)} \int E(x, y, 0) e^{-i\frac{k}{z}(xu+yv)} dxdy \tag{2.6}$$

Thus, if the full complex amplitude of the diffracted wave $g(u, v, z)$ (both magnitude and phase) were known, we can directly retrieve the wavefield $E(x, y, 0)$ at the source plane via an inverse Fourier transform and subsequently reconstruct the spatial structure of sample $O(x, y, 0) = E(x, y, 0)/P(x, y, 0)$ through Eq. 2.4. However, practical detectors in CDI experiments (e.g. CCDs or CMOSs) measure only the intensity. The phase information, essential for reconstructing the original object, is lost in the measurement. To overcome this, phase retrieval algorithms are employed: they aim to reconstruct the complex diffraction field from the measured intensity distribution by enforcing additional physical or mathematical constraints (e.g., finite support [97], non-negativity [98], known probe characteristics [99]). Through iterative inversion, these methods enable the recovery of both the amplitude and phase of the exit wave, thereby reconstructing the real-space structure

of the sample. The procedure is known as phase retrieval or phase reconstruction.

2.2.2 Principles of the phase problem and ptychography

Detectors only record the intensity, leading to the 'phase problem', a central challenge in CDI, which is addressed using computational phase retrieval algorithms. Holography addresses the phase problem by using the interference between a reference wave and an object wave to capture both the amplitude and phase of the wavefront [100]. In crystallography, the phase problem is equally critical, where discrete diffraction peaks arise from crystalline structures [101]. However, unlike crystallography, CDI and ptychography employ a coherent wave incident on a non-crystalline sample or a confined wave illuminating a crystal, resulting in continuous diffraction intensity rather than discrete peaks.

In order to accurately retrieve phase in CDI, the sampling frequency in each spatial dimension should be at least twice the highest spatial frequency present in the diffraction pattern [102, 103]. The condition, known as the *sampling constraint*. According to autocorrelation theory, the diffraction intensity $I(u, v)$ corresponds to the Fourier transform of the autocorrelation function of the complex wavefield:

$$I(u, v) = \mathcal{F}\{E(x, y) \cdot E^*(x, y)\} \tag{2.7}$$

where $\mathcal{F}$ is the Fourier transform operator. If the sample output wave function is discretized into a $M \times N$ matrix, the resulting autocorrelation matrix expands to $M \times N$ expanded to $(2M - 1) \times (2N - 1)$. When performing the discrete Fourier transform, the (u, v) k-space and the (x, y) real-space must employ an identical number of sampling points, with the real-space potentially padded with zeros. Consequently, each dimension in real-space should incorporate redundancy equivalent to the effective data. For instance, a two-dimensional system necessitates fourfold oversampling, a three-dimensional system requires eightfold oversampling, and higher-dimensional systems follow this pattern accordingly.

Miao et al. [104] introduced the concept of *oversampling*, defining the oversampling ratio σ as the number of measured data points divided by the number of unknowns. When the oversampling rate is $\sigma > 2$, the phase information can, in principle, be uniquely determined. Each unknown value in the complex wavefield consists of two components, amplitude and phase, or real and imaginary parts. Each measured intensity value provides only one real constraint, which is the squared amplitude. The number of measurement points gives the number of equations. A unique solution requires that the number of constraints is at least equal to the number of unknown values:

$$I(u_k) = |F(u_k)|^2 = \frac{1}{N} \left| \sum_{l=1}^{N-1} f(x_l e^{-i2\pi kl/N}) \right|, \quad k = 0, 1..., N-1 \tag{2.8}$$

where $I(u_k)$ is the measured intensity, $f(x_l)$ is the unknown complex wavefield in the real space. Using the discrete Fourier transform in Eq. 2.8 is generally infeasible to solve for N complex numbers from only N positive real numbers. A practical approach involves padding with zeros to extend the number of points to $2N$. This method effectively increases the number of equations, as the values of the added points (zeros) are known, while keeping the number of unknowns constant. Such an approach necessitates an isolated sample, with the boundary of the non-zero region defining the support domain.

Phase reconstruction algorithms in single-shot CDI are performed by iteratively propagating the complex optical field between the sample and detector planes while applying physical constraints in each domain. In Gerchberg–Saxton algorithm [105], the amplitude of probe at the sample plane is assumed to be known, but this is not always realistic in CDI. To address this, the concept of a support constraint [27] was introduced, which defines a finite region where the sample is expected to exist. The support can be refined dynamically using the shrink-wrap algorithm [97]. Under these circumstances, reconstructing the sample necessitates simultaneous recovery of both phase and amplitude. Subsequently, a range of algorithms have been developed to improve reconstruction accuracy and convergence, including Error Reduction (ER) [27, 98], Hybrid Input-Output (HIO) [27, 98, 106], Relaxed Averaged Alternating Reflections (RAAR) [107], and the Difference Map (DM) algorithm [108]. These methods typically start from a random initial guess and alternate projections between the Fourier domain and real space. CDI phase iteration risks converging to local minima, potentially failing to reach the true solution. Therefore, a combination of algorithms is often employed to improve robustness and increase the likelihood of reaching the correct solution.

In 2004, Rodenburg and Faulkner [99] revisited Hoppe's early work and proposed the ptychographic iterative engine (PIE) algorithm. In ptychographic experiment, a coherent probe is scanned across the sample, sequentially illuminating overlapping regions. For each position, the resulting diffraction intensity is recorded. The redundancy introduced by overlapping scans, combined with intensity constraints in the Fourier domain, enables iterative reconstruction of both the sample and probe, typically converging to a unique and accurate solution. The overlap scanning constraint utilizes the overlapping regions between successive illuminations to ensure that the iterative convergence process accurately reconstructs the true sample structure. Similar to the oversampling condition in conventional CDI, repeated illumination effectively increases the number of constraint conditions, equivalent to adding equations, while the number of sample pixels, representing unknown quantities, remains unchanged. Consequently, provided the oversampling rate exceeds a factor of two, the system of equations yields a unique solution. In practice, to account for experimental noise and instability, an overlap of more than 60% between adjacent probe positions is typically required to ensure reliable phase retrieval. By employing ptychography, the requirement for sharp-edge support of object is eliminated, allowing full-field imaging of complex samples. Moreover, the increased redundancy and diversity of information afford higher resolution compared to conventional single-shot CDI, significantly broadening the application range of CDI imaging techniques [109].

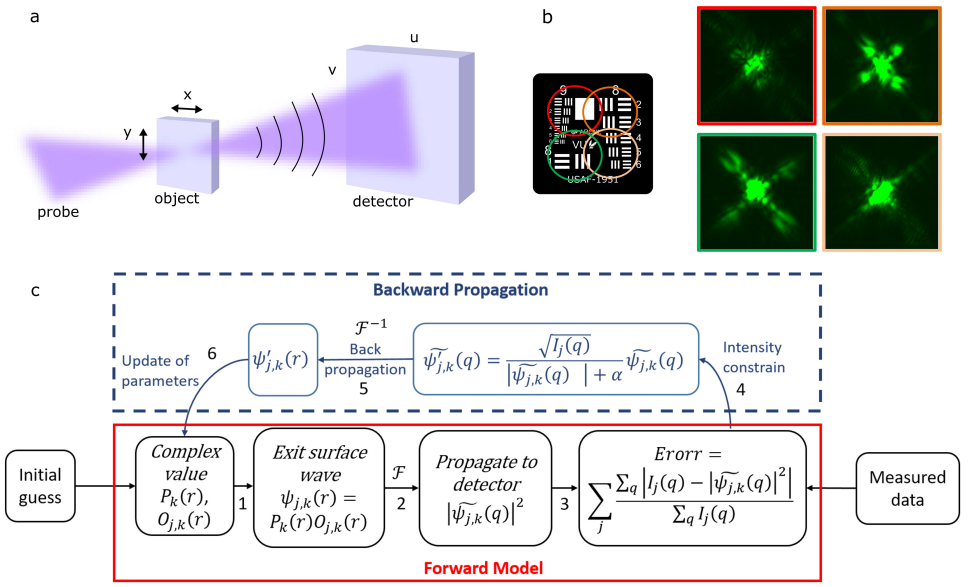

Figure 2.7: The iterative principle of the ptychographic experiment. (a) Experimental setup. (b) Multiple areas on the sample are illuminated sequentially (here four are shown), and the corresponding diffraction patterns are recorded at each position. (c) Flow chart for ptychography algorithms based on the ptychographic iterative engine.

Figure 2.7a shows the typical experimental arrangement of ptychographic experiments: the object O is mounted on a two-dimensional translation stage, and the probe P illuminates the sample through its structure, subsequently the diffracted wavefield reaching the camera. The two-dimensional stage moves in the x-y plane to scan the sample, ensuring overlap between adjacent scan regions and capturing the corresponding diffraction pattern at each position. Figure 2.7b shows the illumination area corresponding to four neighboring scans. During scanning, a sequence of diffraction images tied to specific scan positions is recorded. Once the diffraction patterns are collected, the PIE algorithm reconstructs the lost phase information of both the sample and the optical probe.

In the ptychography reconstruction process, the object $O(r)$ and the probe $P(r)$ are initially estimated, followed by iterative computations shown in Fig. 2.7c. The iteration updates the object $O_{j+1}(r)$ and the probe $P_{j+1}(r)$ for the $(j+1)$-th step based on the j-th workflow as follows:

1. At k-th iteration, compute the exit surface wave $\psi_{j,k}(r)$ at the plane for the j-th probe position:

$$\psi_{j,k}(r) = P_k(r) \cdot O_{j,k}(r) \tag{2.9}$$

where r denotes the real-space coordinates, $O_{j,k}(r)$ is the object wave function at position j and iteration k, and $P_k(r)$ is the probe wave function.

2. Propagate the exit surface wave to the detector plane using a Fourier transform:

$$\tilde{\psi}_{j,k}(q) = \mathcal{F}\{\psi_{j,k}(r)\} \tag{2.10}$$

where q denotes the reciprocal space coordinates (u, v). Note that different propagators can be chosen for numerical calculations depending on the diffraction conditions: Angular spectrum, Fresnel and Fraunhofer propagator [96]. Here, we choose Fraunhofer propagator as a showcase.

3. Calculate an error metric to monitor the convergence behavior of the algorithm:

$$Error = \sum_j \frac{\sum_q |I_j(q) - |\tilde{\psi}_{j,k}(q)|^2|}{\sum_q I_j(q)} \tag{2.11}$$

4. The measured diffraction pattern at the detector is I_j. Apply the intensity constraint to enforce agreement with the measured data:

$$\tilde{\psi}'_{j,k}(q) = \sqrt{I_j(q)} \cdot \frac{\tilde{\psi}_{j,k}(q)}{|\tilde{\psi}_{j,k}(q)| + \alpha} \tag{2.12}$$

where α is a small positive constant (e.g., 10^{-5}) to avoid division by zero, and $\sqrt{I_j(q)}$ replaces the amplitude of $\tilde{\psi}_{j,k}(q)$ while preserving its phase.

5. Back propagate the updated wavefield to the object plane:

$$\psi'_{j,k}(r) = \mathcal{F}^{-1}\{\tilde{\psi}_{j,k}(q)\} \tag{2.13}$$

where $\mathcal{F}^{-1}$ is the inverse Fourier transform.

6. The loss function $L = |\psi - PO|^2 = (\psi - PO)(\psi^* - P^*O^*)$ is defined at object plane. The updated object $O'_{j,k}(r)$ and $P'_k(r)$ can be derived as [110]:

$$O'_{j,k}(r) = O_{j,k}(r) + \beta \frac{P^*_k(r)(\psi'_{j,k}(r) - \psi_{j,k}(r))}{max(|P^*_k(r)|^2)} \tag{2.14}$$

$$P'_k(r) = P_k(r) + \beta \frac{O^*_{j,k}(r)(\psi'_{j,k}(r) - \psi_{j,k}(r))}{max(|O^*_{j,k}(r)|^2)} \tag{2.15}$$

where $0 < \beta < 1$ is the update step size, and we set 0.25 practically.

Employing ptychography to generate substantial data redundancy significantly enhances convergence speed, reduces noise interference, and enables the phase recovery

algorithm to achieve remarkable success. As a result, CDI has developed rapidly into thick samples [111] and even super-resolution [112].

2.2.3 Structured illumination imaging

Structured illumination has become a highly effective approach to improve ptychographic imaging performance, particularly in the EUV and soft X-ray spectral ranges [35–37, 39, 48, 54, 61, 113, 114]. In conventional ptychography setups [99, 115], the detector is placed close to the sample to achieve a large numerical aperture and thus high spatial resolution. However, the use of reflective optics to focus EUV typically results in a limited illumination NA.

Recent studies have demonstrated that using a structured probe, as opposed to traditional Gaussian or flat illumination, significantly improves robustness and convergence of phase retrieval algorithms. Experimentally, placing nanostructured binary masks [35, 39, 48, 54, 61, 116] or increasing divergence [114] in the beam path significantly enhances the quality and resolution of the ptychographic reconstructions. Furthermore, using the OAM beam [36, 37] proves especially valuable for periodic or low-diversity samples, such as semiconductor devices or EUV lithography masks, where uniform illumination frequently results in reconstruction artifacts due to limited diversity in the recorded diffraction patterns. Phase-shifting diffusers [35] are particularly promising due to their photon efficiency and ability to suppress strong zero-order diffraction.

From a mathematical perspective, the probe and object contribute symmetrically to the ptychography, yet the probe uniquely influences every diffraction pattern during the scan. Therefore, a probe exhibiting high spatial diversity, featuring randomized phase and amplitude, can effectively address gaps in the diffraction data, compensating for detector limitations such as missing pixels. In contrast, a uniform flat wavefront results in localized and narrow far-field diffraction patterns, limiting the information coupling between adjacent scan positions. In a coherent imaging system, the imaging process is represented in the the spatial domain as the direct product of the sample and the probe, and in the frequency domain as the convolution between the Fourier spectrum of the sample and the illumination. The concept of structured illumination is shown in Fig. 2.8, where a binary object is illuminated using a 632 nm beam, comparing a smooth Gaussian intensity distribution with a structured grid-like pattern. The far field diffraction pattern reveals that the structured beam introduces high spatial frequency components, making use of the full field of camera.

The advantages of structured illumination are twofold. First, a probe with a wide angular spectrum generates diffraction patterns that are more uniformly spread across the detector, relaxing dynamic range requirements and enabling longer exposure times without saturating low-order diffraction parts. Second, the spatial complexity of the illumination introduces significant variations in the recorded diffraction data during probe scanning, increasing the information content and improving convergence of iterative phase retrieval algorithms. Detailed discussion will be provided in in Chapter 4.

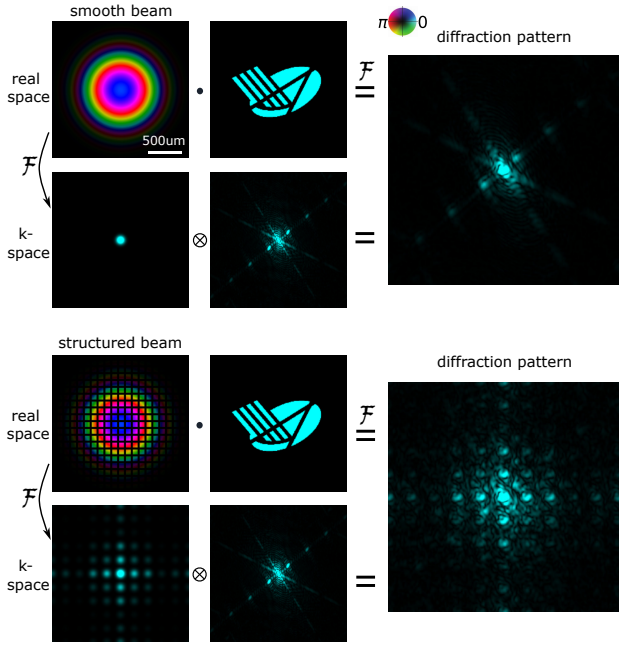

Figure 2.8: Comparison of CDI systems in the spatial and frequency domain using smooth and structured beam, where ⊗ denotes convolution operation. The diffraction patterns are in a saturated dynamic range in order to highlight the differences at higher angles.

Structured illumination proves particularly beneficial for imaging periodic structures [36]. Under conventional illumination, the strong zero-order and first-order diffraction peaks can dominate the dynamic range of the detector, making it difficult to capture high-order signals without saturation. By redistributing the diffraction energy across a broader angular spectrum, structured illumination reduces this central intensity dominance, enabling higher signal-to-noise ratios for high-spatial-frequency features.

In summary, structured illumination in EUV ptychography offers significant benefits in terms of dynamic range optimization, algorithmic convergence, and imaging fidelity.

2.2.4 Light-matter interactions and towards 3D imaging

Detecting and imaging structure underneath opaque materials is essential for nanoscience and nanotechnology. However, most imaging methods cannot be used for nondestructive, sub-surface imaging beyond 50 nm depths. Visible microscopy only image the surfaces of metallic samples. Back-scattered electron (BSE) and SEM can image buried features using high electron energies to enhance penetration depth [117]. However, these methods are constrained by the limited penetration depth of the samples and by sample damage induced through electron interactions. Fortunately, short wavelength EUV and soft X-ray

beams can penetrate materials, enabling nondestructive, non-contact imaging of buried structures and providing depth-dependent compositional information [35, 43, 44].

In dielectric or semiconductor materials, significant absorption does not occur when the photon energy is smaller the band gap of the material. Within the visible spectrum, dielectrics are recognized as materials transparent to radiation, which makes them essential for optics, particularly in optical coatings [118]. The origin of the transparency lies in the electronic band structure of crystalline dielectrics, where less-bound electrons occupy the valence band, and the conduction band remains unfilled [23]. Besides, dielectric materials such as SiO_2, can also exhibit partial transparency at short wavelengths (down to around 12 nm), due to the absence of strong resonances in the atomic structure of silicon and oxygen in this spectral region [119].

For metals, there is no gap between valence and conduction bands. The less-bound electrons are shared by all atoms. According to the free-electron Drude model [120], the plasma frequency serves as a critical frequency turning point between reflective and relatively transparent behavior. When the frequency of light exceeds the plasma frequency, the interaction between light and the metal diminishes significantly. Aluminum serves as an effective transmittance filter due to its plasma frequency at approximately 83.5 nm. Al reflects efficiently at wavelengths longer than 83.5 nm and has a relatively low absorption below 83.5 nm down to the Al $L_{2,3}$ edge at 17.2 nm, so that it can be used as a transmittance filter to selectively pass EUV light within 17.2 nm to 83.5 nm range.

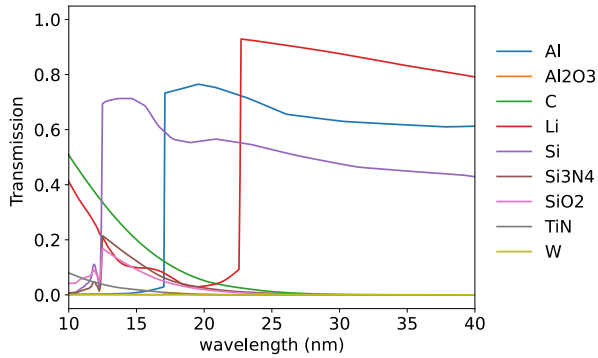

Figure 2.9: Normal incidence transmission of materials with 200 nm thickness in the EUV region.

The complex refractive index $\tilde{n}$ describes how light propagates through a material, which can be expressed as:

$$\tilde{n} = 1 - \delta + i\beta \tag{2.16}$$

Here, $\delta = 1 - n$ is called the refractive index decrement. The complex index $\tilde{n}$ is also usually called the refractive index, like its real part n. β represents absorption. In the

EUV range, δ and β are smaller than 1, resulting in weak refraction and modest absorption. However, at specific photon energies near atomic absorption edges, β can increase sharply, enabling element-specific contrast. Interestingly, many materials used in semiconductor applications, such as silicon, silicon nitride, and silicon dioxide, are relatively transparent in large parts of the EUV spectrum, especially between major absorption edges. The EUV photon energy significantly exceeds the energy levels of the solid state bands, causing most radiation interactions to involve tightly bound electrons, which are little affected by the surrounding atoms, except at photon energies close to the absorption edges [121]. However, EUV photons lack sufficient energy to excite core-level electrons in these materials, resulting in low photon absorption cross-sections and hence small β values. This transparency enables EUV light to penetrate thin films and multilayer structures commonly used in semiconductor devices.

As depicted in the Fig. 2.9, the normal incidence transmission of typical semiconductor materials in the EUV region highlights their unique transparency window, a crucial advantage for EUV imaging [34, 35, 43] and spectroscopy [32, 122]. This property allows for non-destructive imaging of buried nanostructures and interfaces with both elemental and chemical sensitivity. Furthermore, the short wavelength of EUV light provides high spatial resolution, making it ideal for applications such as CDI, ptychography, and nanoscale tomography in materials science and semiconductor metrology.

2.3 Table-top EUV ptychographic setup

2.3.1 Vacuum beamline and optical layout

In the setup, that we use to generate high harmonics, near infrared pulses are usually focused by a lens (f=30 cm) into a jet of noble gas filling with argon (backing pressure is around 5 bar). As shown in Fig. 2.10b, a stainless steel tube with 1.4 mm inner diameter is used to guide the gas, and this tube is intersected by our laser through a ~200 μm hole drilled by the focused beam itself. A pulsed piezo valve [123] limits the gas flow of the jet out of the nozzle to periods of roughly 10 us. The pulses are synchronized with the laser system to limit the quantity of noble gas that is used and reduce the gas load on the turbo molecular pumps. The experimental setup maintains intermediate vacuum conditions to prevent significant re-absorption of harmonics outside the interaction region, using three low-vibration turbo molecular pumps (2x Pfeifer HiPace 700 and 1x Pfeifer HiPace 80) in combination with three scroll pumps (2x Edwards XDS10 and 1x Edwards nXDS10i). Typical pressures during operating conditions were measured to be roughly at 10^{-7} mbar in the refocusing and sample chambers in Fig. 2.10d and e, respectively.

Behind the gas jet, a free-standing aluminum membrane (200 nm meshless Al film, Luxel 13494) filters out the fundamental beam, as shown in Fig. 2.10c. In the refocusing chamber, the high harmonics are directly focused by a pair multilayer mirrors (optiXfab) on to the sample. The multilayer mirrors are mounted in two ultra-high vacuum compatible piezo mirror mounts (Newport 8821-UHV). In order to maintain sufficient flux over a preferred range of harmonics (wavelengths 30-40 nm), we choose a plane broad-band

multilayer mirror and a curved (ROC=-500 mm) narrow-band multilayer mirror. Their transmission curves are shown in Fig. 2.10g and h, respectively. The curved mirror is mounted on a one-dimensional piezo stage (Smaract) that enables precise translation along the beam propagation axis, allowing for flexible adjustment of the focus position with respect to the sample, as shown in Fig 2.10d.

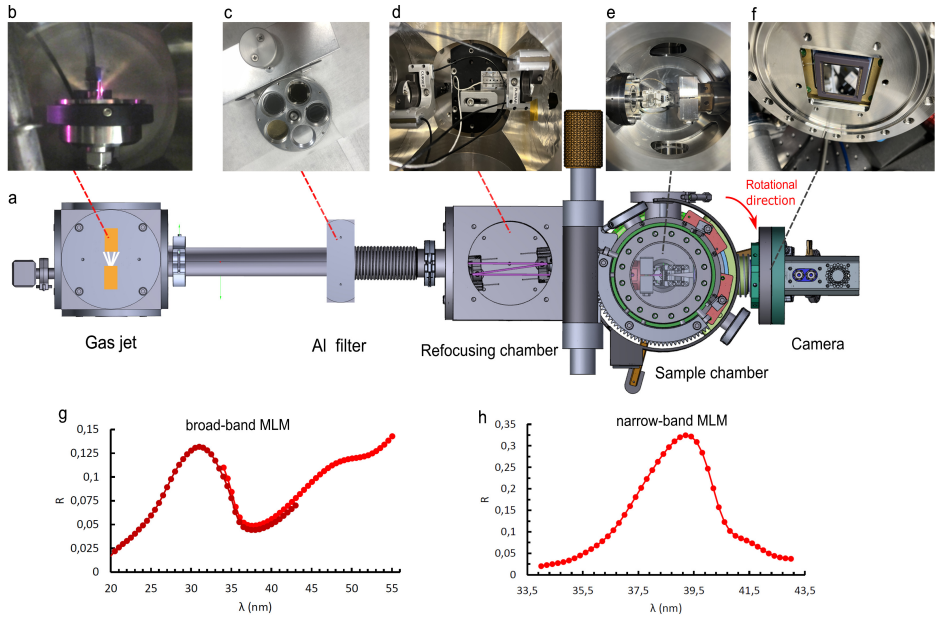

Figure 2.10: (a) Schematic overview of the HHG experimental setup. (b) The gas jet is used to generate HHG. (c) Aluminum filter is used to filter the HHG from near infrared driven laser. (d) A pair of multilayer mirrors is used to focus HHG. (e) Sample chamber. (f) sCMOS camera chip. Reflection curves for (g) broadband and (h) narrow band multilayer mirrors, respectively.

The samples for the imaging experiments are placed in a sample holder, mounted on a piezo-stage with two linear positioners (Smaract SLC-1730) and a angle positioner (Smaract SR-2812), as shown in Fig. 2.10e. Diffraction patterns for EUV experiments where captured using a CMOS (Andor GSENSE400BSI, Marana-X 11, 2048 × 2048 pixels, pixel size 11 μm) or CCD (Andor 936SO, Ikon-L, 2048 × 2048 pixels, pixel size 13.5 μm) camera placed behind the sample, as shown in Fig. 2.10f.

We refer to our custom-designed sample chamber, developed in collaboration with the Mechanical Design and Precision Manufacturing departments at AMOLF, as *Apollo*, named after the first moon landing mission, due to its similar external appearance. The whole design and real-world set up are shown in Fig. 2.11a and b, respectively. To the best of our knowledge, *Apollo* is one of the first imaging chambers worldwide capable of supporting both transmission and reflection mode EUV lensless imaging simultaneously,

using a flange-mounted EUV camera. The purpose of this measurement chamber is to enable precise angular tuning of the mounted camera from 0° to 90° with a resolution of 0.1 degree, while maintaining a vacuum pressure below 10^{-7} mbar. The solution is mounting camera on a series lamella separator to isolate the vacuum from outside. The sample holders are home-designed for reflection and transmission geometry, as shown in Fig. 2.11c and b, respectively.

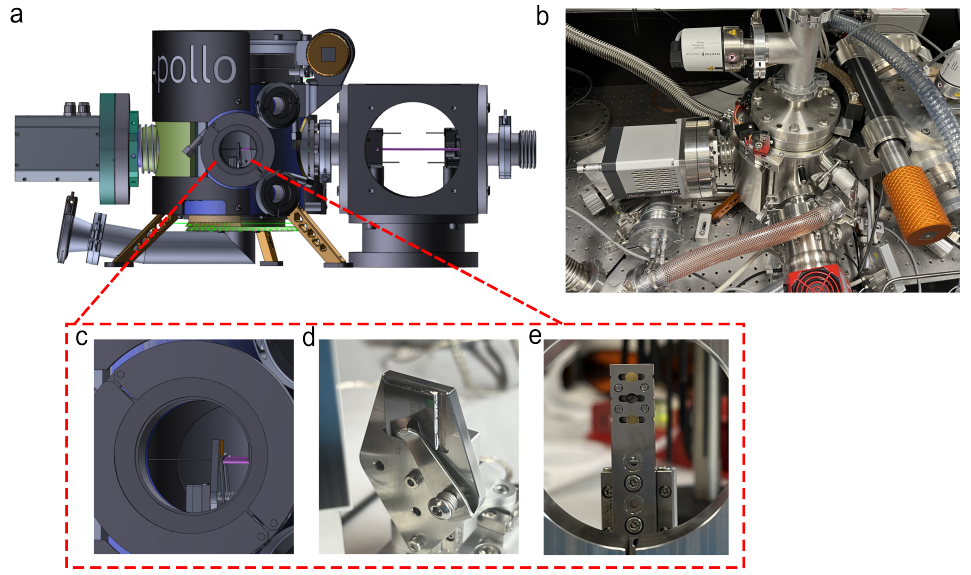

Figure 2.11: (a) Schematic overview of the imaging (*Apollo*) chamber. (b) The real chamber in the lab. Samples and sample holders for (d) reflection and (e) transmission experiments, respectively.

2.3.2 Transmission and reflection imaging geometries

An example of the transmission ptychographic reconstruction using HHG multi-wavelength is shown in figure 2.12. The object is a home-fabricated non-dispersive USAF 1951 resolution target, characterized by a uniform transmission function across all wavelengths, and illuminated by an HHG Gaussian probe. The ptychographic data sets consist of 218 scan positions in a concentric scan grid with 6 μm step size and 104 μm field of view. The multi-PIE algorithm [46, 48] adapted from mPIE [110], enables simultaneous multi-wavelength reconstruction. The reconstructed object, shown in Fig. 2.12a exhibits high quality, with minimal artifacts and sharp edges, though a slight linear phase is observed, likely due to surface irregularities. Figure. 2.12b presents reconstructions for the dominant spectral mode of the six brightest probes, ranging from 41 to 69 nm. The spectral weights, shown in Fig. 2.12d derived from ptychography align closely with grating measurements. Small

differences arise because the ptychographic scan averages the diffracted radiation flux over the scanned area for all wavelength components. The complex-valued reconstructions of the object and probe reveal astigmatism in the beam, attributed to oblique incidence on a curved mirror [51]. The convergence of algorithm, shown in Fig. 2.12c, remains suboptimal after 1470 iters. This will be improved in Chapter 4 by using structured illumination.

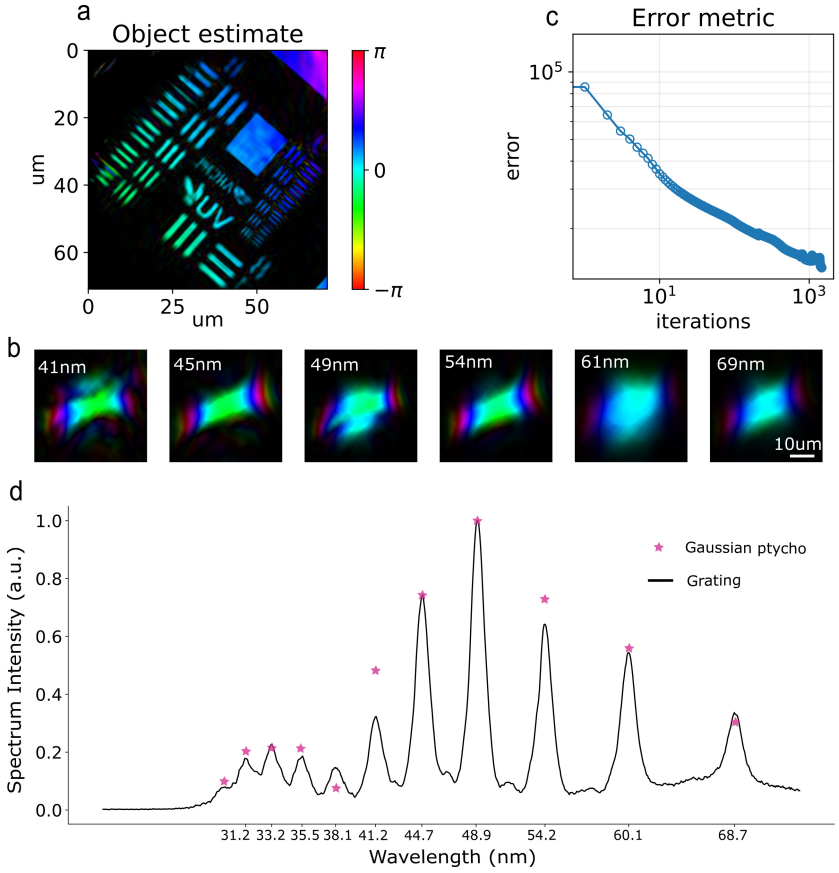

Figure 2.12: Reconstruction results using multiPIE: (a) Reconstructed object, a home-fabricated USAF-1951 resolution target, (b) Reconstructed HHG beams and the spectrum, 11 harmonics. The color represents the phase, and the brightness represents the intensity. (c) Error evolution over 1470 iterations. (d) Measured and reconstructed spectrum of the XUV radiation. Solid line shows the XUV spectrum measured from the diffraction of the HHG beam through a transmission grating with 500 nm pitch.

An efficient way to evaluate the quality of reconstruction is to compare the calculated beam with the direct bare beam measurement on the camera, as shown in Fig. 2.13a,b.

Good agreement can be observed, confirming the accuracy of the quantitative reconstruction results. The dot located in the bottom right of the beam image is attributed to dust on the camera, also shown in the reconstruction results. The further knife-edge experiment, as shown in Fig. 2.13c, d, are applied at the sample plane using a 200 μm thick silicon disk. The knife-edge results also shows a good agreement with the beam size of reconstructed probe.

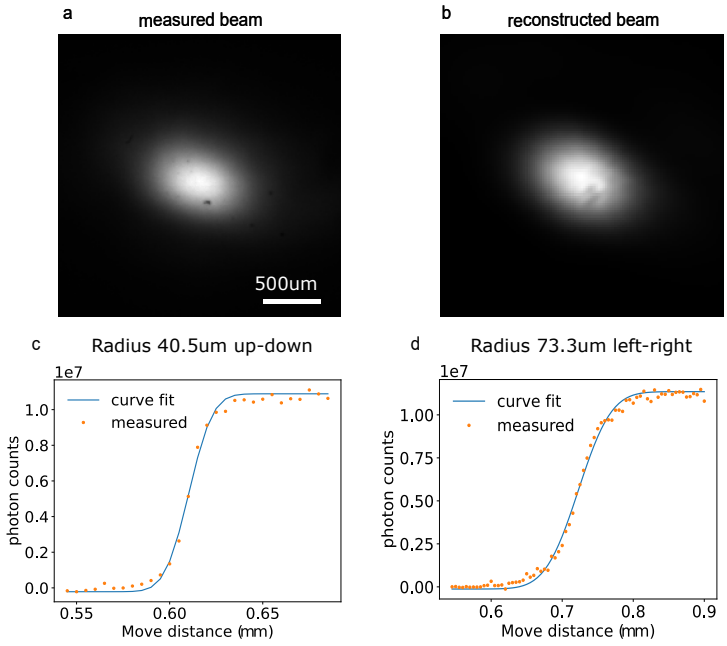

Figure 2.13: Images of the HHG beam at the CCD camera plane (a) directly measured by the camera and (b) calculated from the reconstructions. Knife-edge measurements on the sample plane on (c) vertical and (d) horizontal directions, respectively.

Strictly speaking, HHG ultrashort pulses are partially spatially coherent light [124]. Applying CDI algorithms designed for fully coherent illumination to diffraction patterns generated by partially coherent beams may lead to reconstructions that fail to the correct solution. Instead of complex spectroscopic and filtering devices in the EUV and X-ray regions [125], partially spatially coherent light can be modeled as a mixture of multiple fully coherent spatial modes. By analyzing the diffraction of each spatial mode and employing their incoherent superposition, the constraints can be implemented, leading to high-quality sample reconstruction. In the subsequent reflection reconstruction, mixed-state ptychography is utilized to account for spatial coherence effects, improving reconstruction quality [126].

Figure 2.14 shows an example of the reflection ptychographic reconstruction of a home-fabricated Siemens Star resolution target using the aPIE algorithm. aPIE is a new

engine developed recently [115], which can calibrate the tilt angle for ptychography diffraction patterns in a tilted-plane reflection geometry. The combination of aPIE and multiPIE allows us to do simultaneous multi-wavelength and multi-mode reconstructions in reflection.

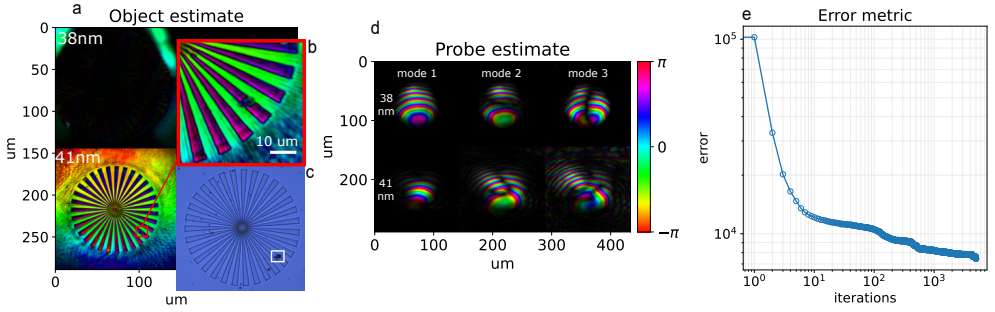

Figure 2.14: Reconstruction results using aPIE+multiPIE: (a) Reconstructed object, a home-fabricated Si siemens star target. (b) A magnified view of the bottom left of the Siemens star. (c) Optical microscopy image of the target. (d) Reconstructed HHG beams, 2 harmonics with 3 orthogonal modes for each harmonics. The color represents the phase, and the brightness represents the intensity. (e) Error evolution over 5000 iterations.

Figure 2.14a shows the reconstructed object, where the intensity of the 38 nm probe is approximately 10% of the total strength of the 41 nm component, contributing to the failure of the object reconstruction in this wavelength. The reconstructed probes shown in Fig. 2.14b are the dominant illumination mode in each data set, making up more than 77% of the power content. The hybrid algorithm, solves for variable mixed-state reflected probes at each position. This method applies singular value decomposition to to extract dominant orthogonal modes from the set of probe functions across all scan positions, projecting them onto a reduced orthogonal basis after each iteration of the ptychographic engine [33]. Application of the hybrid method leads to fewer reconstruction artifacts, providing more quantitative analysis for further reliable material-height map retrieval and classification of materials [35].

Chapter 3

Characterizing Post-compression of MJ-level Ultrafast Pulses via Loose Focusing in a Gas Cell

Fengling Zhang, Antonios Pelekanidis, Augustas Karpavicius, Matthias Gouder, Jacob Seifert, Kjeld Eikema, and Stefan Witte. Optics Express **32**, 40990-41003 (2024).

The ability to generate high-intensity ultrashort laser pulses is a key driver for advancing the strong-field physics and its applications. Post-compression methods aim to increase the peak intensity of amplified laser pulses via spectral broadening through self-phase modulation (SPM), followed by temporal pulse compression. However, other unavoidable nonlinear self-action effects, which typically occur parallel to SPM, can lead to phase distortions and beam quality degradation. Here we study the ability to compress high-energy pulses by loose focusing in a noble gas to induce nonlinear spectral broadening, while limiting unwanted nonlinear effects such as self-focusing. We introduce ptychographic wavefront sensor and FROG measurements to identify the regimes that optimize pulse compression while maintaining high beam quality. Using a 700 mbar argon-filled double-pass-based scheme, we successfully compress 2 mJ, 170 fs, 1030 nm laser pulses to ∼35 fs, achieving 90% overall flux efficiency and excellent stability. This work provides guidelines for optimizing the compressed pulse quality and further energy scaling of double-pass-based post-compression concepts.

3.1 Introduction

High-intensity femtosecond laser pulses are crucial for strong field physics and its applications [81]. Amplifying ultrashort pulses and shortening pulse duration represent a major challenge [82]. Among the ultrashort high-intensity lasers used in strong-field physics, Titanium:sapphire (Ti:Sa) [83] lasers are notable for their broad bandwidth and high peak intensity. In contrast, ytterbium (Yb) ion-doped lasers [84, 85] can achieve very average power and pulse energy but typically have narrower bandwidths, which limited their initial impact on high-intensity applications until the introduction of post-compression techniques. Two methods are commonly employed to achieve such pulse compression at high peak intensity and average power: optical parametric chirped-pulse amplification (OPCPA) and nonlinear-propagation-based post-compression. OPCPA offers a method to amplify ultra-broadband pulses because of its extreme phase-matching bandwidths, even when pumped by narrowband but high-energy laser pulses [81, 88]. On the other hand, post-compression methods [89–92] broaden the spectral width of the high-power pulses [127] through nonlinear interactions during propagation through a medium. Such post-compression methods are particularly appealing due to their high efficiency reaching beyond 95% [128].

Post-compression methods employ nonlinear self-action effects that occur when high-intensity pulses travel through a medium, leading to spectral broadening via self-phase modulation (SPM), as shown in Fig. 3.1a. As the spectral phase accumulated during SPM is well-controlled and typically quadratic, subsequent dispersion compensation can effectively eliminate the pulse chirp, thereby shortening the pulse duration. A related nonlinear effect that generally occurs in parallel to SPM is self-focusing (Fig. 3.1b), leading to spatial wavefront changes and ultimately beam quality degradation[129, 130]. Broadening the spectrum while also minimizing the self-focusing effect poses a significant challenge. Currently, various efficient post-compression methods have been demonstrated for millijoule-level pulses, especially hollow-core fibers[89, 131–133], single[130] or multiple plates[90, 133, 134], and multi-pass cells (MPC)[91, 94, 135, 136]. Hollow-core fibers, filled with noble gases as the nonlinear medium, limit the influence of self-focusing as the beam propagates in a waveguide. Towards higher average power and pulse energy, precise control over the beam pointing and spatial properties are necessary to prevent fiber damage. Multi-plate setups are compact and efficient, but typically operate in a narrow designed optical parameters window with specific pulse conditions. The MPC relies on sequential nonlinear interactions at the focus of an optical cavity, typically a Herriot cell design [135]. Such an approach is scalable to high energies and maintains spatial properties through the cavity mode filtering, but does require careful design and input mode matching for a given nonlinearity.

Recently, various approaches have been explored to compress pulses using hybrid MPC and multiple plates[137, 138], aiming to better control the respective nonlinear effects. A specifically interesting approach is the CASCADE concept [95], which uses loose focusing in an extended gas cell to improve the ratio between self-phase-modulation and self-focusing. This approach can be efficient and robust to alignment variations, and

can operate over a range of input energies.

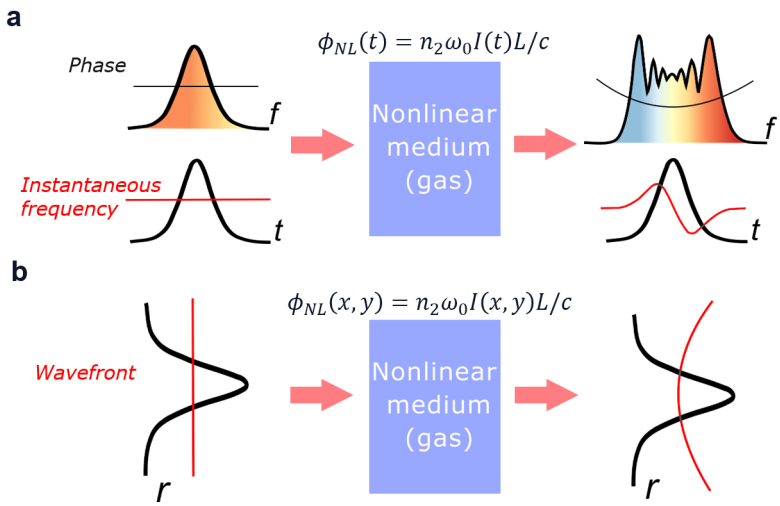

Figure 3.1: Nonlinear processes that occur when a high-intensity laser beam propagates through a medium with an intensity-dependent refractive index. a) Self-phase modulation, leading to a time-dependent phase variation and subsequent spectral broadening. b) Self-focusing, leading to a spatial phase variation that influences beam propagation.

In this work, we report on a robust double-pass setup with limited self-focusing effect for pulse compression of mJ-level, 170 fs Yb ion-doped laser pulses down to 37 fs with 90% overall efficiency, following the CASCADE concept. Each pass involves focusing into an argon gas cell to induce nonlinear spectrum broadening, followed by applying chirped-mirror-based compressor to shorten the pulse duration. We achieve over five-fold pulse compression factors after only two passes, while maintaining good spatial beam properties. In particular, we study the temporal and spatial properties of the compressed pulses in a phase-resolved way, over a wide range of gas pressures to control the amount of nonlinear interaction. The temporal pulse properties are measured using second-harmonic frequency-resolved optical gating (SHG-FROG). For spatial characterization, we use ptychographic wavefront sensing [18, 49, 139] at different wavelengths across the pulse spectrum. Using numerical pulse propagation methods, we retrieve the spatiospectral properties of the beam around a focus. This approach allows the identification of optimal working conditions for the pulse compression system. By retrieving high-resolution quantitative data at specific working conditions, we can design scaling pathways towards higher pulse energy and shorter pulse duration more reliably.

3.2 Processes resulting from the intensity-dependent refractive index

Self-phase modulation occurs when a high-intensity light beam modifies the optical properties of a material, giving rise to an intensity-dependent nonlinear refractive index. The refractive index $n(x, y, z_0; t)$ in the presence of this type of nonlinearity at z_0 along the propagation z-direction can be written as

$$n(x, y, z_0; t) = n_0 + n_2 I(x, y, z_0; t) \tag{3.1}$$

where n_0 is the linear refractive index, n_2 is the nonlinear refractive index (positive value in our case) of the medium, and the intensity of the light $I(x, y, z_0; t) = 2n_0\epsilon_0 c|\widetilde{A}(x, y, z_0; t)|^2$ contributes to both spatial (x, y) and temporal t changes in the refractive index ($\widetilde{A}$ is the spatially slowly field amplitude). The effect of this nonlinear interaction is to add a propagation-dependent phase, given by:

$$\phi_{NL}(x, y; t) = -\frac{n_2\omega_0}{c}\int_0^L I(x, y, z; t)dz = -n_2 I(x, y; t)\omega_0 L/c \tag{3.2}$$

where ω_0 is the center angular frequency of the optical pulse, c is the speed of light, and L is the propagation distance. The phase $\phi_{NL}(x, y; t)$ is also commonly referred to as the B-integral [91, 94, 95, 135, 140]. The spectral content of the propagated pulse $S(\omega)$ can be described by its energy spectrum:

$$S(\omega) = |\int_{-\infty}^{\infty} \widetilde{A}(t)e^{-i\omega_0 t - i\phi_{NL}(t)}e^{i\omega t}dt|^2. \tag{3.3}$$

The temporal pulse shape $I(t)$ leads to a time-dependent phase $\phi_{NL}(t)$, which results in the generation of new frequencies to the spectrum $S(\omega)$. This is the process of self-phase modulation, which can be intuitively described by introducing the instantaneous frequency $\omega(t) = \omega_0 + \delta\omega(t)$, where the variation $\delta\omega(t)$ is given by:

$$\delta\omega(t) = \frac{d}{dt}(\phi_{NL}(t)) = -\frac{n_2\omega_0 L}{c}\frac{dI(t)}{dt} \tag{3.4}$$

An example of SPM is illustrated in Fig. 3.1a, in which the pulse shape is given by a Gaussian distribution. Under the assumption that n_2 is positive, Eq. 3.4 indicates that the instantaneous frequency shifts to lower frequencies in the leading edge of the pulse and to higher frequencies in the trailing edge. The variation in the instantaneous frequency is illustrated by the solid red curve in Fig. 3.1a. Equation 3.4 shows that the instantaneous frequency is proportional to the intensity gradient of the driving pulse $dI(t)/dt$. Consequently, shorter input pulses with a steeper slope $dI(t)/dt$ will result in more significant spectral broadening.

Similar to the time domain picture, the spatial intensity profile of the laser pulse leads

to a spatial variation of $\phi_{NL}(x, y)$. For Gaussian beam profiles this variation resembles a quadratic phase profile (Fig. 3.1b), which causes the material to act as a positive lens. Analogous to the instantaneous frequency in Eq. 3.4 for the time-domain case, we can express the spatial frequency variation $\delta\mathbf{k}(x, y)$ due to self-focusing as:

$$\delta\mathbf{k}(x, y) = \nabla\phi_{NL}(x, y) = -\frac{n_2\omega_0 L}{c}\nabla I(x, y). \tag{3.5}$$

This expression shows that the induced wavefront curvature is proportional to the spatial intensity gradients. Large spatial gradients will thus cause significant self-focusing, which can lead to wavefront aberrations and result in optical damage to the optical components in the beamline[141, 142].

Because SPM and self-focusing result from the same nonlinearity, they will always occur together. However, their dependence on temporal versus spatial intensity gradients provides a way to control the relative strength of the effects, which is the basis of the CASCADE concept. A loose focusing geometry minimizes spatial gradients and therefore limits self-focusing, while pulse compression between multiple SPM stages increases the temporal gradients to maximize spectral broadening.

3.3 Pulse compression in a loose focusing geometry

3.3.1 Experimental setup

The experimental setup is shown in Fig. 5.1. We use an Yb-based laser system (Pharos from Light Conversion) delivering 2 mJ, 170 fs pulses at a center wavelength of 1030 nm and a repetition rate of 1 kHz. The full-width-at-half-maximum (FWHM) beam diameter is 3.9 mm. The laser pulses are loosely focused in gas to induce nonlinear broadening with limited self-focusing, combined with chirped-mirror-based compression between passes. The pulses are first focused into a pressure-tunable argon gas cell by a concave mirror (5 m radius of curvature), and an another concave mirror is used to collimate the beam afterwards. The subsequent dispersion compensation is implemented using a pair of chirped mirrors (CMs) (GDD=-500 fs^2, UltraFast Innovations, CM39). To avoid additional nonlinear effects in the entrance and exit windows of the gas cell, we use 1 mm thin anti-reflection coated fused silica windows and place them close to the curved mirrors. The same loose focusing geometry is applied in the 2nd pass through a separate gas cell. The energy throughput of the system exceeds 90% and is mainly determined by the reflectivity of the mirrors.

3.3.2 Temporal pulse characterization

To characterize the temporal pulse profile and phase, SHG-FROG measurements (Mesa Photonics, LLC) are applied after each pass, with the results displayed in Fig. 3.3. The dark blue dashed traces in the left column of Fig. 3.3 show the broadened spectra after each

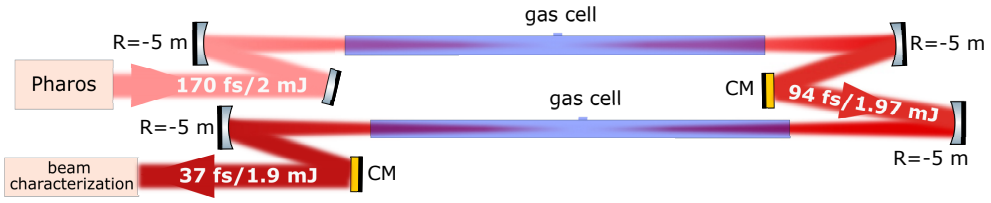

Figure 3.2: Schematic of the setup: the laser output is loosely focused by the concave mirror R=-5 m into the argon gas cell, and subsequently collimated and compressed using chirped mirrors (CM). The 2nd pass uses a similar loose focusing geometry and CM compression.

pass as measured directly by the spectrometer. The reconstructed spectra from the SHG-FROG (solid blue traces) are in good agreement with these measurements. The broadened spectra are also consistent with calculations of the expected SPM (light blue traces). By comparing spectra, the B-integral (Eq. 3.2) of the first and the second pass through 700 mbar argon is estimated at 1.3π and 1.7π, respectively. The nonlinear refractive index of argon at 700 mbar is taken to be $n_2(700\ mbar) = 0.9 \times 10^{-19} cm^2/W$[143, 144]). Without applying dispersion compensation between the passes, the total accumulated B-integral would have been 2.3π, i.e. 1.3 times less. The measured and calculated spectra are shown in Fig.5.1. The dark blue curves are the retrieved spectra from FROG measurements, and the dark blue dashed curves are measured spectra by spectrometer, and the light blue dashed curves are calculated spectra using Eq. 3.3. The red curves are the retrieved spectral phases. The third column shows the measured (top) and retrieved (bottom) FROG trace of each measurements, respectively. Experiments at a higher gas pressure of 800 mbar in both cells (Fig. 3.3, bottom two rows) show a further increase in spectral broadening, but also more structured spectra.

The second column in Fig. 3.3 shows the pulse durations retrieved from the FROG reconstructions. After the first pass, pulse compression close to the Fourier transform limit (TL) is readily achieved, and the temporal profiles are clean with only very minor pre- and post-pulses. After the second pass, near-transform-limited compression to 37 fs is still achieved, although some satellite pulses remain in the temporal profile, likely due to imperfect compensation of higher-order phase terms. Pulse compression to below the measured 37 fs can be achieved by further increasing the pressure inside the gas cells, along with fine-tuning the pass number in the chirped mirror compressor. At a pressure around 800 mbar in both cells, a slightly shorter pulse duration of 34 fs is retrieved (Fig. 3.3c).

The measured spectra for different gas pressures after the second cell are shown in Fig. 3.4a. The bandwidth of the spectrum at -20 dB of the maximum value is plotted as grey points in Fig. 3.4b. For pure SPM and assuming a linear dependence of n_2 on pressure, Eq. 3.4 predicts a linear trend [129, 136, 145], which is the case up to a pressure around 600 mbar. Beyond this pressure, the trend becomes nonlinear, indicating the growing influence of other mechanisms such as intensity changes induced by self-focusing during

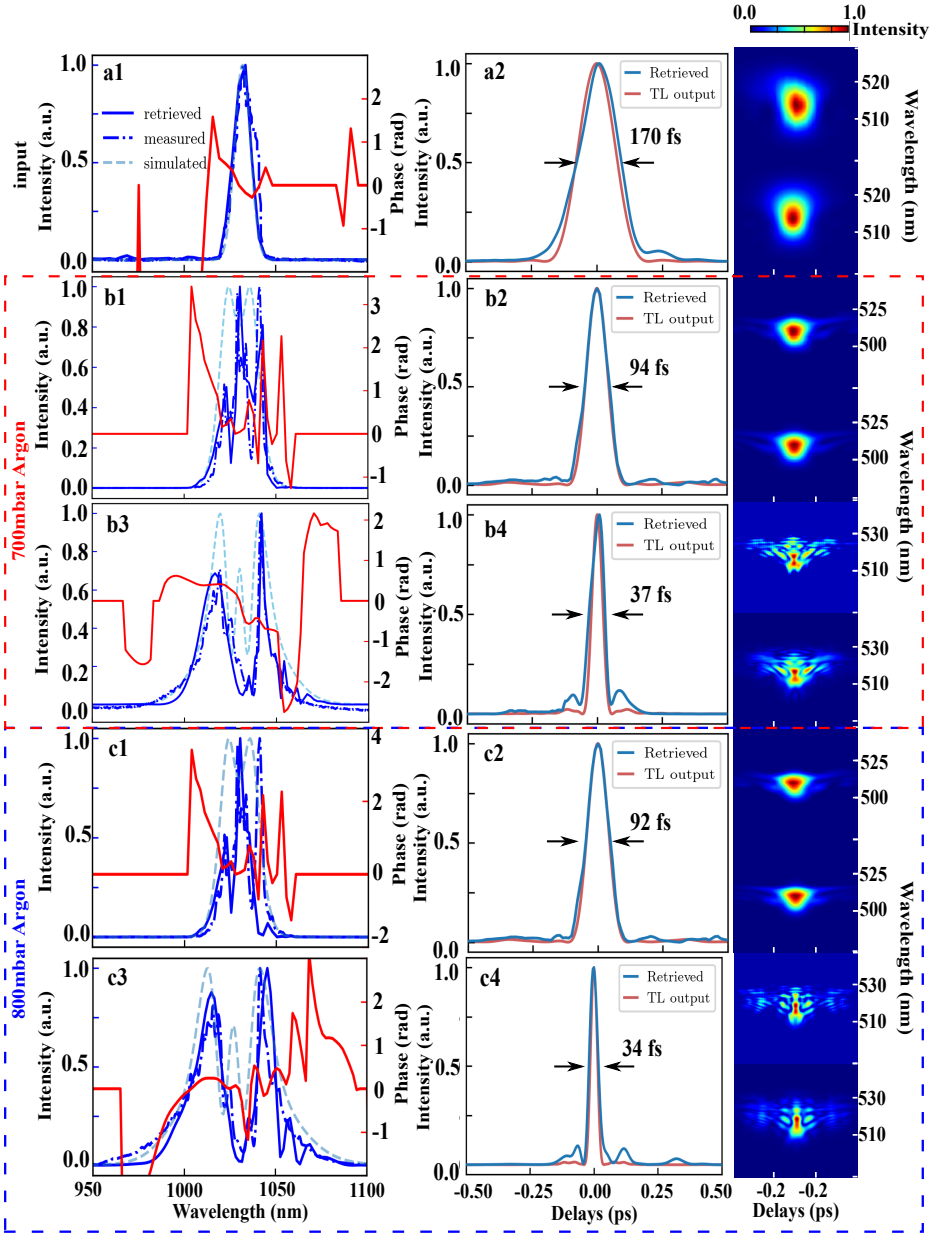

Figure 3.3: SHG-FROG measurements and retrieved spectral fields and temporal pulse shapes for the input pulse (a1,a2), after the first gas cell and chirped mirrors (b1,b2,c1,c2), and after the second gas cell and additional chirped mirrors (b3,b4,c3,c4). For both gas cells, measurements were performed at Argon pressures of 700 mbar (b1-b4) and 800 mbar (c1-c4), respectively.

propagation.

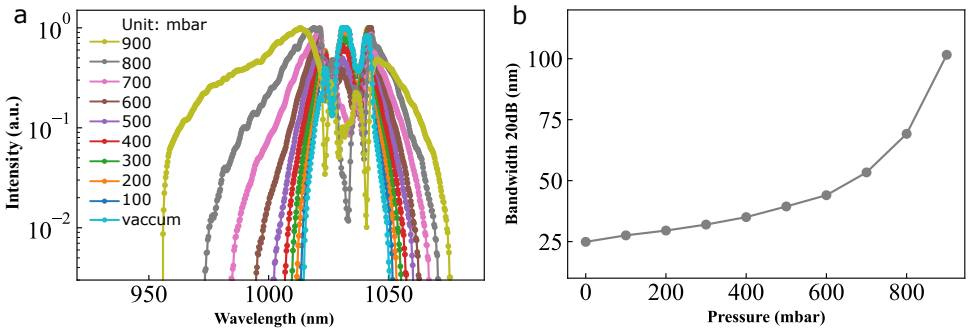

Figure 3.4: a) Measured output spectra for different argon pressure in the second gas cell. b) Spectral width at 20 dB below maximum

3.3.3 Spatial beam characterization

To characterize the spatial properties of the beam after the spectral broadening, ptychographic wavefront sensor (PWFS) measurements [49, 139] are performed directly behind both gas cells. Such PWFS measurements retrieve high-resolution images of the full complex field (both amplitude and phase profiles). The fields are measured before the collimating mirror to accurately determine the curvature of the wavefront exiting the gas cell.

To identify any wavelength dependence in the beam profiles, these PWFS measurements are performed for a series of wavelengths, which are selected using ultra-narrow bandpass filters (Laser Components HBP1063.1/1.8-25, HBP1030.2/1.2-25). The reconstructed fields after the two pulse compression cells for different wavelength components and two gas pressures are shown in Figs. 3.5.

The output after the first cell (Figs. 3.5a1-a3) shows no significant wavelength dependence of the wavefronts when using 700 mbar argon. Increasing gas pressure leads to a slight reduction in wavefront curvature (Figs. 3.5b1-b3) at the output due to self-focusing, while maintaining a Gaussian spatial profile across the spectrum. Using 700 mbar argon in the CASCADE, pulse compression after the first cell results in 94 fs pulse duration, which leads to increased nonlinear effects in the second cell as propagation conditions are kept nominally identical to the first pass. The PWFS measurements after the second cell (Figs. 3.5c1-c5,d1-d5) confirm this, with the wavefronts showing more pronounced variations in curvature, and a stronger dependence on gas pressure. As a consequence of the increased SPM, we could measure at two more wavelength components near the edges of the output spectrum. Note that these wavelength components were generated via SPM and were not in the input spectrum.

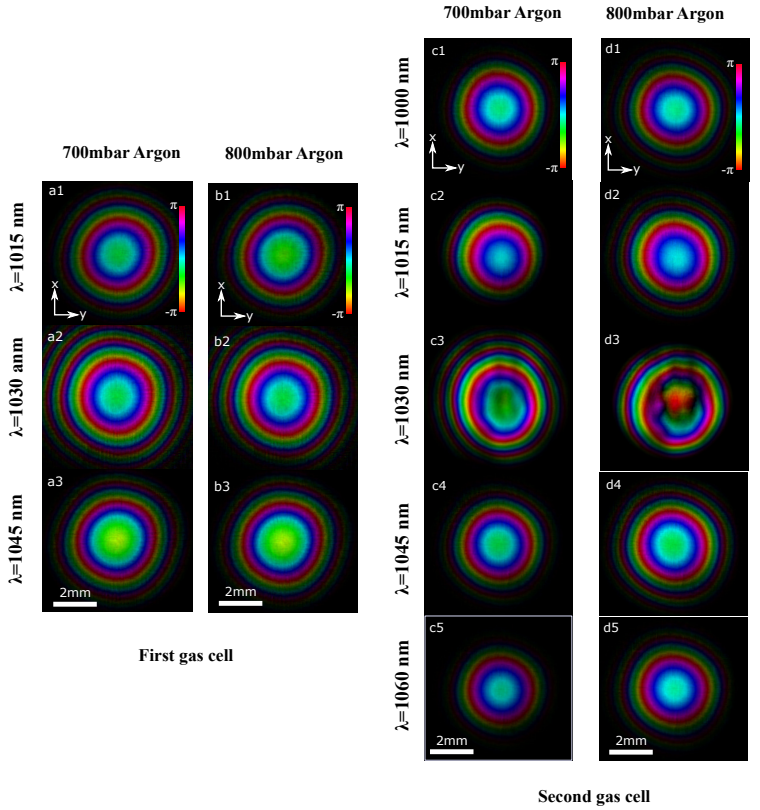

Figure 3.5: Reconstructed probe beams after a-b). first gas cell and c-d). second gas cell under 700 mbar and 800 mbar argon, respectively. Color encodes phase (see scale bar), and brightness represents field amplitude.

Increasing the gas pressure to 800 mbar (Figs.3.5d) leads to particularly significant beam distortions at 1030 nm, including intensity modulations across the beam, and the nonlinear effects at 1015 nm and 1045 nm start to deteriorate the output wavefront as well. At this pressure, the input power is just below the critical power, $P_{in} = 0.87P_{cr}$, which will lead to multiphoton ionization and plasma generation [146]. The distortion of beam wavefronts under such significant nonlinear effects are to be expected.

3.3.3.a Self-focusing analysis via backward propagation

To study the beam as it emerges from the gas cells, we study the focusing properties of the compressed beam by back-propagating measured wavefronts. A complete analysis would require solving the nonlinear time-dependent Schrodinger equation in 3D, which

is a computationally challenging task. We employ a more limited approach, which still provides insight into the main operating conditions of the CASCADE system.

To include the effect of self-focusing in the beam reconstruction inside the gas cell, we numerically propagate the PWFS reconstructions backwards through the nonlinear medium using a split-step approach [147]. Starting with a transverse field distribution $E(x, y)$, propagation in the z-direction over a distance dz can be described as:

$$E(x, y, z + dz) = \mathcal{F}^{-1}\{\mathcal{F}\{E(x, y, z)\}H(k_x, k_y, dz)\exp(i\phi_{NL}(x, y))\} \tag{3.6}$$

where $\mathcal{F}$ and $\mathcal{F}^{-1}$ denote forward and inverse 2D Fourier transforms. The transfer function is given in Eq. 3.8. The nonlinearity is included by multiplying the propagated field with a phase term including $\phi_{NL}(x, y)$ in the Fourier domain in Eq. 3.6. The nonlinear phase can be calculated for a given intensity profile using Eq. 3.2, which however varies during propagation. To approximate the nonlinear propagation, Eq. 3.6 is evaluated for a series of steps, where the step size dz is sufficiently small to approximate the intensity profile close to constant over this length [148]. The phase $\phi_{NL}(x, y)$ is calculated at each step and included in the field propagation via Eq. 3.6. In our calculations dz is chosen as $dz = -5\ cm$, corresponding to half of the Rayleigh length.

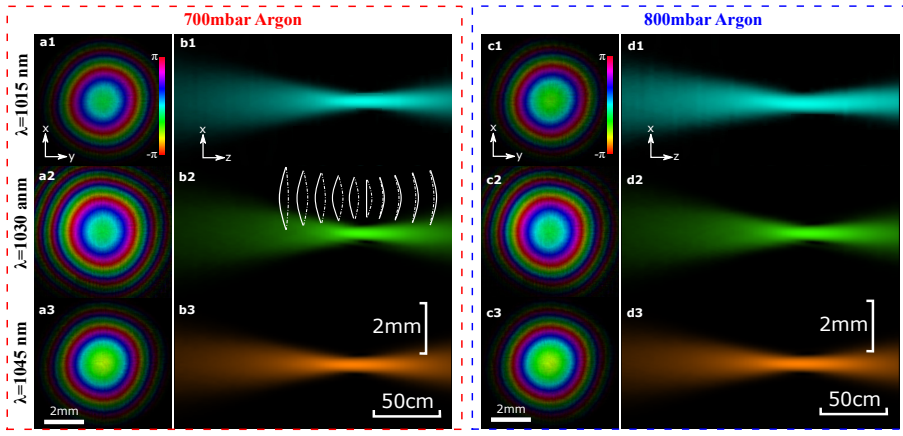

Figure 3.6: Spatial beam characterization after the first gas cell. a1-a3) Ptychographic wavefront reconstructions at 700 mbar argon pressure, at wavelengths of 1015 nm, 1030 nm and 1045 nm, respectively. Color encodes phase (see scale bar), and brightness represents field amplitude. b1-b3) Numerically reconstructed xz-plane side-views of the beams from a) propagation from right to left. The inset in b2) schematically shows the wavefront curvature for linear propagation (solid lines) and the contribution of self-focusing (dash-dotted lines, not to scale). c1-c3) Ptychographic wavefront reconstructions at 800 mbar argon pressure. d1-d3) Numerically reconstructed xz-plane side-views of the beams from c.

Using this approach we can construct side-view images of the beam propagation through the gas cell (Figs. 3.6b,d). Because of the limitations of the approach, these

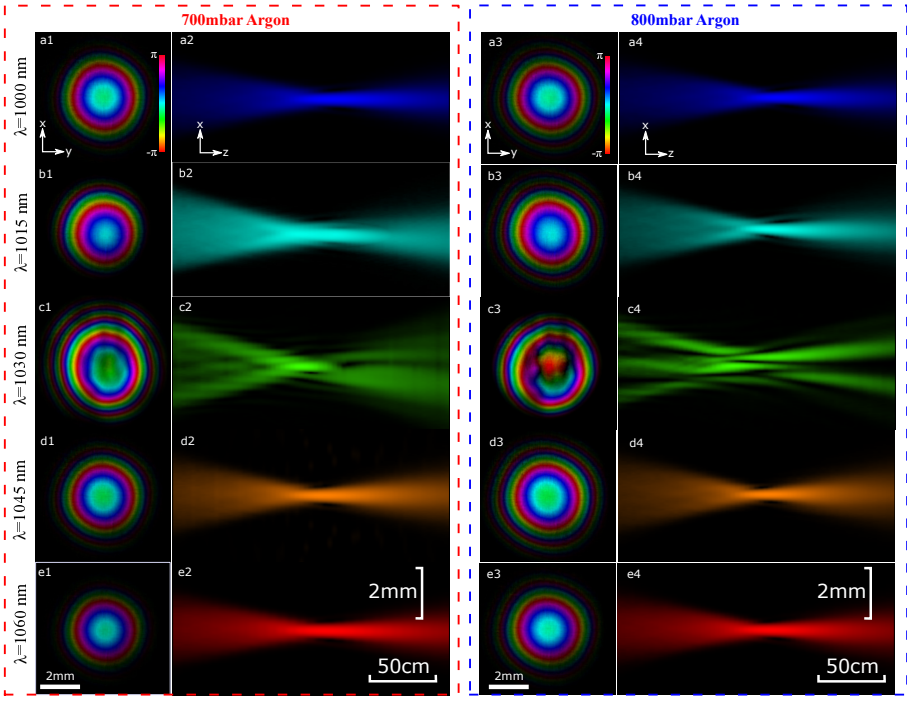

Figure 3.7: Spatial beam characterization after the second gas cell. a1-a5) Ptychographic wavefront reconstructions at 700 mbar argon pressure at five different wavelength components. Color encodes phase (see scale bar), and brightness represents field amplitude. b1-b5) Numerically reconstructed xz-plane side-views of the beams from a) propagation from right to left. c1-c5) Ptychographic wavefront reconstructions at 800 mbar argon pressure. d1-d5) Numerically reconstructed xz-plane side-views of the beams from c.

images do not contain information about the nonlinear frequency conversion, but are only intended to assess the importance of self-focusing in the beam propagation. Of course, the wavelength components at 1015 and 1045 nm in Fig. 3.6 are generated around the focus, and therefore propagating them to before the focal point is not realistic. However, the relative focus positions as they are influenced by the self-focusing effect can be determined through this approach, which is a major design parameter for the CASCADE system.

For the first pass, we find only limited influence of self-focusing, with the beam propagation only slightly deviating from linear Gaussian beam propagation. To illustrate the effect of self-focusing, Fig. 3.6b2 has an inset showing the wavefront for linear propagation (solid lines) as well as the induced wavefront change due to self-focusing (dash-dotted lines). As the beam converges towards the focus, the increased intensity leads to a stronger influence of self-focusing. For this first pass example, the maximum induced phase lag near the focal plane is estimated at 0.06 rad via Eq. 3.2. Overall the output from the first gas

cell shows no significant wavelength dependence of the wavefronts. Increasing gas pressure leads to a slight reduction in wavefront curvature at the output due to self-focusing, while maintaining a Gaussian spatial profile across the spectrum.

Using 700 mbar argon in the CASCADE, our pulse compression after the first cell results in 94 fs pulse duration, which results in increased nonlinear effects in the second cell as propagation conditions are kept nominally identical to the first pass. As a consequence of the increased SPM, we could measure at two more wavelength components near the edges of the output spectrum. Note that these wavelength components were generated via SPM and were not in the input spectrum. Therefore, propagating them backwards through the cell as shown in Figs. 3.7b,d is mainly done to characterize their propagation after the focus in comparison to the other wavelength components. A striking observation is that at the center wavelength of 1030 nm, propagation clearly deviates from linear Gaussian behavior with minor modifications, but shows additional diffraction effects. As our model only includes linear propagation and self-focusing via Eq. 3.2, the exact beam properties near the focus cannot be reliably reconstructed in this way. Given that the input beam has a clean Gaussian intensity and wavefront (see Fig. 3.6) that does not match the propagation result in Fig. 3.7b3, we can conclude that additional nonlinear effects influence the propagation in the second cell. While more detailed propagation simulations can include such effects [95, 142, 146], this working regime is not suitable for a stable pulse compression system, and the present PWFS data and these basic simulations can be used to identify the limits. Interestingly, the wavelengths towards the edge of the spectrum, which are produced inside the cell, do display smooth beam profiles and wavefronts that allow high-quality focusing.

3.3.3.b Beam characterization via forward propagation

Knowing both the amplitude and phase profiles at the plane of the PWFS allows us to numerically propagate the beams to any plane, enabling us to assess beam quality. Starting with the measured wavefronts, we first remove the quadratic phase to get the transverse field distribution $E(x, y)$ corresponding to a focal length of 2.5 m before the second CASCADE gas cell. Subsequently, a phase curvature corresponding to a lens with a focal length $f = 30\,cm$ is numerically added to evaluate beam propagation quality under typical experimental conditions. This beam propagation [149] in the z-direction over a distance dz can be described as:

$$E(x, y, z + dz) = \mathcal{F}^{-1}\{\mathcal{F}\{E(x, y, z) exp(ik(x^2 + y^2)/2f)\} H(k_x, k_y, dz)\} \tag{3.7}$$

where $\mathcal{F}$ and $\mathcal{F}^{-1}$ denote forward and inverse 2D Fourier transforms. The propagation transfer function $H(k_x, k_y, dz)$ is given by:

$$H(k_x, k_y, dz) = \exp(i\sqrt{k^2 - k_x^2 - k_y^2}dz) \tag{3.8}$$

where k is the magnitude of the wavevector of the propagated field, and k_x and k_y are the transverse components of the wavevector. The transfer function in Eq. 3.8 describes linear propagation. In our calculations, we set dz to 1 mm, smaller than the Rayleigh length (30 mm at 1060 nm), to obtain a detailed view of propagation through the focal region.

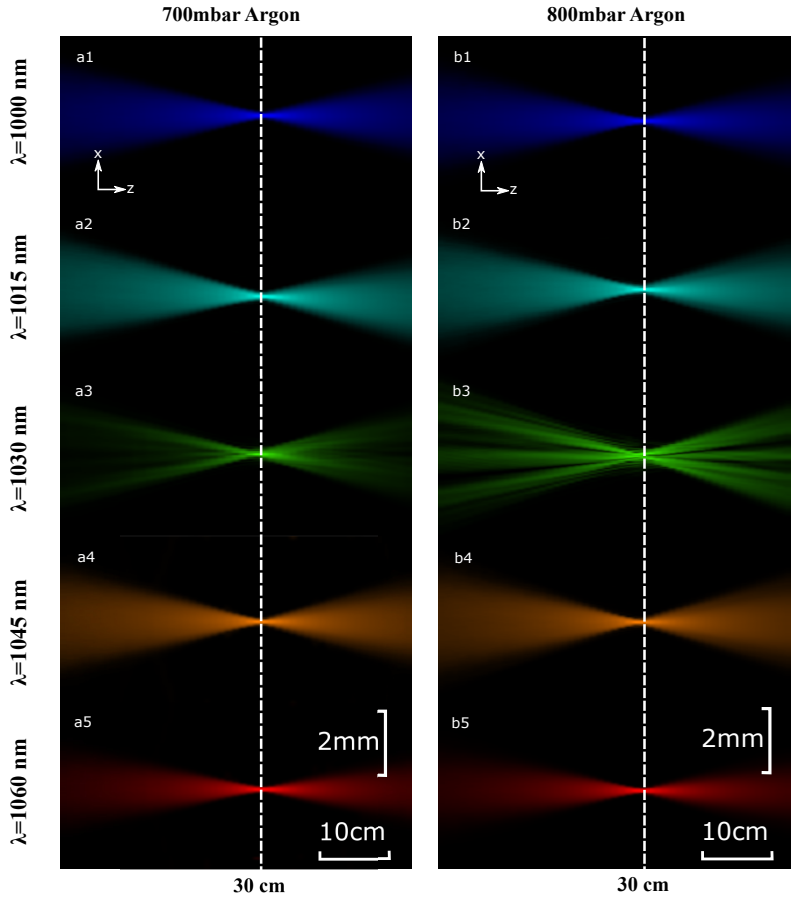

Figure 3.8: Numerical forward propagation of the experimentally retrieved complex fields at multiple wavelengths. a1-a5) Numerically reconstructed xz-plane side-views of the beams from Figs. 3.5c (propagation from left to right). b1-b5) Numerically reconstructed xz-plane side-views of the beams from Figs. 3.5b. The white dashed lines indicate the physical location of the focus position.

Using this approach we can construct side-view images of the beam propagation through the focus (Figs. 3.8a,b), where the white dashed lines indicate the position of lens focus. The divergence and focal positions for each wavelength can be clearly identified,

and a tight focus is observed in the cross section, without major influence of astigmatism or other wavefront aberrations. The limited variation in focal position across wavelengths indicates the absence of chromatic aberration in the pulse compression process.

Propagating the most intense wavelengths beams to a common focal plane enables us to investigate the spatiospectral properties and focus quality of the beam. Figures 3.9a4-a6 and b4-b6 show the intensity distributions for different wavelength components. The strong nonlinear effects during spectral broadening, especially for 800 mbar argon pressure, lead to the formation of a non-Gaussian focused beam at the input wavelength of 1030 nm, as shown in Fig. 3.9b5. At 700 mbar pressure, the incoherent addition of all wavelength components gives a well-formed polychromatic focus, with the FWHM beam diameter of approximately 306.8 um (Fig. 3.9a1). However, small wavelength-dependent differences in spot shape are already visible. At 800 mbar pressure, sidelobes and wavelength-dependent focusing differences significantly affect the quality of the polychromatic focus (Figure 3.9b3).

To connect our PWFS results to other common methods for beam quality analysis, we retrieve M^2 values from the measured complex wavefronts [139] over a range of gas pressures. Starting from the reconstructed complex-valued probes at 1030 nm, we linearly propagate these fields through a focus and subsequently calculate M_x^2 and M_y^2. The retrieved values as a function of argon pressure are shown in Fig. 3.9c. Starting from an input laser beam with $M^2 = 1.11 \times 1.11$, the beam quality factor maintains acceptable values of $M^2 = 2$ after the two-stage post-compression for argon pressure up to 700 mbar. We attribute the difference in beam quality of the two axes to the slight astigmatism in the beam caused by the focusing mirrors, leading to a small different nonlinearity. The inset figure in Fig. 3.9c also shows the beam quality of spectral components towards the edges of the bandwidth. Interestingly, these components consistently maintain a high beam quality throughout the spectral broadening process, even at gas pressures up to 900 mbar. In contrast, the beam quality at the center wavelength severely degrades above 700 mbar, showing significant intensity modulations and phase distortions (Fig. 3.5d3), caused by excessive nonlinear effects[130] at these higher gas pressures, which would eventually lead to optical breakdown [146].

The high beam quality at the outer spectral ranges can be explained by the SPM mechanism, as these wavelengths are mainly generated inside the (second) gas cell. As these wavelength components only appear around the focus, they experience much less nonlinear propagation effects and associated self-focusing and other beam distortion effects.

In the presented double-pass configuration, using our specific beam parameters and focusing geometry, we therefore conclude that maintaining sufficient beam quality across the spectrum requires an argon pressure below 700 mbar, and therefore the achievable compressed pulse duration is limited to 37 fs. Even though shorter pulse durations are obtained at higher pressure, the (wavelength-dependent) reduction in beam quality will likely reduce the applicability of such pulses in strong-field experiments.

We confirm this expectation by using the compressed pulses for high-harmonic generation (HHG) in a gas jet geometry. To achieve a Fourier-limited pulse at different CASCADE

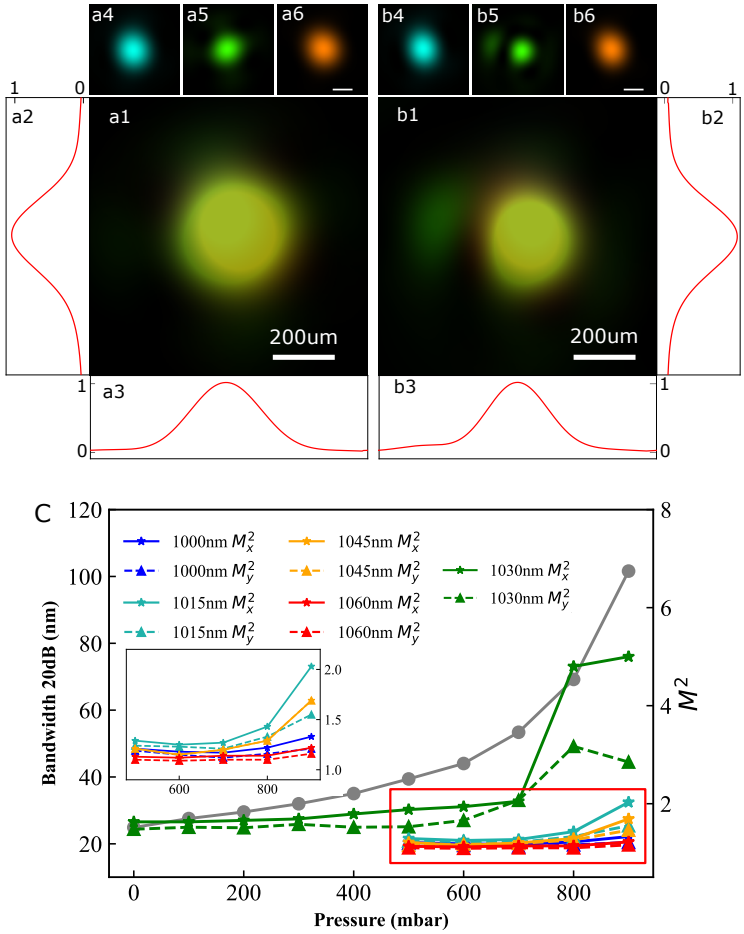

Figure 3.9: Intensity profile of the polychromatic focus summed over three central wavelength beams after a1) 700 mbar and b1) 800 mbar argon filled CASCADE, respectively. 1D intensity of the polychromatic focus for a2-a3) 700 mbar and b2-b3) 800 mbar argon filled CASCADE, respectively. The sub-figures a4)-a6) and b4)-b6) show the color coded monochromatic (blue: 1015 nm, green: 1030 nm, orange: 1045 nm) intensity plots of corresponding focus, and the scaled bar represents 200 um. c) Beam quality parameter M^2 as determined for different wavelength components separately. The inset figure shows the enlarged view of the red area, to better visualize the M^2 values for the wavelengths towards the edge of the spectrum. The bandwidth of the broadened spectrum at -20 dB of the maximum value is plotted as grey points, which refer to the left y-axis.

pressures, we adjusted the number of bounces on the CMs and confirmed the pulse duration through FROG measurements. In addition to optimizing the pulse compression, we

adjusted other HHG generation parameters independently, such as gas backing pressure and lens position, to maximize HHG brightness. When focusing the pulses into a 0.6 mm wide argon jet (around 4 bar backing pressure), using a 30 cm focal length lens, we observe optimal HHG for an argon pressure of 620 mbar in the compression cells. Increasing the pressure to 750 mbar results in a 7% reduction in HHG yield, which we attribute to the reduced overall laser beam quality.

An extension towards shorter pulse durations will therefore require an increase in SPM without increasing the spatial nonlinearities such as self-focusing. This can be achieved by an even looser focusing geometry, to reduce the spatial gradients (Eq. 3.5) while maintaining temporal gradients (Eq. 3.4). Alternatively, adding more passes through the nonlinear medium at constant or even slightly lower gas pressure will have a similar effect. Including pulse compression after each stage will then significantly improve the SPM-to-self-focusing ratio, as it increases the temporal gradients before subsequent broadening. This approach was recently shown to work very effectively [95]. Such intermediate compression is more challenging to incorporate in multipass cell configurations, but can be achieved e.g. by using chirped cavity mirrors [150, 151].

3.4 Conclusions

Using a double-pass CASCADE scheme, we demonstrate post-compression of 2 mJ 170 fs Yb ion-doped laser pulses to 37 fs with 90% overall flux efficiency, while maintaining good beam quality across the full spectrum. Specifically, we use SHG-FROG and PWFS measurements to characterize the compressed pulses in both the temporal and spatial domain. This approach provides a detailed view on the results of the nonlinear effects in each broadening stage, and it enables a determination of optimum working conditions for the pulse compression system in terms of pulse duration, beam quality and system complexity. Specifically, we note the importance of wavelength-resolved wavefront characterization, as highlighted by our observations in Fig. 3.5. While an averaged wavefront and beam profile may show acceptable behavior, we find that the nonlinear propagation can lead to strong aberrations at specific wavelength components, especially those already present in the input spectrum. This effect may lead to significant spatiotemporal coupling upon focusing, affecting the efficiency and reproducibility in strong-field experiments.

While a similar approach can be taken to characterize multipass cell or fiber-based compression systems, we focused on a particularly simple implementation of the CASCADE-type scheme using only double-pass compression. Our measurements confirm that these systems indeed enable effective broadening via SPM while limiting self-focusing, and have favourable scaling properties towards higher pulse energy.

Chapter 4

Illumination Diversity in Multi-Wavelength Extreme Ultraviolet Ptychography

Antonios Pelekanidis*, Fengling Zhang*, Matthias Gouder, Jacob Seifert, Mengqi Du, Kjeld S. E. Eikema, and Stefan Witte. Photonics Research **12**, 2757-2771 (2024). (**These authors contributed equally.*)

Lensless EUV imaging at nanoscale resolution has become possible with the development of table-top HHG systems. Ptychography with monochromatic EUV illumination exhibits extraordinary robustness and accuracy to reconstruct both the object and the illumination beam profile. Incorporating structured illumination further improves reconstruction robustness and image resolution by enhancing high-spatial-frequency diffraction. However, broadband imaging remains challenge due to the complexity of multi-wavelength algorithms, particularly in separating distinct spectral information. Here we show that introducing spatial diversity between spectral components of the beam can significantly improve the reconstruction quality in multi-wavelength EUV ptychography. The diversity in the polychromatic illumination is quantified by applying geometry- and information-based dissimilarity metrics to the diffraction patterns. We experimentally verify the effect of diversity by comparing ptychography measurements using Gaussian, binary-structured, and wavelength-dependent orbital angular momentum beams. Our results show that structured illumination enables the separation of spectral components within a single diffraction pattern while also maximizing added information from each new scan positions. Our work can be anticipated as a starting point for high-fidelity polychromatic imaging of next-generation nanostructured devices at EUV and soft-X-ray wavelengths.

4.1 Introduction

Advances in diffraction-based imaging technology [152, 153] have pushed the achievable resolution well beyond the capabilities of conventional microscopes. In particular, coherent diffraction lensless imaging (CDI) in the EUV regime has become an active research area. The short wavelengths in the EUV region give a better diffraction-limited resolution [154] compared to visible or infrared light, while it is still possible to generate coherent light at these wavelengths with tabletop sources via HHG from a near-infrared (NIR) driving laser [32, 155–159]. One specific technique for CDI is ptychography, in which the object is translated laterally to the source and a series of correlated diffraction patterns are captured [99, 160]. The reconstruction algorithm can then computationally retrieve the missing phase of the measured diffraction patterns and reconstruct complex-valued expressions for the object and the illumination source. Ptychography has been investigated extensively in the EUV [35, 39, 43, 48, 49, 57, 161–165] and X-ray ranges [61, 166–168], and has been proven to be a robust method to image both the object and the illumination, called probe hereafter, in principle without the necessity for support constraints or other prior knowledge.

In HHG a number of high harmonics of the driving laser field are generated. This large bandwidth in principle allows for broadband imaging, which can reveal element-specific information of a sample due to the material-specific transmission windows in the EUV spectral range [119]. However, the polychromatic beam lacks the necessary longitudinal coherence for diffraction-based methods such as ptychography. In many recent works, coherence is achieved by spectrally filtering the HHG beam and selecting a single harmonic [35, 43, 163, 165], which is effective for single-wavelength object reconstruction, but removes the ability for spectroscopic imaging. Retrieving full spectral information from broadband diffraction can be achieved through two-pulse Fourier-transform methods [169, 170], but the need for two coherent sources and the required temporal scanning make this concept challenging to combine with ptychography. A more efficient and flexible approach is multi-wavelength ptychography [46, 48, 49, 162, 168, 171, 172]. In multi-wavelength ptychography, the probe and object are typically modeled as a set of incoherent modes, similar to the mixed states approach for partially coherent beams [38], with each mode corresponding to a different wavelength. However, due to the presence and the necessity to reconstruct complex-valued expressions for all probe and object modes, the demands on the reconstruction algorithm become increasingly challenging.

Experience from earlier works has shown that structured illumination improves the reconstruction quality and algorithm convergence [35, 54, 116, 173–177]. A structured beam provides higher illumination NA and reduces the dynamic range of the diffraction pattern, which leads to more efficient use of the full chip of the camera. For ptychography with HHG beams, structure can be accomplished either by structuring directly the EUV beam with the use of a mask [35, 54, 61] or a phase-shifting diffuser in the beamline [113] or indirectly by structuring the driving laser beam, which transfers amplitude and phase properties to the high harmonics [178, 179]. A specific example of such phase transfer is the upconversion of beams carrying orbital angular momentum (OAM) [180–189], for

which it was shown that the q^{th} harmonic of a driving beam with OAM l_1 will have an OAM of $l_q \approx q \cdot l_1$, with the exact OAM depending on the fundamental beam properties [187, 188]. Wang *et al.* [36] showed that ptychography on periodic structures can be improved significantly by using an EUV beam with nonzero OAM, as its large intrinsic divergence leads to overlapping diffraction orders in the far field.

In addition to the amount of structure in individual diffraction patterns, a key aspect of ptychography is the diversity between scan positions. Similarly, multimode ptychography can be expected to benefit in situations where the diffraction resulting from different modes is clearly distinct. Especially when such modes are well-defined physical states, such as different wavelengths, it should be possible to engineer the illumination such that the resulting diffraction data can be more accurately processed by multimode ptychography algorithms.

In this paper we investigate and experimentally demonstrate the improvement in ptychographic multi-wavelength reconstructions with directly and indirectly structured HHG probe beams compared to smooth Gaussian beams. To systematically explore the suitability of a probe for a given object and experimental ptychographic setup, we introduce the concept of diversity in the diffraction patterns and use dissimilarity metrics [190] to characterize our probes. We observe a strong correlation between these diversity metrics and the achieved image reconstruction quality. Based on these observations, we conclude that analyzing and optimizing diversity between wavelengths (or other modes) is an important aspect in the design of any multimode ptychography experiment.

4.2 Diversity considerations

In multi-wavelength ptychography the reconstruction algorithms are usually based on PIM [46], which models measured polychromatic diffraction data as an incoherent sum of individual monochromatic diffraction patterns. For objects with grating-like structures, probe modes corresponding to different wavelengths have distinct diffraction angles and illuminate different areas of the detector [49, 191], which facilitates the reconstruction algorithm to identify the monochromatic components of the polychromatic diffraction pattern. However, for general imaging purposes, objects with arbitrary features do not guarantee spectral diversity. This creates a challenge for the reconstruction algorithm to reliably converge and accurately reconstruct all probe and object modes. Here we explore the influence of illumination diversity on successful ptychographic reconstructions.

The concept of diversity enhancement is illustrated in Fig. 4.1. We consider a binary object illuminated by an EUV beam consisting of the 27^{th} and the 29^{th} harmonic of a 1030 nm wavelength drive laser, with either low or high diversity. The two harmonic beams are assumed to have equal photon flux for both diversity cases. As a low-diversity beam we assume a flat wavefront with top-hat intensity distribution for both wavelengths (Fig. 4.1a)), while for high diversity we consider a beam with similar intensity profiles but having an OAM phase proportional to the harmonic order (Fig. 4.1b)). We model the propagation of the two-color beams from the sample plane to a camera plane that is placed in the far field. Figures 4.1c) and 4.1d) show images of the difference between

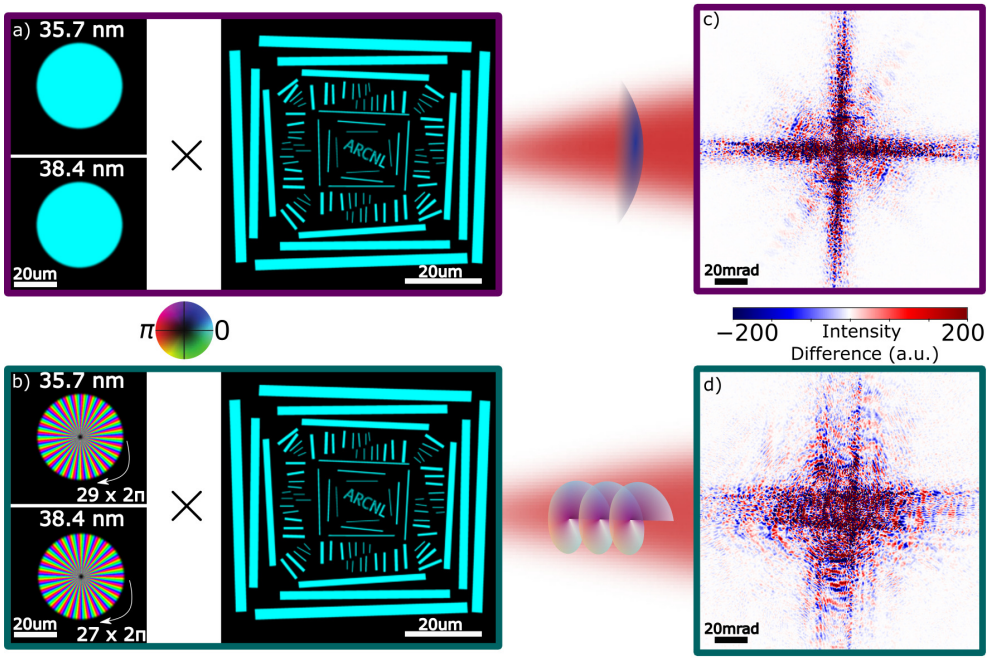

Figure 4.1: Spectral diversity in diffraction. (a, b) A binary object is illuminated by a beam containing the 27$^{\text{th}}$ and 29$^{\text{th}}$ harmonics (at 38.4 nm and 35.7 nm wavelength), either with (a) a flat intensity and phase or (b) with order-dependent OAM. (c, d) Difference of the monochromatic diffraction patterns between the two wavelengths ($I_{35.7nm} - I_{38.4nm}$) for (c) flat and (d) OAM beam illumination. The dynamic range of the camera is set to ≈20-bit and 15-bit for the flat beam and OAM beam respectively such that the number of photons in the incoherent sum of the monochromatic diffraction patterns is equal to 2.27×10^8 photons in both cases.

the two wavelength components in the far-field diffraction patterns for the flat and OAM beam respectively in a saturated dynamic range in order to highlight the differences. It is clear that the diversity introduced by the wavelength-dependent OAM phase leads to strongly enhanced differences in diffraction between the modes.

The diversity in diffraction patterns can be quantified using various dissimilarity metrics [190], such as the *L1* norm, the *L2* norm, the *cosine* metric and the *Jensen-Shannon divergence* (JSD). The former three metrics treat the $N \times N$-sized diffraction patterns as one-dimensional vectors with size equal to N^2 and calculate the distance or angle between the vectors. JSD is a metric borrowed from information theory that compares two or more probability density functions (PDFs). To evaluate the JSD we treat each diffraction pattern as the PDF of the diffracted beam over all detector pixels. The mathematical expressions for these metrics are:

$$D_{p-norm} = \frac{\left(\sum_{x,y} |I_1(x,y) - I_2(x,y)|^p\right)^{1/p}}{\max_{k\in[1,2,\ldots,K]}\left(\sum_{x,y}\left(I_k(x,y)\right)^p\right)^{1/p}} \tag{4.1}$$

$$D_{cosine} = 1 - \frac{\sum_{x,y}\left(I_1(x,y)\cdot I_2(x,y)\right)}{\left(\sum_{x,y} I_1(x,y)^2\right)^{\frac{1}{2}}\left(\sum_{x,y} I_2(x,y)^2\right)^{\frac{1}{2}}} \tag{4.2}$$

$$D_{JSD} = S\Big(\sum_{j=1}^{2}\frac{1}{2}I_j\Big) - \sum_{j=1}^{2}\frac{1}{2}S(I_j) \tag{4.3}$$

where $p = 1$ or $p = 2$ for calculating the diversity according to L1 or L2 norm respectively, K is the number of scan positions, I is the diffraction pattern for a scan position and $S\big(I(x,y)\big) = \sum_{x,y} I(x,y)\log I(x,y)$, with $\log\alpha$ the natural logarithm of α, is the spatial entropy functional as defined in [48]. The cosine metric and JSD are bounded metrics with $0 \leq D_{cosine} \leq 1$ and $0 \leq D_{JSD} \leq \log 2$. The L1 norm and L2 norm are instead unbounded metrics and the absolute values of distances give practically no information about the similarity of two diffraction patterns, as they depend on the dynamic range that is assumed for the calculation of the norms. For this reason, we use a relative L1 norm and L2 norm metric, which are normalized with respect to the largest magnitude in the diffraction pattern series. The relative norms, albeit still unbounded, give more insight about the similarity of two diffraction patterns. Using these metrics, we can compare pairs of monochromatic diffraction patterns at a single scan position and calculate the *spectral diversity*. Similarly, we can compare pairs of polychromatic diffraction patterns that correspond to two adjacent scan positions in the ptychographic measurement and compute their *scanning diversity*.

Scanning diversity, where each additional scan position contributes new information to the ptychographic reconstruction algorithm, is highly beneficial. This is because the robustness of ptychography relies on the aggregated information from diffraction patterns recorded at partially overlapping areas of the object. With HHG beams it is challenging

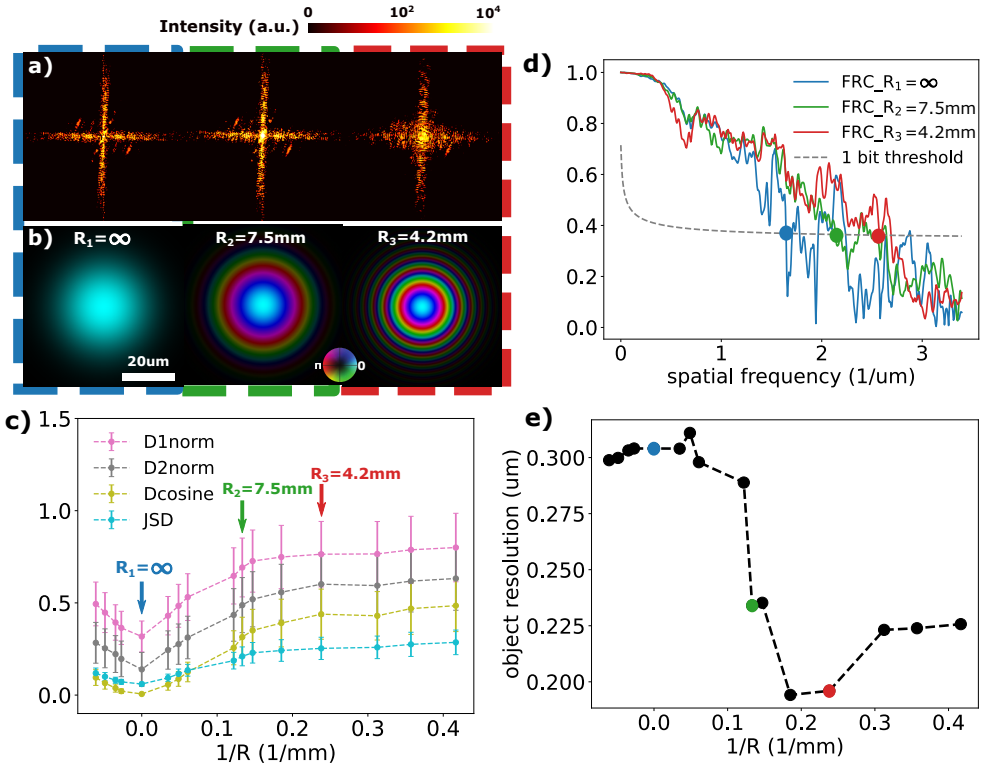

Figure 4.2: Scanning diversity and reconstruction quality of simulated datasets. a) Logarithmic scale diffraction patterns are shown for beams with radii of curvature $R = \infty$, $R = 7.5$ mm, and $R = 4.2$ mm, all illuminating the center of the object at scan position 0. b) Three monochromatic probes at 38.25 nm wavelength with increasing quadratic phase and identical Gaussian intensity profile (30.5 μm $1/e^2$ diameter). c) Diversity metrics $D_{1\,norm}$, $D_{2\,norm}$, cosine and JSD by comparing diffraction patterns between adjacent scan positions for a scan grid with the first 20 scan points, as a function of the quadratic phase of the probe. d) The example FRC by comparing independent reconstructions within the datasets of three monochromatic probes. The intersection of FRC curves and one-bit threshold line determines the object resolution. e) Reconstruction quality calculated from the FRC as a function of the quadratic phase of the probe. The colored dots are extracted from d).

to isolate the effects of spectral and scanning diversity in an experiment, and to tune the amount of diversity in a continuous way. To get more insight in the diversity provided by structuring the HHG beam, and the subsequent improvement in the reconstructions, we performed a series of numerical simulations. In these simulations we consider an object that is illuminated by a monochromatic Gaussian-shaped probe beam with increasing divergence, keeping all other relevant parameters constant (beam size: 30.5 μm; scanning pattern: concentric, 200 scan positions; overlap: 87%; photon flux of probe: $8.4{\times}10^8$ photons; distance between object and detector: 105 mm; probe wavelength: 38.25 nm; noise statistics: mixture of Poisson and Gaussian $\mathcal{N}(0, 50)$.) Probe divergence can be considered as a simple, continuously tunable version of spatial beam structure, resulting in similar diversity variation as observed for the binary masks and OAM beams that we study experimentally (see below). Since the actual object is known, the quality of ptychographic reconstruction can be calculated with the FRC for the object [192]. The object used in simulation is shown in Fig.4.1. The examples of probes with increasing quadratic phase and the corresponding diffraction patterns are given in Figs. 4.2a-b).

The magnitudes of the various diversity metrics as a function of beam divergence are shown in Fig. 4.2c). The diversity is calculated by comparing diffraction patterns from adjacent scan positions. We observe that all diversity metrics exhibit a similar trend with slight variations: the lowest diversity occurs when the object is illuminated by a flat wavefront, while diversity stabilizes after a certain degree of curvature is added to the beam phase. For each probe curvature, we performed independent ptychography reconstructions, with the achieved object resolution determined using FRC. As examples, Fig. 4.2d) shows the FRC results of three beams with increasing quadratic phase, demonstrating that the achieved resolution improves as beam divergence increases. Figure. 4.2e) summarizes the achieved object resolution. As beam divergence increases, diversity between the diffraction patterns also improves. Consequently, the aggregated information from diffraction patterns recorded during each scan position increased. Therefore, we attribute the better reconstructions obtained with more divergent beams to the higher scanning diversity they provide.

4.3 Results

4.3.1 Experiment design

To test the use of diversity metrics in ptychography, we designed a series of experiments in which we perform multi-wavelength ptychography in the extreme-ultraviolet wavelength range, while introducing varying degrees of diversity both between the different wavelength components and scan positions. We use HHG as the illumination source, as it naturally provides coherent EUV radiation at multiple wavelengths in parallel. The concept extends to other broadband EUV sources such as pink beam synchrotrons and free-electron lasers. To control the amount of diversity, we use two ways to structure the illumination beams, as schematically indicated in Fig. 4.3. The first approach is the introduction of a binary mask in the HHG beam just before the imaging target. This

mask leads to a finely structured beam at the object location, thus increasing the scanning diversity. In addition, the diffraction from the mask leads to increased spectral diversity at the object location as well. The second approach is to structure the HHG radiation by shaping the fundamental laser beam. Here we use the property of the HHG process that OAM is upconverted in an order-dependent way, which naturally leads to a large spectral diversity at the object location while maintaining efficient HHG. The rapid angular phase profiles of these OAM beams also result in a high scanning diversity. With these different HHG beams, we perform ptychography scans on a resolution test chart. The resulting data is reconstructed using our PIE-based algorithm [193] and analyzed to determine the link between diversity and image reconstruction quality.

4.3.2 Experimental setup

The experimental setup is shown in Fig. 4.3a). A NIR laser is focused in an argon gas jet to generate high harmonics. Detailed information about the HHG source is given in Appendix 4.6.1. Before the focusing lens we can insert a spiral phase plate (Vortex Photonics V-1064-20-1 [194]) in the beamline to generate a vortex fundamental beam with OAM equal to 1.

Behind the gas jet, a 200 nm aluminum membrane filters out the fundamental beam and the high harmonics are directed and focused by a pair of plane and curved (ROC=500 mm) multilayer mirrors onto the sample. A secondary sample stage is placed at 1.62 mm distance in front of the sample plane, allowing us to place a binary beam-structuring mask or a circular aperture with 50 μm diameter. The binary mask consists of a set of 2 μm holes oriented in a slightly distorted periodic grid separated by an average distance of 5 μm. The 50 μm aperture acts as a spatial filter for the EUV Gaussian beam and minimizes the leakage of the fundamental beam on the camera, while no mask or aperture is used for the vortex beam measurements. As the Gaussian beam at the focus is smaller compared to the structured beams, the measurement with the Gaussian probe is performed with the sample placed 4 mm behind the focus, where the beam has expanded to a comparable size with respect to the focused vortex or mask-structured beam.

The imaging object is a home-built USAF-1951 resolution target with printed logos of VU and ARCNL at the center of the target (Fig. 4.3h)). It is oriented in a 45-degree configuration so that the diffraction of the bars is along the diagonal of the camera, where the detection NA is maximized. A typical multi-spectral HHG diffraction pattern corresponding to illumination of the central area of the sample is shown in Figs. 4.3i-k) for the three considered beams (Gaussian, vortex, structured), assuming equal photon budgets for the three beams. From the individual polychromatic diffraction patterns it can be seen that the vortex beam leads to the highest NA data, as the diffraction pattern has spread to higher angles on the detector. However, we expect that the overall reconstruction quality is not merely a function of the effective NA, but it will be described more completely by the spectral and scanning diversity metrics.

Figure 4.3g) shows the EUV spectrum, measured from the diffraction of the HHG beam through a transmission grating with 500 nm pitch (solid line) and compared with

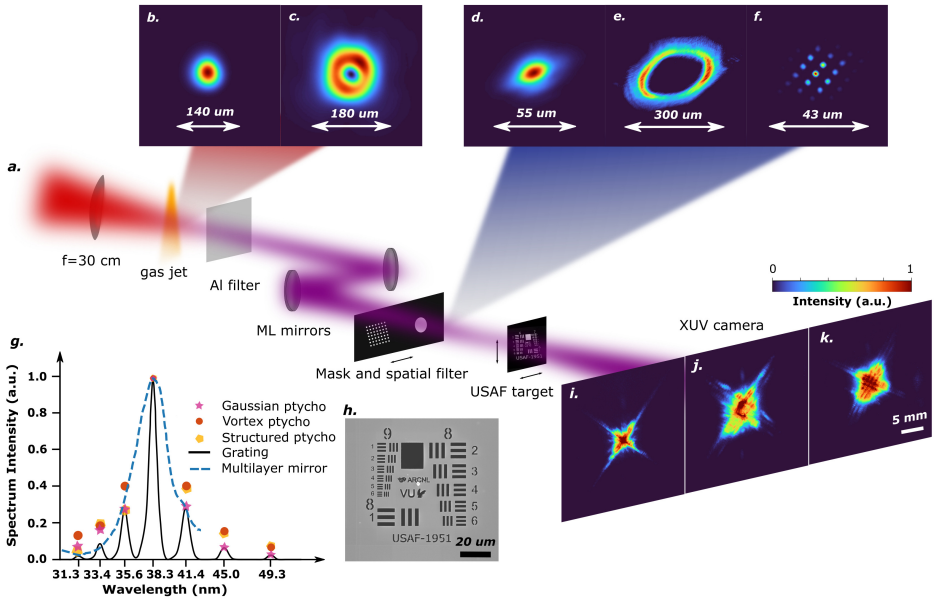

Figure 4.3: Experimental setup. (a) The driving NIR laser is focused by a $f = 300\,\text{mm}$ focal length lens into an argon gas jet. An Al filter blocks the fundamental and the high harmonics are refocused by a pair of broadband multilayer mirrors onto the sample. A CCD camera is placed approximately 10 cm from the focal plane. (b, c) Intensity profile of the driving laser at the gas jet plane for generating (b) Gaussian and (c) OAM EUV beams. (d-f) Polychromatic beam intensities for (d) Gaussian, (e) vortex, and (f) structured beam, computed upstream from the sample plane at distances 8.1 mm, 6 mm, and 1.625 mm (mask plane), respectively. (g) Measured and reconstructed spectrum of the EUV radiation after the mirrors, plotted along with the reflectivity curve of the EUV mirrors. (h) Scanning electron microscope image of the imaging target. (i-k) Polychromatic diffraction patterns from illumination of the central part of the object with (i) Gaussian, (j) vortex, (k) structured beam.

the spectral weights of the reconstructed probes shown in the next section. The Gaussian-shaped envelope of the spectrum has been formed by the efficiency of the EUV mirrors (dashed line in Fig. 4.3g)) that favour the reflection of the 27$^{\text{th}}$ harmonic (38.3 nm), while harmonics 25 and 29 have about three times lower first-order diffraction signal on the camera, and harmonics 23 and 31 have about ten percent of the signal strength of the brightest harmonic.

4.3.3 Ptychographic imaging with different probes

In order to have a fair comparison for the reconstruction quality of ptychographic imaging experiments with different beam types, it is important that other experimental settings, such as sample to camera distance, illumination overlap between adjacent scan positions and probe energy are identical. However, in practice the distance between object and camera is slightly different for measurements with different beam types, and varies between 104.8 mm and 108 mm to achieve a desired beam size at the sample plane. The variation in the distance leads to a 3% variation of the achievable diffraction-limited resolution. Moreover, in order to maximize the captured information from each ptychography scan, we aimed for the utilization of the full dynamic range of the camera via adjusting exposure times and preamplification gain of the camera. This strategy inevitably leads to unequal photon budget of the diffraction patterns for different beam types, as smooth beams more readily saturate the zeroth order diffraction at the center of the camera. A possible solution to this issue would be high dynamic range exposures [36, 162, 164, 195] during the measurement of the Gaussian beam, which however significantly increases measurement time, and increases long-term drift and stability requirements.

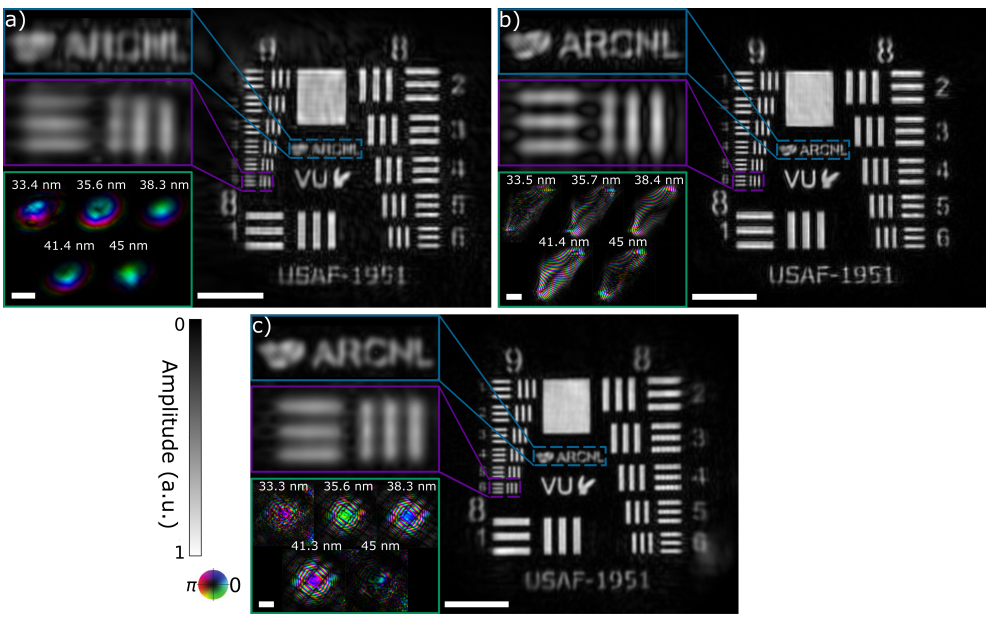

Figure 4.4: Reconstruction results from ptychographic measurements for (a) Gaussian, (b) vortex, (c) structured probes. Right: amplitude of reconstructed objects; top left: zoomed-in areas of the object; bottom left: dominant modes of the reconstructed probes of the five brightest harmonics. Scale bars in all figures correspond to 20 μm.

The ptychographic datasets for the Gaussian and vortex beams consist of 218 scan positions in a concentric scan grid with 6 μm step size and 104 μm field of view. For the structured beam we used a scan grid with smaller step size (2.45 μm) and field of view (44 μm) due to an underestimation of the probe size. Due to the irregular intensity profile of the non-smooth beam types, characterization of the overlap with a linear overlap factor $1 - \frac{\text{step size}}{\text{beam diameter}}$ [196] is not accurate. Therefore, we have defined the overlap as the two-dimensional average cross-correlation of a binarized version of the polychromatic beam with a translated version of itself to an adjacent scan position. According to this definition, the overlap is equal to 74% with a standard deviation of 5.8% for the Gaussian beam, 68% with a standard deviation of 8.3% for the vortex beam and 88.6% with a standard deviation 10% for the structured beam.

Figure 4.4 shows the reconstruction results from the ptychography measurements with the three different beam types. These results were obtained using two incoherent probe modes for each wavelength, similar to [57], in order to account for decoherence and other sources of noise in the forward model [35, 57]. To reduce the complexity of the problem, we constrained the object to look identical for all wavelengths, given that we use a binary, non-dispersive object. More details on the PIE-based reconstruction algorithm and the reconstruction results are given in Appendices 4.7 and 4.8 respectively. The reconstruction quality of the object upon vortex and structured beam illumination is clearly better than for Gaussian beam illumination, with fewer artifacts and sharper edges. Since the reconstructions give complex-valued expressions for the both the object and the probe, the object has been numerically propagated to remove a defocus term that is caused by calibration errors of the wavelengths or the sample to camera distance.

In Fig. 4.4 we also show reconstructions for the dominant mode of the five brightest probes that range from 33.4 nm to 45 nm. The vortex probes are elongated due to the presence of astigmatism, as is explained in more detail in Appendix 4.6.3. For all beam shapes, the spectral weights reconstructed from ptychography are consistent with the grating measurement (Fig. 4.3g)). Small variations are apparent, as the ptychography scan effectively measures the average diffracted radiation flux from the object across the scanned area for all wavelength components. The resulting spectrum may differ from the grating measurement that was acquired by only sampling part of the Gaussian beam. For the smooth beam, the wavefronts of the weaker harmonics have more artifacts and are less trustworthy compared to the weak harmonics of the structured and vortex beam.

The significant difference in the quality of the reconstruction for the smooth beam can be attributed either to the smaller photon budget on the camera or the lower illumination diversity, likely to the combination of the two factors.

4.3.4 Simulations with reconstructed probes under comparable experimental conditions

To determine the cause of the difference in imaging performance and exclude the potential influence of experimental conditions, we set up simulations using the actual reconstructed

probes and the SEM image of the object. In this simulation we ensured identical parameters such as object to camera distance $z = 106.8$ mm, spectral weights, overlap OV=90% and probe energy. Specifically, the probe energy was normalized such that the dataset with the vortex beams would have a 15-bit dynamic range. A combination of Poisson noise and Gaussian noise with standard deviation $\sigma = 40$ counts was added to the ptychograms.

The object and probe reconstructions of the synthetic ptychographic data are shown in Fig. 4.5. The improved imaging results with non-smooth beams (Fig. 4.5e,f,i,j)) compared to results with smooth beams (Fig. 4.5a,b)) remain clear, with similar trends as in Fig. 4.4. Note that there are slight discrepancies between the probes in Figs. 4.4 and 4.5, because the synthetic data were generated based on single-mode reconstructed beams, since no instability or decoherence effects were considered during the simulation. The assumption of perfectly coherent harmonic probes does not influence the hypothesis that is examined during this simulation, of how diversity caused by a structured beam can enhance the reconstructed image quality.

The achieved object resolution is determined using FRC between the true simulated object and one object reconstruction per probe beam and is shown in Fig. 4.4d,h,l). The resolution using the one-bit criterion is equal to 400 nm for the vortex beam, 1251 nm for the Gaussian beam and 414 nm for the structured beam. For the current experimental parameters, the highest achievable, diffraction-limited, resolution is 129 nm, assuming the shortest contributing wavelength component is 33.4 nm.

4.3.5 Characterization of probe diversity

To compare the spectral and scanning diversity for the different beam types, we calculate spectrally resolved diffraction patterns at the detector plane. The probes, object and scan grid are identical to what we used in the simulations presented in Section 4.3.4, so that we can correlate the diversity metrics to the reconstruction results in Fig. 4.5. Moreover, the diversity metrics are calculated based on stable and coherent harmonic beams, without any long-term drifts.

The diversity is calculated according to the dissimilarity metrics presented in Section 4.2, and the results are shown in Fig. 4.6. The diffraction patterns used as input to Eqs. (4.1,4.2) for the calculation of diversity according to L1 norm, L2 norm, and the cosine metric were normalized with respect to the maximum pixel value over the full dataset ($\max_{x,y,k} I_k(x,y) = 1$). We selected this normalization approach as it conserves relative intensity differences among different patterns, which contains relevant information that influences ptychography algorithm performance. On the other hand, for the diversity metric according to JSD (Eq. (4.3)), each diffraction pattern was normalized independently such that $\sum_{x,y} I_k(x,y) = 1$, $\forall k$, in accordance with the original definition of entropy from information theory. Different normalization strategies can be chosen: diversity results for different cases are given in the Appendix 4.9 (Figs. 4.9, 4.10), which show different absolute values but very similar trends.

As shown by the calculated diversity metrics in Fig. 4.6, the vortex beam leads to the largest scanning diversity and spectral diversity, while the structured beam follows closely

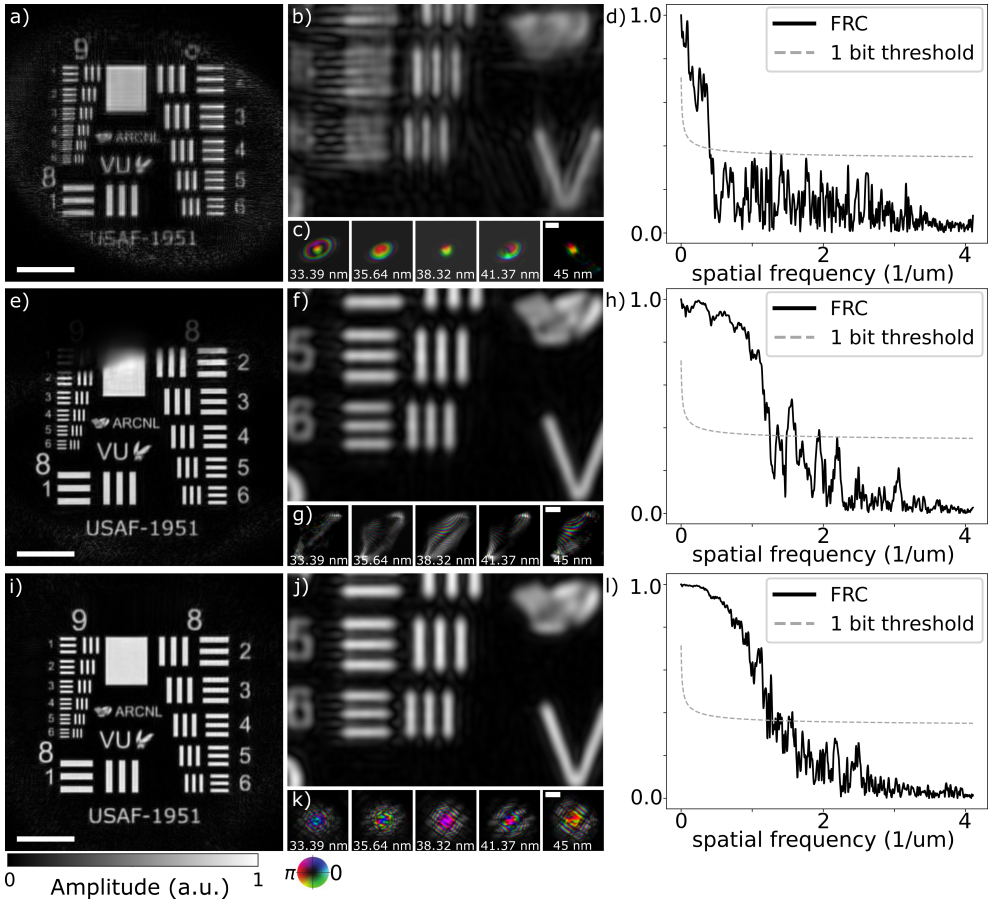

Figure 4.5: Reconstruction results from synthetic ptychographic datasets with (a-d) Gaussian, (e-h) vortex, (i-l) structured probes. (a,e,i) Amplitude of the reconstructed object. (b,f,j) Zoomed-in area of the object group 9/elements 5 and 6. (c,g,k) Probe reconstructions of the five brightest harmonics. (d,h,l) FRC computed by comparing object reconstructions with true object. Scale bars in all figures correspond to 20 μm.

with high diversity values, especially according to cosine metric and JSD. These results are in close agreement with the reconstruction results of Fig. 4.5, where the vortex and structured beams were shown to lead to better object reconstructions than the Gaussian beam. Out of the four different metrics, both the JSD and cosine metrics reflect this difference in ptychography performance, showing significantly higher diversity values for the vortex and structured beams in a way that correlates with the image reconstruction quality. In comparison, the L1- and L2-norms are less clear, showing both larger variance

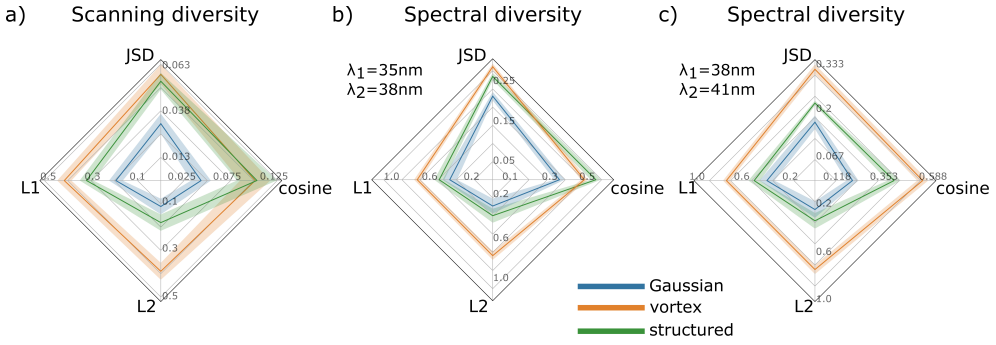

Figure 4.6: Diversity metrics for different probe beam structures. (a) scanning diversity of polychromatic diffraction patterns, (b) spectral diversity between diffraction patterns at wavelengths of 35.6 nm and 38.3 nm, (c) spectral diversity between diffraction patterns at wavelengths of 38.3 nm and 41.4 nm. The solid lines indicate the mean values of comparing adjacent scan positions (for scanning diversity) or wavelengths (for spectral diversity) over the whole diffraction patterns series, while the shaded areas have a width of one standard deviation.

and smaller differences between the beams.

4.3.6 Fisher information analysis

To further analyze the influence of structured illumination on the ptychographic reconstruction quality, we compare the Fisher information for the three previously described and experimentally reconstructed probes: Gaussian, vortex, and structured beam. The Fisher information quantifies the amount of information a measured diffraction pattern contains about an unknown parameter θ, thereby setting a lower bound on the achievable precision in estimating that parameter (the Cramér-Rao lower bound). Given the observed improvement in ptychographic reconstruction quality with increased illumination diversity, it is worth investigating whether this improvement is accompanied by an increase in Fisher information. Such a finding would bolster our claim that the increased diversity in diffraction patterns achieved through structured illumination leads to more informative measurements, which subsequently enable better object reconstructions.

In general, the Fisher information is defined as $\mathcal{J}(\theta) = \mathbb{E}([\partial_\theta \ln p(X;\theta)]^2)$, where $\mathbb{E}$ denotes the expectation operator with respect to noise fluctuations, and $p(X;\theta)$ denotes a probability density function of a random variable X representing the observed data [197, 198]. The term $\partial_\theta \ln p(X;\theta)$ represents the partial derivative of the natural logarithm of the probability density function with respect to the parameter θ. In other words, the Fisher information describes how sensitive the measurement is to changes in θ. This sensitivity is directly related to the concept of diversity in diffraction patterns, as a more

diverse set of patterns can be expected to contain more information about the object and its parameters.

In the case of ptychography, where the measurement noise is assumed to follow a Poisson distribution, the Fisher information associated with the l-th diffraction pattern for a single parameter θ can be expressed as [199]:

$$\mathcal{J}_l(\theta) = \sum_k \frac{1}{I_{k,l}} \left(\frac{\partial I_{k,l}}{\partial \theta} \right)^2 , \tag{4.4}$$

where I_k is the expected photon count at detector pixel k, and the sum runs over all pixels of the detector.

To explore the relationship between structured illumination and Fisher information, we consider two types of object parameters: a dimensionless scaling factor Δs, representing overall changes in the object's size, and a phase shift $\Delta\phi$ in radians, representing changes in the object's optical thickness. We study the same object shape as previously used in section 4.2, but as a transparent phase object instead of a binary amplitude object. Assuming a sample to camera distance of $z = 105\,\mathrm{mm}$ and the same experimental design as used in our experimental setup featuring an HHG source, we can numerically calculate the diffraction patterns for each parameter θ using the multi-wavelength EUV probes that were reconstructed and presented in section 4.3.3. The probe intensities are all normalized to a total photon count of 10×10^6 photons, and the object is scanned through the beams in a concentric pattern comprised of 219 positions. Using a centered finite difference scheme, we can then estimate the Fisher information as

$$\mathcal{J}_l(\theta) = \sum_l \frac{1}{I_{k,l}(\theta) + \epsilon} \left[\frac{I_{k,l}(\theta + \Delta\theta) - I_{k,l}(\theta - \Delta\theta)}{2\Delta\theta} \right]^2 , \tag{4.5}$$

where $\epsilon = 1 \times 10^{-6}$ denotes a regularization parameter with the physical interpretation of the expected value of additive Poissonian noise, and the step sizes $\Delta\theta$ are chosen as $\Delta s = 5 \times 10^{-3}$ for the scaling factor, and $\Delta\phi = 1 \times 10^{-6}$ rad for the phase shift, respectively.

For both object parameters, the Fisher information is shown in Fig. 4.7 independently of each other. To assess the distribution of information across the whole ptychography scan, we visualize the Fisher information per diffraction pattern as violin plots and normalize them by the average information that is achieved by Gaussian beam illumination. For the object scaling parameter s (Fig. 4.7a), we observe a significant increase of information using structured illumination. Specifically, the vortex probe exhibits a total Fisher information about 3.4 times higher than the Gaussian probe. This translates into a reduction in the standard deviation of the estimate for this parameter by about 1.8 times, calculated as the square root of the inverse of the Fisher information (from the definition of the Cramér-Rao lower bound).

This finding supports our expectation that the increased diversity in the diffraction patterns leads to a higher sensitivity to changes of a parameter that is closely linked

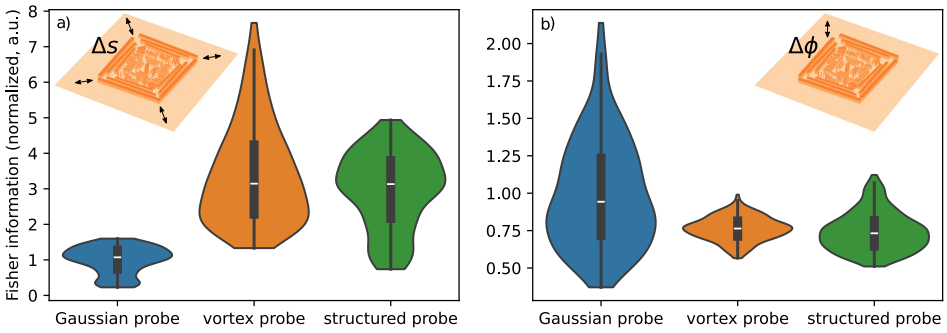

Figure 4.7: Fisher information for different probe beam structures. The shape of the violin plots describes the distribution of Fisher information per diffraction pattern (for a total of 219 scanning positions). The Fisher information is normalized by the average information achievable with a Gaussian probe. (a) Fisher information associated with a parameter s that determines the overall size and scale of the phase object shown as an inset plot. (b) Fisher information associated with the phase ϕ of the phase object shown as an inset plot.

to the faithful reconstruction of the object's size and shape. The scaling factor directly affects the spatial frequencies in the diffraction patterns, which are crucial for achieving high-resolution reconstructions. Moreover, the scaling factor is intrinsically related to experimental parameters such as the wavelength and object-to-detector distance [200]. The enhanced sensitivity to the scaling factor through structured illumination can therefore lead to more accurate and precise object reconstructions, as well as improved retrieval of the experimental geometry from the ptychographic dataset.

Interestingly, we do not observe a significant difference in the Fisher information between structured and unstructured illumination for the phase parameter ϕ (Fig. 4.7b). This suggests that phase sensitivity in ptychography may depend on additional factors beyond beam structure, such as phase matching conditions as discussed in Ref. [201]. It is important to note that estimating the single parameter of the object's phase assumes prior knowledge of its shape. This assumption reduces the complexity of the ptychographic algorithm by alleviating the need to simultaneously retrieve spatial features, which may explain the relative invariance of the achievable estimation precision to the illumination diversity used.

4.4 Discussion

The concept of diversity metrics using diffraction patterns as a means to assess the expected image quality in ptychography is found to work well. Both the diversity among scan positions and the spectral diversity in a multi-wavelength ptychography experiment can be characterized with such metrics. From the Fisher information analysis, it follows

that beams with high spatial and spectral diversity lead to increased sensitivity to spatial properties in ptychography datasets. As a result, ptychography with such high-diversity beams can be expected to lead to better image reconstructions at similar photon numbers and scan times. Although diversity metrics provide less quantitative insight than Fisher information, they consider the overall information content between measurements rather than the sensitivity to single parameters, which makes them well-suited in the assessment of imaging performance. Diversity metrics based on estimated diffraction patterns can therefore provide a way to optimize illumination beam profiles and secondary experimental parameters. From our experiments, we find that the JSD and cosine metric show clear correlation with image quality. These metrics have the additional advantage that they are bounded, meaning that the calculated diversity can be compared to the maximum possible diversity of a given dataset. While this correlation is not a direct predictor of image quality, they do allow a comparison of the expected imaging performance with different beams and objects, giving valuable insight already in the design phase of a ptychography experiment.

In contrast, the L1- and L2-norms show larger variations and less sensitivity to image reconstruction quality for different beams. This is likely due to the structure of these metrics (Eq. 4.1), which are more sensitive to absolute differences in intensity. Therefore, they are less reliable in quantifying structural changes between different diffraction patterns, in which the information for ptychography reconstructions is mainly contained.

Our experiments were designed in such a way that we could compare the spatial and spectral diversity when using beams without structure, with mainly spatial diversity induced by a binary mask, and with mainly spectral diversity through wavelength-dependent OAM. We find that both of these structured beam approaches provide enough spectral and scanning diversity to enable object reconstructions with improved resolution and fewer artifacts. Furthermore, individual probe modes that correspond to different wavelengths of the polychromatic beam are reconstructed in a more robust and reproducible way. While the structured beams indeed lead to improved image reconstructions, an interesting finding is that both types of structuring result in comparable image quality and resolution. A possible explanation is the strong wavelength dependence of far-field diffraction, as a larger separation between diffraction orders results in better wavelength-resolved patterns as well. Strikingly, the spectral diversity between some harmonic orders is actually higher for the binary mask structuring than for the OAM beams (Fig. 4.6b)).

In the present work, the available HHG flux was the limiting factor in the experiments, as the measurements required exposure times that made the ptychography scans susceptible to drifts in beam pointing and ambient changes. In particular for the vortex EUV beam, the required exposure time was almost twice as long as for the diffraction-based structured beam to reach similar flux. This additional measurement time may also have led to a reduced reconstruction quality, which could offset the present conclusions given that the OAM beam shows the highest diversity among all the beams. Improving the HHG flux and using additional long-term stabilization systems would remove these uncertainties. Nevertheless, even though the beam structuring methods reduce the available HHG flux, the increased diversity remains a driver for reconstruction improvements.

First demonstrations of nanoscale-resolution ptychography on dispersive samples

used monochromatic EUV light [35, 43]. The spectrally resolved probe reconstruction with multi-wavelength structured illumination in this work paves the way for broadband imaging of dispersive samples, aided by diversity metrics to design the required illumination profiles. This approach can unlock the full use of the potential of broadband EUV imaging systems for semiconductor wafer metrology and biological materials.

4.5 Conclusion

In conclusion, in this study we introduce diversity metrics in order to quantify the suitability of a coherent illumination type for ptychography experiments. We performed comparative measurements with various multi-wavelength EUV beam types, namely Gaussian, OAM, and structured by diffraction from a binary mask. Both simulation and experimental results verify that increased scanning and spectral diversity of diffraction patterns leads to improved imaging results at a given photon flux and measurement time. These diversity metrics therefore provide an intuitive design guideline for ptychography experiments, enabling a comparison of expected image reconstruction quality for different beam profiles and objects.

4.6 Materials and methods

4.6.1 Drive laser for high harmonic generation

Our table-top HHG source is driven by an ultrafast NIR laser system. With an ytterbium-based laser system (Pharos from Light Conversion) delivering 170 fs pulses at a center wavelength of 1030 nm, 2 mJ pulses are obtained at a repetition rate of 1 kHz. For efficient high-harmonic generation, the pulses are compressed by a home-built post-compression system to a pulse duration ~35 fs with an average power of 1.5 W [202]. The NIR beam is subsequently focused by an $f = 300$ mm lens into an argon gas jet confined in a 1 mm diameter metal tube, at a backing pressure of 5 bar. Moreover, an iris clips the beam before the focusing lens in order to improve the phase matching conditions for HHG.

4.6.2 Sample preparation

The binary USAF 1951 resolution target as used in the experiments is fabricated on a 120 nm thick gold layer sputter coated on a 50 nm silicon nitride free-standing membrane (Ted Pella Inc.). Patterning was performed with a 30 keV focused gallium ion beam (FEI Helios Nanolab 600) with a current of 0.28 nA and dwell time of 1000 ms. SEM image of the USAF is shown in Fig 4.3h). In our case, the sample thickness $\Delta z = 170$ nm and the smallest structure in the sample $\Delta x \approx 0.3\,\mu$m meet the condition $\Delta z < 2(\Delta x)^2/\lambda$, which is referred to here as the projection approximation [203]. Therefore, the sample is mathematically represented by a two-dimensional transmission function, which is obtained by a projection of the refractive index along one spatial dimension.

4.6.3 Extreme ultraviolet optics

The EUV mirrors that have been used for focusing the HHG beams to the sample are molybdenum/silicon multilayer mirrors fabricated by optiXfab GmbH [204]. We use one plane and one curved mirror to steer and refocus the beam respectively. The bandwidth coverage of the mirrors is broadband (20 nm-55 nm) for the plane mirror and narrowband centered at 39 nm for the curved mirror, at an average reflectivity of 20% per mirror.

The indicated angle of incidence for maximized reflectivity is 5 degrees. However, oblique incidence on the curved mirror leads to astigmatism, as can be clearly observed in the ptychographic reconstruction of the vortex probes in Fig. 4.4b). A small amount of astigmatism is also noticeable in the smooth beam reconstruction (Fig. 4.4a)). The induced astigmatism to the wavefront is equal to $\frac{I^2}{2r}(y^2 - x^2)$, with I the incidence angle and r the radius of curvature of the mirror [205]. OAM beams have larger divergence compared to Gaussian beams, so the beam has a larger size on the curved mirror and the effect of astigmatism becomes stronger.

4.6.4 Data acquisition

The EUV camera in our experimental setup (Andor Ikon-L 936SO, 2048×2048 pixels, pixel size 13.5 μm, 15-bit dynamic range) has a constant background offset of approximately 320 counts for unbinned data when cooled to −60 °C. The CCD pixels were read-out at a rate of 1 MHz with preamplifier gain 2× for the vortex and structured beam measurements, where the signal was decreased compared to the smooth beam measurement.

To fully utilize the dynamic range of the camera, we set different exposure times for each measurement, equal to 10 s, 350 ms and 6 s for the vortex, Gaussian and structured beams respectively. This difference in exposure times per diffraction pattern creates different sensitivities to possible beam drifts and spectral jitter. To monitor slow drifts, we recorded a diffraction pattern at one specific scan position several times throughout the ptychographic measurement, as well as the polychromatic bare beam position before and after the measurement, and we did not observe any significant drift for either measurement. Spectral and pointing jitter can lead to blurring of the diffraction patterns, especially for long exposure times. The jitter can be modelled as a degree of incoherence in the beam, which we treated algorithmically by decomposing each high harmonic wavefront into incoherent modes. Given the limited amount of jitter, we found that using two modes is sufficient for ptychographic reconstruction.

The sample is mounted on a three-dimensional translation stage (Smaract SLC-1730). The translation lateral to the beam is required to perform ptychography scans and the longitudinal translation allows us to select a desired beam size and divergence at the sample plane.

4.7 Ptychographic reconstruction algorithm

The ptychographic reconstructions were performed with Ptylab.py [193]. In Ptylab, the PIM [46] algorithm has been implemented to describe the measured far-field diffraction pattern at position j as the incoherent sum of monochromatic diffraction patterns. For the specific experimental settings of Fig. 4.3 we have modified the general forward model expression to the following:

$$I_j \sim \sum_{\Lambda} \sum_{k\in\{0,1\}} \left(\mathscr{P}_{\Lambda}[P_{k,\Lambda}(\mathbf{r}) \cdot O(\mathbf{r}-\mathbf{r}_j)]\right)^2 + I_B$$

where Λ denotes the wavelength, k refers to the incoherent mixed states of each probe that account for sources of decoherence [35], the binary object O is identical for all wavelengths and $\mathscr{P}_{\Lambda}$ is the scaled angular spectrum propagator [149, 193] that permits the propagation of an electromagnetic wave under the Fresnel approximation [96] with wavelength-independent pixel size at the object plane. The mixed states of the probes are orthogonalized during the reconstruction via singular value decomposition. In Fig. 4.4 we show the probes with the highest singular values that correspond more to the physical representation of the beams, while for all simulations we do not use mixed states. Furthermore, the general forward model expression allows for the object to be different for every wavelength, but in our demonstration we have simplified the formula by using a single object that looks identical for all wavelengths. The phase plots of the object shown in Fig. 4.8 verify that the object is binary and there is no requirement for considering different object representation for each wavelength. I_B is a constant background, iteratively updated according to [206], that is added to the forward model in order to take into account leakage of the fundamental beam to the detector. The update rules in the $(n+1)^{\text{th}}$ iteration for probe and object are then, according to [46, 193]

$$P_{n+1,k,\Lambda}(\mathbf{r}) = P_{n,k,\Lambda}(\mathbf{r}) + \beta_P \cdot \frac{O_n^*(\mathbf{r}-\mathbf{r}_j)\big(\psi - P_{n,k,\Lambda}(\mathbf{r})O_n(\mathbf{r}-\mathbf{r}_j)\big)}{\alpha_p|O_n(\mathbf{r})|^2_{max} + (1-\alpha_p)|O_n(\mathbf{r}-\mathbf{r}_j)|^2}$$

$$O_{n+1}(\mathbf{r}-\mathbf{r}_j) = O_n(\mathbf{r}-\mathbf{r}_j) + \beta_O \cdot \sum_{\Lambda}\sum_{k} \frac{P^*_{n,k,\Lambda}(\mathbf{r})\big(\psi - P_{n,k,\Lambda}(\mathbf{r})O_n(\mathbf{r}-\mathbf{r}_j)\big)}{\alpha_o|P_{n,k,\Lambda}(\mathbf{r})|^2_{max} + (1-\alpha_o)|P_{n,k,\Lambda}(\mathbf{r})|^2}$$

Since we use a single object representation for all wavelengths, we have modified the update rule given in [193] accordingly. Specifically, the update for the object is derived via the accumulated gradients from all spectral and decoherence modes of the probe. Moreover, for the reconstructions shown in Fig. 4.4, the regularization parameters α_p and α_o, which were first introduced in [110], were chosen equal to 0.99 in order to penalize updates of pixels with low signals, $\beta_p = 0.3$ and β_o was adjusted manually during the reconstruction from 0 to 0.3. Since the polychromatic beam on the camera plane was recorded before each ptychographic measurement, we implemented the modulus enforced probe technique [58] within the reconstruction process. A good initial guess based on

earlier reconstructed results was used for the object in the results shown in Fig. 4.4, but the algorithms also converged with slightly worse performance if prior knowledge was assumed only for the probes and not for the object.

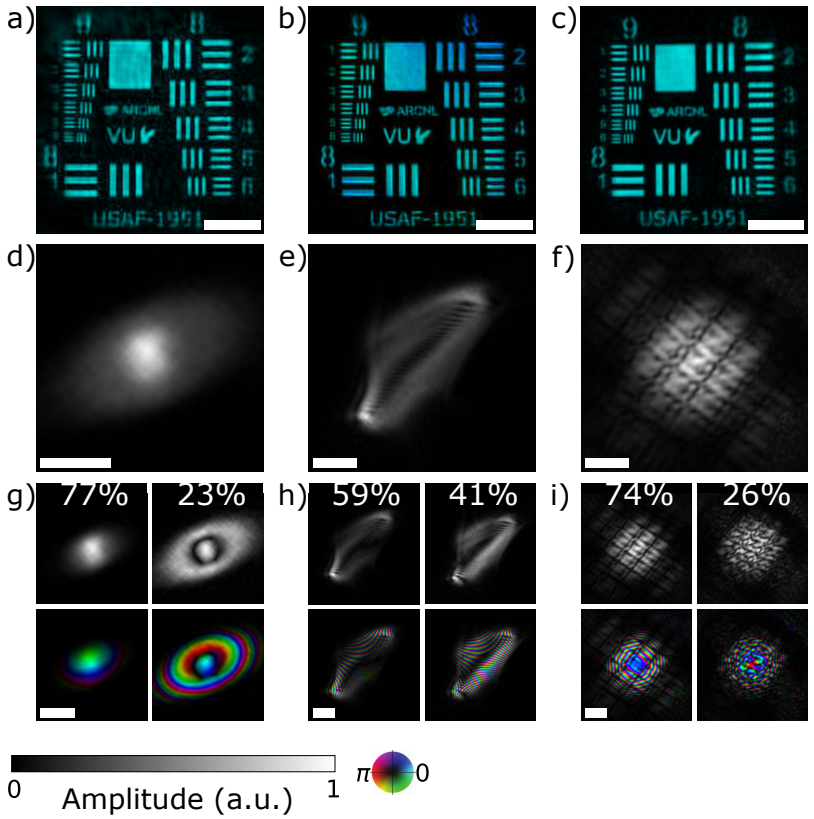

Figure 4.8: Complementary object and probe reconstructions for experimental data. (a-c) Complex-valued representations of the reconstructed object for (a) Gaussian, (b) vortex and (c) structured beam. (d-e) Amplitude of the partially coherent 27$^{\text{th}}$ harmonic (38.3 nm) beams at the object plane. (g-i) Amplitude and complex-valued plots of the incoherent modes of the 27$^{\text{th}}$ harmonic. In all complex-valued plots, brightness corresponds to amplitude and hue to phase. Scale bars in all figures are equal to 20 μm.

4.8 Additional information about the reconstruction of experimental data

4.8.1 Object reconstruction

In ptychography the imaging results are typically complex-valued expressions for the probe and object that correspond to the laser beam amplitude and phase and to the transmission (or reflection) function of the sample under examination. In this work we demonstrated our concept in a binary sample that is either fully opaque or fully transparent to all wavelengths. However, the reconstruction algorithm was not restricted to converge to a real-valued object. The complete object reconstruction results, after numerical propagation that remove any defocusing effects, are shown in Figs. 4.8a-c) for the three tested beam cases. We observe that indeed the algorithm has converged to a flat-phased object reconstruction for all beam cases, with only a minor residual phase variation of ≈0.65 rad at the edge of the object when illuminated by a vortex beam.

4.8.2 Probe reconstruction

As mentioned in Section 4.3.3 and Appendix 4.7, during the reconstruction we use two incoherent probe modes, also called mixed states, per wavelength. Figures 4.8d-f) show the amplitudes of the incoherent sums of the modes of the 27^{th} harmonic (38.3 nm) for the three different beam types, which correspond to a physical representation of the beam amplitude at this wavelength. We observe that both proposed methods to structure the HHG beam (diffraction mask-based and introducing OAM) lead to highly structured beam profiles. Finally, Figs. 4.8g-i) show amplitude and complex-valued plots of the incoherent probe modes of the 27^{th} harmonic, with the percentage of the total energy that is included in each mode.

4.9 Diversity metrics under different normalization strategies

The diversity metrics that have been used throughout this work, namely the L_1, L_2 norms, the cosine metric, and Jensen-Shannon divergence (JSD), were proposed by Iwasaki et al. [190] as appropriate to describe similarity between diffraction patterns, but originally have been defined and used in other disciplines. The L_p norms measure distance between vectors, making the results strongly dependent on the magnitude of the vectors, which in this application translates to the absolute intensity of the diffraction patterns. The cosine metric only measures the angle between two vectors, giving a result that is independent of any arbitrary scaling of the vector magnitudes. The JSD, on the other hand, has been defined as similarity metric between probability density functions (PDFs), so the two diffraction patterns that are inputs in the JSD equation need to be normalized accordingly, such that the integrated intensity over the whole detector area is equal to 1. If we abide

by this normalization, JSD is a bounded metric, with the supremum $JSD_{max} = log2$ indicating maximum diversity.

For ptychography, the absolute value of the signal is an important parameter for successful reconstructions, as high pixel values imply better signal-to-noise ratio (SNR), although this aspect is not specifically relevant for diversity. However, it certainly affects the reconstruction quality if within the diffraction patterns series there are many low-signal diffraction patterns that mathematically give high diversity, but practically do not contain any significant information due to the low SNR. Therefore, it is relevant to assess the effect of including diffraction signal strengths in the diversity metrics on the achieved reconstruction quality.

Figure 4.4 in the main text shows L_1, L_2, and cosine results for normalization of the diffraction patterns such that the maximum pixel value over the whole series of diffraction patterns is equal to 1. This approach ensures that relative intensity variations among the diffraction patterns are included in the diversity metrics. For JSD a different choice was made, and each diffraction pattern has been normalized individually such that $\sum_{x,y} I(x,y) = 1$, in order to be consistent with the definition of entropy. In addition to this choice of normalization, we can consider alternative normalization methods to calculate both scanning and spectral diversity, and investigate their effect on the different metrics and their correlation to the ptychographic image reconstruction results. The normalization procedures that we considered can be listed as follows:

1. Global normalization: normalize all diffraction patterns that correspond to different scan positions (and different wavelengths if applicable) by the same number, such that $\max_{x,y,k} I_k(x,y) = 1$, with $x, y \in [1,N], k \in [1,K]$

2. Local normalization: normalize each diffraction pattern that corresponds to a different scan position (and a different wavelength if applicable) individually, such that $\max_{x,y} I_k(x,y) = 1$, with $x, y \in [1,N], k \in [1,K]$

3. Local normalization on total flux: normalize each diffraction pattern that corresponds to a different scan position (and a different wavelength if applicable) individually, such that $\sum_{x,y} I_k(x,y) = 1$, with $x, y \in [1,N], k \in [1,K]$

4. Local normalization including spectral weights: normalize two monochromatic diffraction patterns that correspond to the same scan position by the same number, such that $\max_{x,y,\lambda} I_{k,\lambda}(x,y) = 1$, with $x, y \in [1,N], k \in [1,K], \lambda \in \{\lambda_1, \lambda_2\}$

where K is the number of scan positions and $N \times N$ is the size of the detector.

In Figs. 4.9, 4.10 we show results of scanning and spectral diversity respectively for these different normalization strategies as applied to all four metrics. The results indicate that the L_1 and L_2 norms are very sensitive to the normalization strategy, even to the point where their difference becomes insignificant when using local normalization (Fig. 4.9b)). We attribute this behaviour to the situation as described above, where the local normalization results in an increased weight of low-intensity diffraction patterns on the diversity metrics. As such low-intensity patterns contain significant noise, overestimating

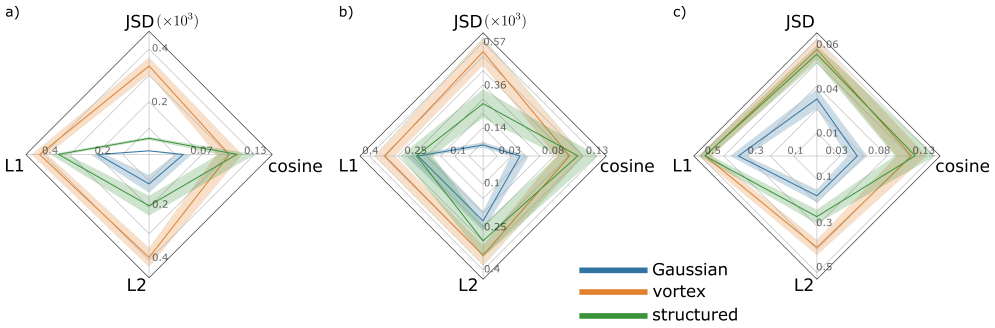

Figure 4.9: Scanning diversity metrics for different normalization strategies. (a) Global normalization, (b) Local normalization, (c) Local normalization on total flux. The solid lines indicate the mean values of comparing adjacent scan positions for scanning diversity over the whole diffraction patterns series, while the shaded areas have a width of one standard deviation. Note the different horizontal and vertical scales.

their weights will lead to higher diversity estimates, as white noise in principle has very high diversity between separate measurements. Therefore, when using L_p norms as a diversity metric, global normalization is required to properly account for true signal variations across the ptychography scan. In contrast, the cosine norm is independent of the normalization, which is to be expected as the angle between vectors is not affected by relative amplitude differences. This feature makes the metric more robust against the choice of normalization and therefore more flexible. However, its independence of the magnitude may form a limitation, as it may become less clear how to identify the influence of low SNR in a ptychography dataset. As long as data of sufficiently high SNR can be guaranteed, the cosine metric is a suitable way to assess diversity in a dataset.

The JSD is quite different from the other considered metrics, as it does not consider measurements as vectors, but rather as probability distributions. Diversity is then quantified as the difference in information content instead of norms or projections of vectors. This concept seems naturally suited to assess diversity in measured diffraction 'information', but does require a different treatment to allow such an interpretation. Interpreting a diffraction measurement as a probability distribution requires the total probability of all registered events to add up to one. This corresponds to the approach of local normalization on flux, as used in Figs. 4.9c) and 4.10d). With this approach, the JSD is a bounded metric with a clear interpretation of diversity in terms of new information added by each next diffraction pattern, which is clearly attractive for experiment design and analysis. However, such a local normalization approach does have the risk of becoming too sensitive to noise when there are many low-SNR diffraction patterns in a dataset, as was discussed above for the L_p norms. Therefore, one could argue that JSD with a global normalization approach has advantages, as it significantly reduces this noise sensitivity. Comparing the JSD results in Figs. 4.9 and 4.10, we find that the trends in JSD for our datasets are largely independent of the chosen normalization, although the variance is

significantly reduced for global normalization. This does make it easier to assess trends in JSD, but global normalization removes the absolute upper bound and reduces the JSD to a relative metric.

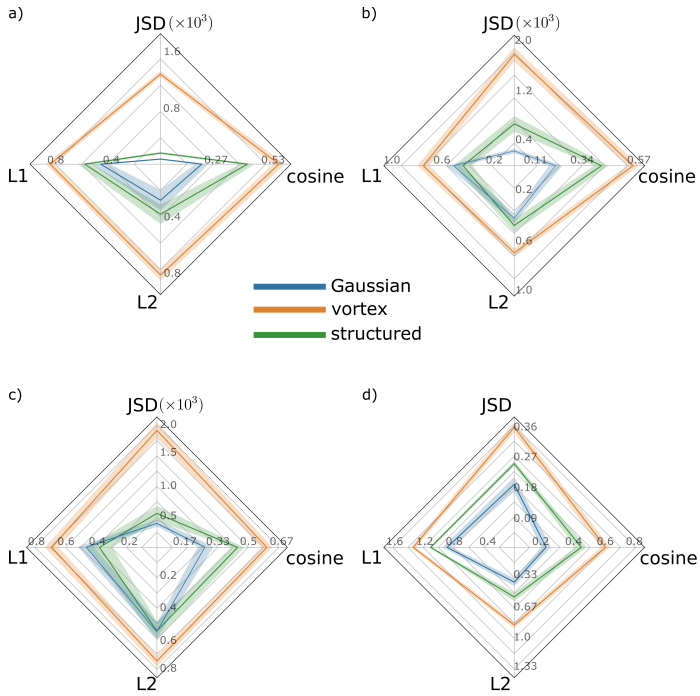

Figure 4.10: Spectral diversity metrics for monochromatic diffraction patterns at 38.3 nm and 41.4 nm for different normalization strategies. (a) Global normalization, (b) Local normalization, (c) Local normalization including spectral weights, (d) Local normalization on total flux. The solid lines indicate the mean values of comparing wavelengths over the whole diffraction patterns series, while the shaded areas have a width of one standard deviation. Note the different horizontal and vertical scales.

Chapter 5

Material-sensitive and thickness-resolved transmission imaging using coherent extreme ultraviolet radiation

Fengling Zhang, Xiaomeng Liu, Antonios Pelekanidis, Matthias Gouder, Kjeld Eikema, and Stefan Witte. *under review*

Microscopy with EUV radiation enables high-resolution imaging with excellent material contrast, because of the short wavelength and numerous element-specific absorption edges available in this spectral range. Table-top HHG sources offer the additional advantage of generating wide spectra in the EUV and soft X-ray range, making them inherently well-suited for characterizing nanostructures. As lens-based EUV imaging is challenging, lensless imaging methods based on coherent diffraction offer practical advantages and can even allow for quantitative phase measurements of object transmission functions. Here, a spectrally resolved lensless imaging of dispersive sample is performed using multiple high harmonics, based on different HHG-based measurement concepts. We characterize the structure and composition of a three-element spiral-shaped object in transmission using multi-wavelength diffractive shearing interferometry, as well as single-wavelength structured-illumination ptychography. We find that both methods are capable of retrieving spatially resolved element maps and corresponding layer thicknesses. Comparing methods, ptychography provides superior accuracy in determining layer thickness, even for stacks of multiple materials, using an extended scattering quotient. These measurement and analysis concepts thus provide a non-destructive way to accurately extract information on the material composition and layer thicknesses of complex nanostructured samples.

5.1 Introduction: Material-sensitive Coherent Diffractive Imaging with High Harmonic Sources

Breakthroughs in imaging are driving advances in nanoscale metrology, enabling more precise multiscale, three-dimensional characterization of functional systems such as integrated circuits in the semiconductor industry. Unlike traditional microscopy, which requires wavelength-specific lenses for photons and electrons, CDI captures diffraction patterns directly and employs numerical phase retrieval algorithms to reconstruct an object [17, 20, 27]. The resulting object image can be numerically corrected for aberrations, with resolution limited only by the wavelength of the incident radiation and spatial frequency of the diffracted waves. To overcome the wavelength limitations, CDI and especially its scanning version known as ptychography [207] has been extensively explored in the short wavelength spectral ranges such as EUV [18, 35–37, 43, 48, 57] and X-ray [56, 208, 209], as well as for electron imaging [210–212].

While CDI enables high-resolution imaging, its reconstruction quality depends on the signal-to-noise ratio of the diffraction patterns [96, 213]. Current coherent sources like synchrotron radiation and free-electron lasers fulfill the high brightness requirements, yet their accessibility limits the widespread implementation of CDI techniques [56, 61, 209]. Meanwhile, table-top HHG provides the possibility to generate a broad harmonic spectrum of spatially coherent EUV radiation with a laboratory-scale setup [66]. In recent years, HHG sources have been widely applied in nanoscale coherent imaging from interferometry [214, 215], reflectometry [43, 57], and wavefront sensing [49–51, 216] to both material [35, 44, 217] and biological science [39].

For semiconductor applications, imaging and inspection with HHG sources presents an attractive option, as many materials exhibit unique absorption and transmission properties in the EUV wavelength range [218]. This capability makes HHG-based imaging an excellent tool for characterizing nanostructures. A first demonstration at 13.5 nm imaged the nearly periodic structure on a silicon-based zone plate with subwavelength spatial resolution of 12.6 nm with a corresponding relative height map [58].Recent ptychographic studies utilize information on both absorption and phase shift in every pixel of the sample image, enabling chemically resolved imaging by calculating the so-called scattering quotient [35, 217, 219].Reflection-mode ptychography enabled non-destructive determination of layer thicknesses with chemically specific contrast for substrate-based samples [43, 44, 57]. For thin, transparent samples, having a transmission-based measurement that is sensitive to both material composition and thickness of various layers would be particularly relevant.

To characterize layer thickness and material composition in transmission, both attenuation and phase shift upon propagation are relevant measurable quantities. The concept of scattering quotient is based on the ratio of these quantities [35], but removes the sensitivity to layer thickness. Another approach can be to utilize the wavelength dependence of such material properties, by performing e.g. intensity-only measurements at multiple wavelengths. In this work, we perform different HHG-based lensless imaging experiments aimed at retrieving element-resolved images of a multi-element structured film

in transmission. Specifically, we use both diffractive shearing interferometry (DSI) [214, 215] and ptychography, and compare the ability of both methods to provide quantitative information on elemental composition and layer thicknesses. DSI is ideally suited for multi-wavelength measurements, as it is based on Fourier-transform spectroscopy to retrieve spectrally resolved diffraction information. Ptychography is developed for single-wavelength measurements, although it can be extended to multi-wavelength reconstructions as well [37, 46, 48, 57]. An important advantage of ptychography is the ability to separate the probe beam information, leading to accurate quantitative phase retrieval, and enabling imaging with structured probe beams.

By applying both methods to the same sample, and comparing the results with EDX from the SEM, we analyze their respective performance. We find that especially the quantitative amplitude and phase information provided by ptychography allow for an accurate sample characterization. By extending the concept of the scattering quotient to include multiple layers of different materials, we can determine the local thickness of two layers of distinct materials across the sample. We therefore conclude that ptychography is a useful non-destructive approach to characterize both material composition and layer thickness in complex nanostructured thin film samples.

5.2 Coherent Diffractive Imaging techniques

As image sensors only record intensity, the main challenge in CDI is to retrieve the phase information belonging to a measured diffraction intensity profile. In the far-field limit, the diffracted electric field corresponds to the Fourier transform of the exit wave, which is typically modeled as the product of the illumination field ("probe") and the complex object transmission function. To reconstruct the exit wave, the phase of the electric field at the detector plane is retrieved using iterative methods [17, 28], and subsequently numerically propagated to the object plane. The two specific implementations of CDI that we use are DSI and ptychography, which are schematically depicted in Fig. 5.1 and introduced in more detail below. To compare the main properties of both methods, Table 5.1 summarizes the advantages and current limitations of both DSI and ptychography.

5.2.1 Diffractive Shearing Interferometry

The DSI approach [214] is based on the concept of spatially resolved Fourier transform spectroscopy (FTS) [221] combined with lateral shearing interferometry [222–224]. The experimental concept is shown in Fig.5.1a). The object is illuminated by a pair of broadband noncollinear HHG sources, which are produced using phased-locked pairs of intense driving laser pulses [220, 221]. The two beams illuminate the sample target at slightly different angles. An EUV-sensitive CCD camera positioned downstream captures the resulting diffraction pattern, which corresponds to the coherent sum of the two spatially displaced (sheared) exit waves in the far field. By scanning the time delay τ between the HHG pulses, a series of far-field diffraction patterns is recorded. The time delay scan gives rise to an interference pattern analogous to Fourier-transform spectroscopy at each CCD

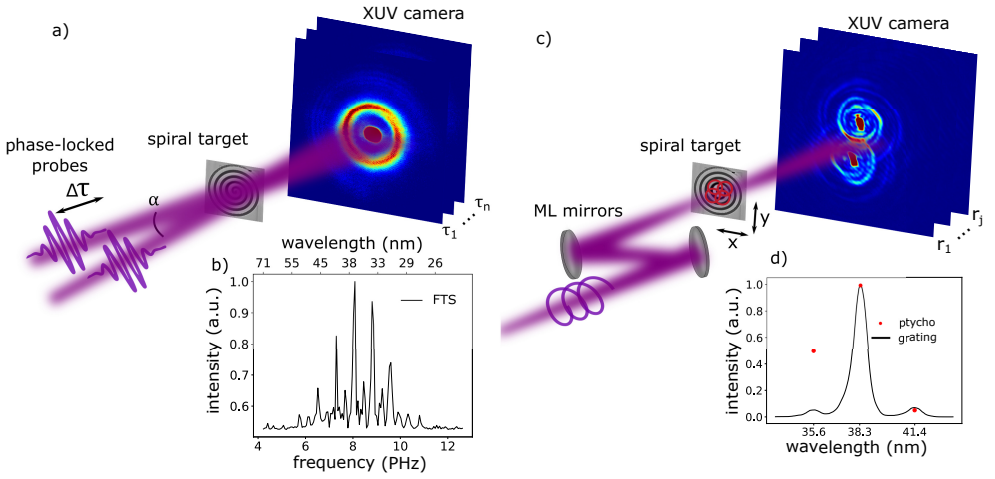

Figure 5.1: Schematic of the different CDI concepts used in this work. a) Diffractive shearing interferometry: two identical and mutually coherent HHG beams illuminate the object (being a spiral target in our experiments) with a finite shear angle α between them and a controlled time delay $\Delta\tau$. A series of diffraction patterns is recorded as a function of τ, from which spectrally resolved diffraction patterns can be reconstructed [220]. b) Typical HHG spectrum retrieved from a time-delay scan without an object present in the beam. c) Ptychography: the HHG beam is refocused and spectrally filtered by a pair of narrow-band multilayer mirrors onto the object mounted on a translation stage. A series of diffraction patterns is recorded as a function of transverse object position relative to the probe r_j. In these experiments, the EUV beam is spatially structured by imparting orbital angular momentum onto it in the HHG process. d) Measured spectrum of the EUV radiation after the spectrally selective mirrors, along with spectral weights as retrieved by ptychography (see text for details).

pixel, enabling the reconstruction of diffraction patterns for each wavelength present in the HHG illumination [220]. For each wavelength component, the complex measured interference pattern at the camera plane can then be expressed as [214]:

$$\begin{aligned} M(k) &= E(k+dk)E(k-dk)^* \\ &= A(k+dk)A(k-dk)exp\{i(\phi(k+dk)-\phi(k-dk))\} \end{aligned} \tag{5.1}$$

where $M(k)$ is the measured signal. $A(k+dk)$ is the amplitude of the electric field $E(k+dk)$ of one beam, $\phi(k)$ is the phase of the electric field and k is the k-space coordinate as recorded in the camera plane. Given the lateral shear between the two beams $2dk$, a

general camera-plane constraint for iterative phase retrieval can be written as

$$\begin{aligned} E_{n+1}(k) =&(1-\beta)E_n(k) \\ &+\frac{\beta}{2}\left[\frac{M(k-dk)E_n(k-2dk)}{|E_n(k-2dk)|^2+\epsilon^2}+\frac{M^*(k+dk)E_n(k+2dk)}{|E_n(k+2dk)|^2+\epsilon^2}\right] \end{aligned} \tag{5.2}$$

where E_n is the n^{th} guess of the electric field, β is the strength of the correction to the electric field guess and is typically set to 0.9, and ϵ is a small number to avoid zero divisions. In combination with prior knowledge of object support, the monochromatic electric field can be acquired by using different phase retrieval algorithms [27, 28, 225].

An advantage of DSI is that the complex phase term provides information about the spatial phase derivative along the direction of the shear between the beams. Furthermore, information at multiple wavelengths is recorded in parallel, making effective use of the available HHG flux and bandwidth, and avoiding the systematic errors involved in wavelength-scanning measurements. During DSI, the use of near-plane-wave illumination ensures that the diffraction pattern remains unchanged with the sample, greatly simplifying the sample alignment during reconstruction. However, the retrieved phase information still contains the wavefront of the illumination beam, making it challenging to unambiguously isolate the sample-induced phase shifts from the inherent phase curvature of the probe.

5.2.2 Ptychography

As shown in Fig. 5.1c), ptychography utilizes a spatially confined probe beam that is transversely scanned across the sample with partial overlap between adjacent positions [207]. This scanning strategy imposes strong constraints on the possible exit wave solutions, leading to robust and accurate phase retrieval. As ptychography can be extended to separately retrieve the complex fields of both probe beam and the sample response [195], the illumination profile does not need to be accurately known and can be used to increase measurement diversity [36, 37]. We perform our ptychography reconstructions with the package PtyLab.py [193], which includes the ability for ptychographic information multiplexing [46]. Here, the measured far-field diffraction pattern at position j is described as the incoherent sum of k monochromatic diffraction patterns. For our experiments on a dispersive sample, we modify the forward model to include a wavelength-dependent object transmissivity:

$$I_j \sim \sum_{\lambda}\sum_{k\in\{0,1\}}\left(\hat{\mathbf{P}}_\lambda[P_{k,\lambda}(\mathbf{r})\cdot O_\lambda(\mathbf{r}-\mathbf{r}_j)]\right)^2+I_B \tag{5.3}$$

where λ denotes the wavelength, and k refers to the orthogonal modes in the decomposition of the mutual intensity of a spatially partially coherent beam [35, 37, 126]. Both the object O and the probe P are modeled in terms of a set of modes covering the different harmonic wavelengths. Additionally, $\hat{\mathbf{P}}_\lambda$ is the scaled angular spectrum propagator [96,

226, 227], which allows the propagation of an electromagnetic wave under the Fresnel approximation, maintaining a wavelength-independent pixel size at the object plane. Although we use a narrowband multilayer mirror in the experiment, the mirror pair still reflects an additional harmonic on each side of the central harmonic, as shown in Fig. 5.1d). I_B is a constant background, caused by leakage of the fundamental beam to the detector and thermal effects from the detector itself.

Ptychographic methods remove the need for any object support and the associated prior object knowledge [207]. However, in addition to the computational complexity, ptychography relies on accurate knowledge of the wavelengths and the distance between the object and the detector plane to ensure the scaled angular spectrum propagator $\hat{\mathbf{P}}_\lambda$ can be applied accurately, although such parameters can be optimized numerically to a certain extent [200].

Table 5.1: Comparison of DSI and ptychography

Method	FTS+DSI	Ptychography
Spectral-resolved	$\surd$ no prior knowledge needed	$\surd$ Needs well-calibrated prior input
Quantitative phase retrieval	$\times$	$\surd$
Amplitude retrieval	$\surd$	$\surd$
Advantages	Single-shot imaging; high spatial and temporal resolution	Reconstructs probe and object; large field of view with nanoscale resolution; compensate partial coherence and imperfect measurements via a mixed-state model.
Limitations	Prior knowledge of sample; cannot separate phase contributions from object and probe.	Prior knowledge of spectrum; high computational cost.

5.3 Materials and Methods

5.3.1 Nanofabrication of a dispersive multilayer sample

To test the performance of the different CDI methods on a dispersive and multi-element sample in transmission, we fabricated a dedicated test object. Such a partially transparent sample was fabricated using a combination of sputter coating and focused ion beam (FIB) milling techniques. A 50 nm thick freestanding Si_3N_4 membrane was used as the substrate, coated with a 59 nm thick layer of titanium, followed by 100 nm thick gold capping layer. As shown in Fig. 5.2b), a spiral shaped pattern is milled onto the multilayer substrate using

the FIB processing. The narrow-linewidth spiral structure generates far-field diffraction patterns with strong high-angle components, providing rich spatial frequency information that benefits CDI reconstruction.

A key feature of the design is the spiral pattern's varying depth profile, which gradually changes from the center outward. At the very center, all layers are fully removed, resulting in full transmission. As the spiral line progresses towards the outside, the Si_3N_4 layer starts to appear and gradually increases in thickness to 50 nm. The EUV transmission profile for a 50 nm Si_3N_4 layer is shown in Fig. 5.2a). Further towards the outside of the spiral, the Ti layer also remains present with gradually increasing thickness. The EUV transmission for 50 nm Si_3N_4 plus 59 nm Ti is shown in Fig. 5.2c). At the tail of the spiral, the full thickness is retained. In this region, the transmission is expected to drop to zero, as the gold layer is fully opaque for our HHG spectrum. To mark where the spiral ends, a fully transmissive rectangular hole is milled as a reference marker. As the Si_3N_4 and Ti layers have different spectral responses, and especially Ti has an absorption edge leading to a strong reduction in transmissivity at wavelengths below 30 nm, the resulting object is expected to have a strong spatially-dependent spectral response in both amplitude and phase.

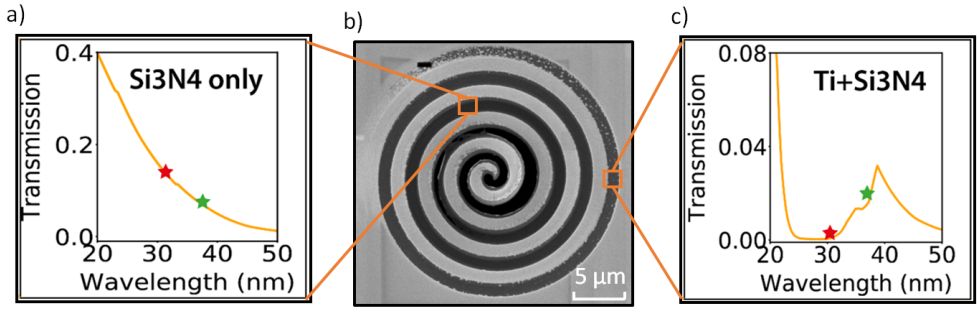

Figure 5.2: The transmission profile of the a) Si_3N_4 layer and c) Si_3N_4+Ti layer, respectively. The red star indicates the transmission at the 31 nm, while the green star indicates transmission at 37 nm. b) The SEM image of the spiral target.

5.3.2 Experiment Design

The DSI experimental setup is shown in Fig. 5.1a). The two EUV beams intersect at a relative angle α of 0.4 mrad, resulting in two sheared copies of the diffraction pattern on the CCD camera placed 18 cm downstream from the sample plane. The CCD chip has 2048x2048 pixels with 13.5 um pixel size. The sample transmissivity was low, which necessitated an 18-second integration time for each camera exposure with 4-by-4 binning and 4× camera pre-amplifier gain. The time-delay scan was optimized for the HHG spectrum in argon gas jet, with a time delay step of approximately 32 as, corresponding

to 9.7 nm optical path difference, enabling measurement of the theoretically shortest wavelength of 19.4 nm. The entire experiment comprised 485 time steps, resulting in a total delay of 15.7 fs, spanning multiple optical cycles of the driving laser and ensuring sufficient spectral resolution.

The ptychographic experimental setup is shown in Fig. 5.1c). The fundamental laser driving the HHG process contained OAM with charge one, leading to harmonics carrying OAM as well [180]. This nonzero OAM results in a significantly structured illumination profile of the probe, which improves the reconstruction quality and algorithm convergence [36, 37]. The structured high harmonics are refocused by a pair of narrow-band multilayer mirrors onto the sample. The CCD camera is placed approximately 10.68 cm from the sample plane. A typical multi-spectral HHG diffraction pattern corresponding to illumination of the central area of the sample is shown in Figs. 5.1c). The ptychographic datasets for the OAM beams consist of 301 scan positions in a concentric scan grid with 3.76 um step size and 67 um field of view. The EUV spectrum is measured separately by placing a transmission grating with 500 nm pitch (solid line in Fig. 5.1d)) in the HHG beam. Furthermore, ptychography retrieves the spectral weights of the different probe modes [49], allowing a comparison (Fig. 5.1d)). The multilayer mirror pair is specifically designed to reflect the 27th harmonic (38.3 nm), while the neighboring 25th and 29th harmonics exhibit significantly lower signal strengths, approximately 10% of that of the 27th harmonic. A discrepancy between retrieved spectrum and grating measurement is observed at the 25th harmonic at 35.6 nm, where the signal-to-noise ratio is the lowest. Therefore, we focus on the ptychographic results at 38.3 nm in the rest of this paper.

5.4 Results and Discussion

5.4.1 Qualitative, material-resolved DSI results

Figures 5.3a) and b) show the retrieved monochromatic diffraction patterns at wavelengths 31 nm (red trace) and 37 nm (green trace) resulting from the time-delay scan, respectively. The wavelength scaling between the patterns at 31 nm and 37 nm is clearly visible. The DSI iterative phase retrieval method is employed to reconstruct the spiral images at both 31 nm and 37 nm wavelengths from their corresponding diffraction patterns.

The reconstructed spiral transmissivity images at 31 nm and 37 nm are visualized using color mapping, with red representing 31 nm and green representing 37 nm. The two reconstructed spiral images are superimposed, as illustrated in Fig. 5.3c), with their transmissivities normalized at the center of the spiral where no material is present. The color in the composite image reflects the relative transmission strength at the two wavelengths. In the central region, a yellow hue indicates comparable transmission at 31 nm and 37 nm. A gradual shift in color is observed toward red in regions primarily composed of Si_3N_4, and toward green in regions containing Ti. These trends meet a good agreement with the expected transmission properties of the respective materials shown in Fig. 5.2.

The DSI data is analyzed by taking a line-out along the spiral line, to determine the experimentally observed normalized transmissivity along the spiral. As an independent

reference, we performed EDX measurements on the same sample, and calculated expected sample transmissivity from the observed local elemental composition. More details on the EDX data and analysis are given in Appendix 5.6.1 and 5.6.1. The comparison of the DSI and EDX results is shown in Fig. 5.3d). The reconstructed transmissivity from DSI (solid traces) is consistent with the EDX results (dashed traces). Figure 5.3e) shows the transmissivity across the outer ring of the spiral structure, where a larger amount of Ti remains on the sample. Significantly, the transmissivity at 37 nm is higher than that at 31 nm in both DSI and EDX datasets. This wavelength-dependent variation in transmissivity suggests the presence of both Si_3N_4 and Ti in the region between around 500 μm and 1500 μm distance along the spiral path.

DSI measurements provide an accurate spectrally-resolved imaging method. Qualitatively, good agreement is found between the transmission percentages extracted from the DSI data and from the EDX data. However, accurately extracting quantitative layer thicknesses based solely on the amplitude information from DSI is found to be challenging. Although the DSI and EDX data show consistent trends at both 31 nm and 37 nm, the level of noise in the DSI-derived transmissivity is comparable to the wavelength-dependent signal differences, limiting the precision of any layer thickness estimation. To achieve more accurate material-specific and elemental characterization, the phase of the exit wave can be taken into consideration, which allows mapping the spatial variations in optical path length across the sample. In DSI reconstruction, however, the measured phase contains contributions from both the sample and the illumination beam, and separating the phase shift introduced by the dispersive sample from the inherent phase curvature of the probe is a significant challenge. Therefore, any quantitative analysis of DSI image reconstructions typically remains limited to the intensity information. The following section explores how ptychography offers a promising approach to overcome this limitation.

5.4.2 Quantitative, material-resolved and thickness-sensitive ptychography measurements

The results of the ptychography measurement are summarized in Fig. 5.4. The reconstructed spiral target is shown in Fig. 5.4a). Given the current experimental parameters, the diffraction-limited resolution is 138 nm, assuming the shortest contributing wavelength component is 35.6 nm. Since the reconstructions give complex-valued expressions for both the object and the probe, numerical propagation was applied to the object to correct for a defocus term arising from calibration mismatches in the wavelength or the sample-to-camera distance. Figure 5.4b shows the reconstructed probe, which is 27th harmonic generated from our home-built high-power laser operating at 1030 nm central wavelength [228]. Two incoherent probe modes at 38.3 nm are reconstructed, referring to "mixed states" in Section 2.2. The main mode $k = 0$ contains 62% of the intensity, with an overall mode purity of 71.2% [126]. Given that HHG sources typically exhibit a high degree of spatial coherence [229], we attribute the mixed state modes to partial decoherence and other sources of noise in the forward model. The reconstructed probe does not exhibit the typical donut-shaped profile characteristic of standard OAM beams.

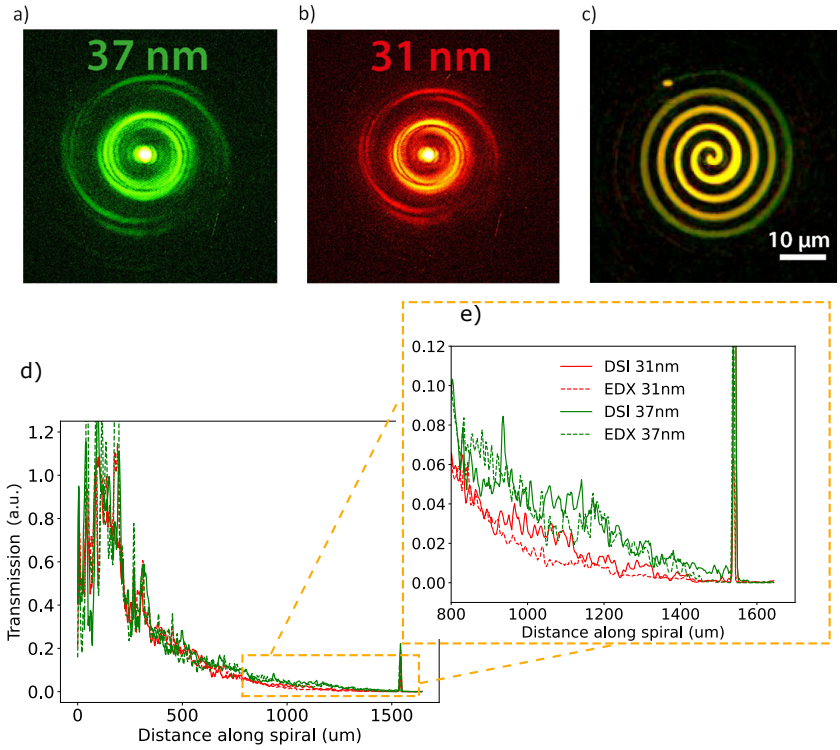

Figure 5.3: DSI measurement results. Monochromatic diffraction patterns at a wavelength of a) 37 nm and b) 31 nm. c) Image reconstructions superimposed at wavelengths of 37 nm (green) and 31 nm (red). A yellow color represents similar transmission at both wavelengths, while red or green color indicates higher transmission at 31 nm or 37 nm, respectively. d) Comparison of the relative smooth transmissivity along the spiral, as determined by DSI at 31 nm (red solid line) and 37 nm (green solid line) wavelength, and calculated from the layer thicknesses determined from EDX (see text for details) data for 31 nm (red dashed line) and 37 nm (green dashed line), respectively. e) Zoomed-in version of d) for the outer part of the spiral.

This deviation is primarily attributed to strong astigmatism introduced by the multilayer mirrors, as discussed in detail in our previous work [51].

Similar to the DSI analysis, we retrieved the transmissivity along the spiral line. As ptychography separates the complex fields of objetct and probe, it becomes possible to quantitatively assess the phase delay introduced by the object along the spiral trajectory as well (Fig. 5.4c)). From the retrieved transmission intensity, we find that the transmission curve is consistent with the results from the DSI and EDX measurements.

Knowing the phase profiles of spiral sample enables us to analyze its material properties in more detail. Similar to the intensity, there is a distinct jump in the accumulated phase

around 250 μm along the spiral, which has much better visibility in the phase profile compared to the noisier intensity profile. Further along the spiral path, the phase delay continues to increase monotonously, as expected for an increasing amount of material, but with a varying slope. This behavior indicates that the spiral sample exhibits a more complex structure than a simple material with linearly increasing thickness. Given the limited control over the rate of material removal in the FIB milling process, especially in the presence of multiple elements, a linear thickness profile would not necessarily be expected for the fabricated spiral path.

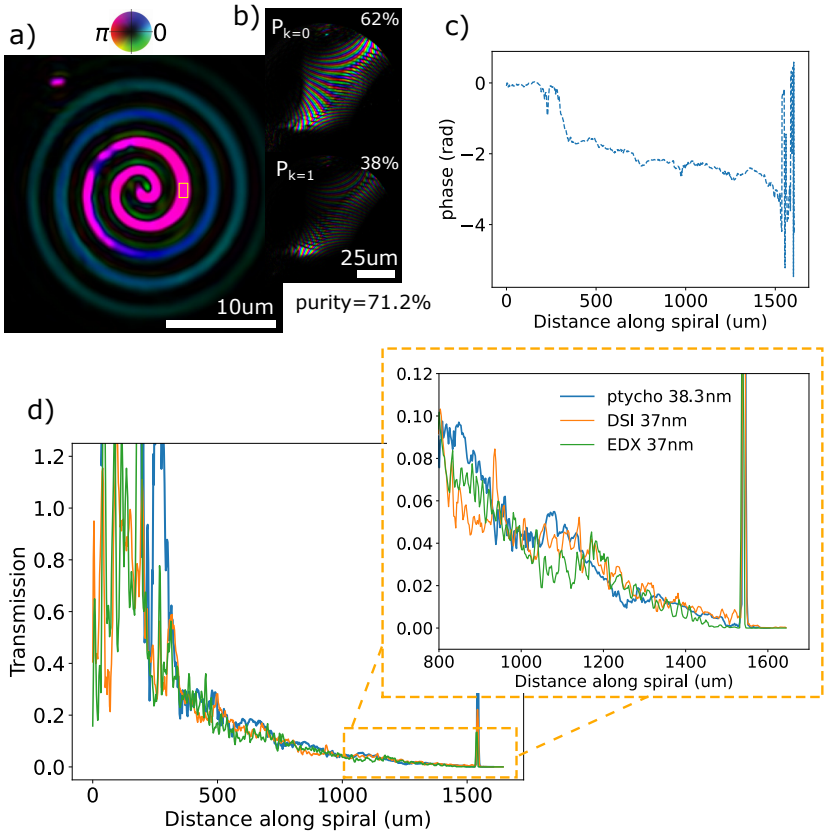

Figure 5.4: Ptychography reconstructions of a) the spiral sample and b) the main spatial modes of the OAM beam at 38.3 nm. Here, the amplitude and the phase are represented by brightness and color, respectively. c) extracted unwrapped phase along the trajectory of the spiral. d) Comparison of the relative transmissivity along the spiral, as determined by ptychography at 38.3 nm (blue trace), DSI at 37 nm (orange trace) and EDX at 37 nm (green trace).

For a more quantitative analysis of the local material composition, we use the retrieved

amplitude and phase images to calculate the scattering quotient averaged along the projection direction (Fig 5.5a)). The scattering quotient allows identification of different materials by comparison with measured complex refractive indices of different materials [35, 39]. With the complex refractive index given as $n = 1 - \delta - i\beta$, the scattering quotient is defined as the ratio $f_q = \delta/\beta$, which can be shown [35] to be equivalent to the ratio of the measured phase delay and the logarithm of the object transmissivity amplitude:

$$f_q = \frac{\phi(x,y)}{\ln(|A(x,y)|)} = \frac{\delta}{\beta} \tag{5.4}$$

An advantage of such a scattering quotient is that it is independent of the layer thickness, making it a sensitive probe to identify materials in the case of a single element at each location. In the case where multiple elements are stacked, a similar approach can still be used to connect the measured amplitude and phase to the local material properties. We define an extended scattering quotient, which for a two-layer system takes the following form:

$$f_q = \frac{\phi(x,y)}{\ln(|A(x,y)|)} = \frac{\delta_1 + \delta_2(d_2/d_1)}{\beta_1 + \beta_2(d_2/d_1)} \tag{5.5}$$

where the refractive index of the Si_3N_4 is given by $n_1 = 1 - \delta_1 - i\beta_1$, and the subscript '2' refers to Ti. A derivation of this extended scattering quotient is provided in the Appendix 5.6.3, and a further extension to more than two materials is straightforward. For locations on the sample where the the Ti layer is removed (i.e. $d_2 = 0$), f_q only corresponds to Si_3N_4. Equation 5.5 then reduces to the form for a single material (Eq. 5.4 and again becomes independent of material thickness).

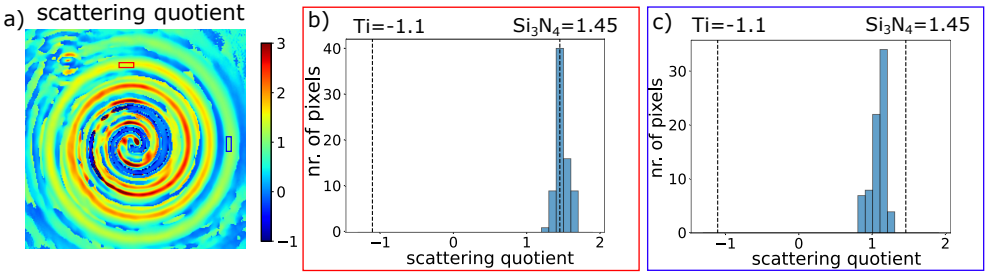

Figure 5.5: a) Scattering quotient map from reconstructed spiral sample. b) and c) Histograms representing the data from the selected regions (blue and red squares in a), respectively).

To determine the spatially resolved scattering quotient across the object, we take an area at a position where the spiral is fully open (indicated by the yellow rectangle in Fig. 5.4a)) as a reference. The object transmissivity amplitude $A(x,y)$ and phase delay $\phi(x,y)$ are then determined with respect to that reference, and used to calculate the scattering quotient. The result is shown in Fig. 5.5a). Along the spiral path, a continuous change of the scattering quotient is observed, indicating a change in the material composition. For further analysis, we plot histograms of the scattering quotient per pixel across two

selected regions located in different ringsindicated by the red and blue areas in Fig. 5.5a), respectively. In the histogram of the red region (Fig. 5.5b)), corresponding to the inner ring, the scattering quotient peaks around 1.45 at 38.3 nm. This value matches the expected value for Si_3N_4, indicating that there is a single material present in this area. In contrast, the histogram of the blue area in the outer ring (Fig. 5.5c)) shows a significantly lower scattering quotient, which can be attributed to the presence of Ti on top of the Si_3N_4 membrane. As expected from Eq. 5.5, a value for the scattering quotient is found that effectively is a weighted average of the value of the separate elements, with the relative thickness of the two layers as the weighting factor.

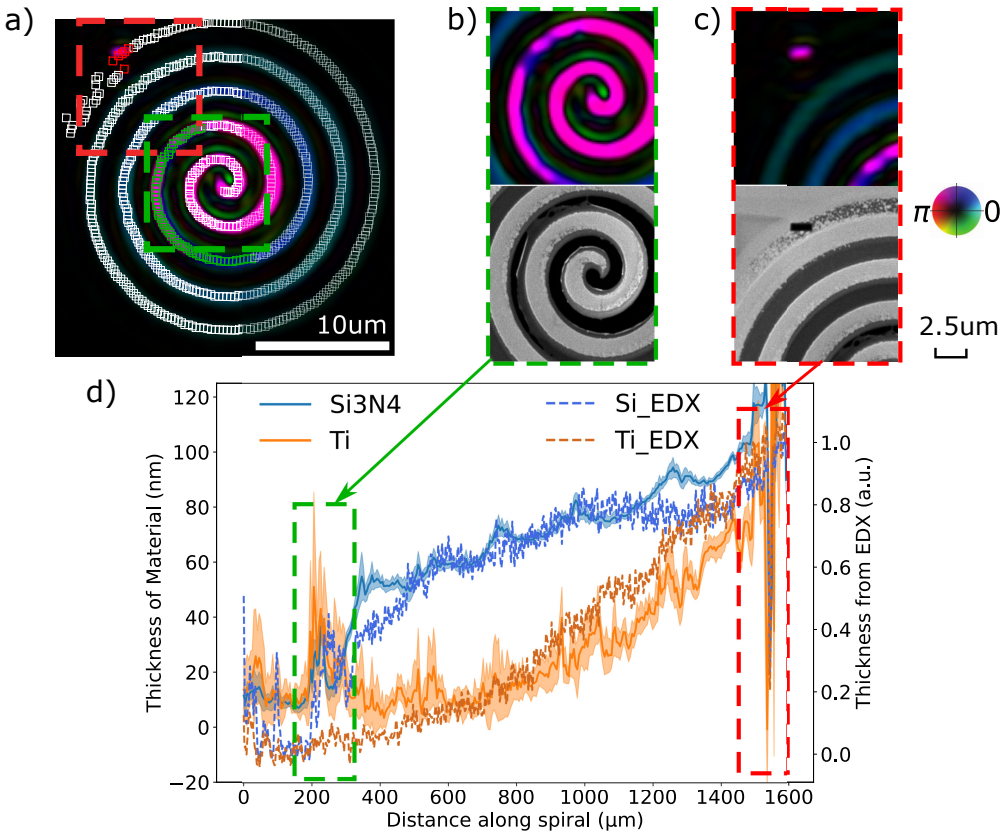

Figure 5.6: Quantitative thickness determination from ptychography reconstructions. a) White squares indicate the regions selected along the line-out of the reconstructed complex transmissivity of the spiral sample. Regions of specific interest, highlighted in green and red in a), are shown in detail in b) and c), respectively. d) Absolute layer thicknesses extracted from the ptychography, including a comparison of the normalized layer thickness along the spiral sample as determined by EDX (dashed traces).

For a sample consisting of two materials, it is possible to determine the thickness

of both layers from the reconstructed amplitude and phase delay. Assuming weakly reflecting layers and linear propagation, the thickness of the two layers can be expressed as:

$$d_1 = \frac{C_1\delta_2 - C_2\beta_2}{\beta_1\delta_2 - \beta_2\delta_1} \tag{5.6}$$

$$d_2 = \frac{C_2\beta_1 - C_1\delta_1}{\beta_1\delta_2 - \beta_2\delta_1} \tag{5.7}$$

Here, $C_1 = -(\lambda_0/2\pi)\ln(|A|)$ and $C_2 = (\lambda_0/2\pi)\ \phi$. A derivation of these expressions, along with an error analysis of the thickness determination, is given in the Appendix 5.6.4. Figure 5.6 shows the results of such a layer thickness analysis on our spiral target. We average the measured amplitude and phase over a series of 5×5 $pixels^2$ areas (954 in total), indicated by white squares in Fig. 5.6a), and calculate the thickness of the Si_3N_4 and Ti layers using Eqs. 5.6, 5.7. Starting from the spiral center to the outside, the thickness of both layers remains consistent with zero up to around 150 μm. From there onward, a rapid increase in thickness of especially the Si_3N_4 layer is observed from 170 to 300 μm, as highlighted by the green dashed box in Fig. 5.6d). This region corresponds to the green-marked areas in Fig. 5.6a). After 300 μm the Si_3N_4 thickness continues to increase at a much lower rate, while the thickness of the Ti layer starts to increase more rapidly. The nominal thicknesses of the layers are 50 nm for Si_3N_4 and 59 nm for Ti, although these values can have a significant error margin from the fabrication tolerances.

In Fig. 5.6d), we also compare the material thickness retrieved from ptychography with an estimate the EDX data. Although EDX cannot provide direct thickness values, for thin homogeneous layers the relative signal strength can be interpreted as the total amount of material in a column, and is therefore proportional to height (see Appendix 5.6.4 for details). By normalizing the thickness to the ptychography value at the end of the spiral path, the shape of the EDX curve can be used for comparison. These normalized curves show very good agreement, indicating that our ptychography-based approach can accurately characterize both material composition and layer thickness.

Aside from the overall good agreement, two regions along the spiral path show more complex behaviour. The first such region is around 200 μm, which is where the Si_3N_4 film becomes visible. In this area, a large peak appears in the Ti thickness as well, although with large error bars as well. This behaviour seems to result from the rapidly varying spatial structure of the Si_3N_4 film, as can be seen in the SEM image in Fig. 5.6b). Instead of a homogeneous layer, the film has various holes and curled remnants, which lead to deviations in the area-averaged scattering quotient. A second region with more complex behaviour is towards the end of the spiral. Here, a deviation between the EDX estimate and the ptychography reconstruction is visible, with an overestimation of the the Si_3N_4 thickness, and an underestimation for Ti. These discrepancies are likely due to the presence of gold particle remnants on the spiral path, as can be seen in Fig. 5.6c). The reference aperture at the end of the path is retrieved well, and the local layer thickness estimate is consistent with zero.

5.5 Outlook and Conclusion

In this work, we performed HHG-based lensless imaging experiments aimed at retrieving element-resolved and thickness-sensitive information from a multi-layer, compositionally complex nanostructured sample in transmission. DSI provides spectrally resolved reconstructions at 31 nm and 37 nm wavelengths. The method enables qualitative identification of regions dominated by Si_3N_4 and Ti across the sample based on their wavelength-dependent transmission properties. However, the ability of DSI to retrieve quantitative phase information was fundamentally constrained by the coupling of the object-induced phase with the curvature of the illumination beam. As a result, while it offers efficient multi-wavelength imaging, DSI is limited in its capacity for precise thickness determination. Ptychography overcomes the limitations of DSI by reconstructing both the amplitude and phase of the exit wave with a given spectrum. Using structured illumination with OAM beams, we obtain high-quality reconstructions at a wavelength of 38.3 nm, enabling detailed analysis of the material composition and layer thicknesses of the sample. The scattering quotient method further facilitated material identification, while the combined amplitude and phase data allowed for accurate thickness extraction, validated by EDX. It is worth noting that the ptychographic results not only provided absolute layer thickness measurements but also revealed fabrication imperfections in specific regions, such as incomplete ion milling and residual gold particles, further highlighting the sensitivity and diagnostic potential of the method.

Combining these methods with multi-wavelength ptychography would further increase the diagnostic capabilities, potentially giving sufficient information to extract thickness information of more than two layers (assuming refractive index information is available). Future work could combine DSI and ptychography to multiwavelength region, in which a pair of HHG pulses with varying time delay is used in a ptychography scan [230]. This scheme would combine increased wavelength diversity with multi-wavelength amplitude and phase reconstructions of a complex object.

In conclusion, we find that especially ptychography provides a nondestructive framework for quantitative lensless EUV imaging. The ability to perform high-resolution, material-sensitive, and thickness-resolved analysis of complex nanostructures is promising for applications in nanolithography, semiconductor inspection, and multilayer thin film analysis, where access to buried structures and identification of material contrast is essential.

5.6 Appendix

5.6.1 Energy-dispersive X-ray Spectroscopy Results

To establish a correlation between the reconstructed image and the chemical composition of the spiral sample, EDX measurements were carried out, and the results are presented in Fig. 5.7a), for the elements Si, Ti and Au. An EDX image encodes the abundance of the corresponding element in the brightness of the image. The Si image is representative of

the Si_3N_4 layer, and appears dark in the center of the spiral, indicating that the layer has been completely removed. Along the spiral line, the brightness increases, indicating an increase in the thickness of the layer. Similar observations were made for the other two elements, but with different gradients and positions where the material is fully removed.

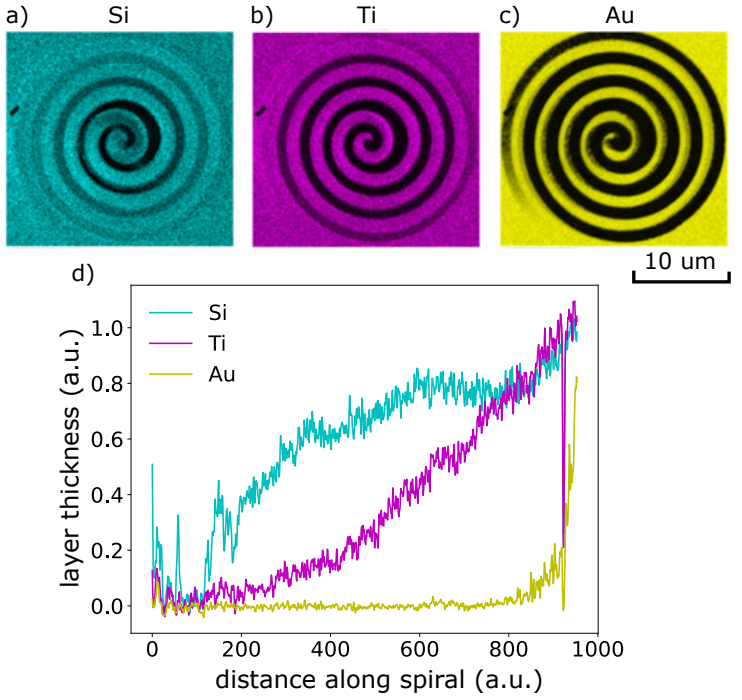

Figure 5.7: a) EDX measurements of the spiral sample: Si, Ti and Au data is shown. b) Line-out along the spiral on the EDX data, giving an indication of the local layer thicknesses.

The EDX data is analyzed by taking a line-out along the spiral line and normalizing it to the signal outside the spiral, as illustrated in Fig 5.7b). This signal is interpreted as the local layer thickness d_l for each element. From this data, the EUV spectral transmission of each material is subsequently estimated through the utilization of a comprehensive X-ray database, provided by the Center for X-Ray Optics [231]. The Beer-Lambert Law is then used to derive the transmission as a function of layer thickness, following the expression: $T_{layer} = T_t^{d_l/d_t}$, where T_t and d_t are the expected transmission and the nominal thickness of the fabricated layers. Finally, the overall transmission of the spiral thin-film is calculated by multiplying the individual layer transmissions.

5.6.2 Data analysis to raw transmissivity from DSI and EDX

Figure 5.8 shows the raw transmissivity data from DSI and EDX measurements. To improve visibility and signal-to-noise ratio, we have applied a smoothing procedure to the data, which leads to the final results shown in Fig. 5.3d-e) in the main text. For this smoothing, we convolute the raw transmissivity profiles with a rectangular window function of 3 μm width. While this does lead to a reduction of the spatial resolution along the spiral path, the noise reduction makes the resulting curves more readily comparable.

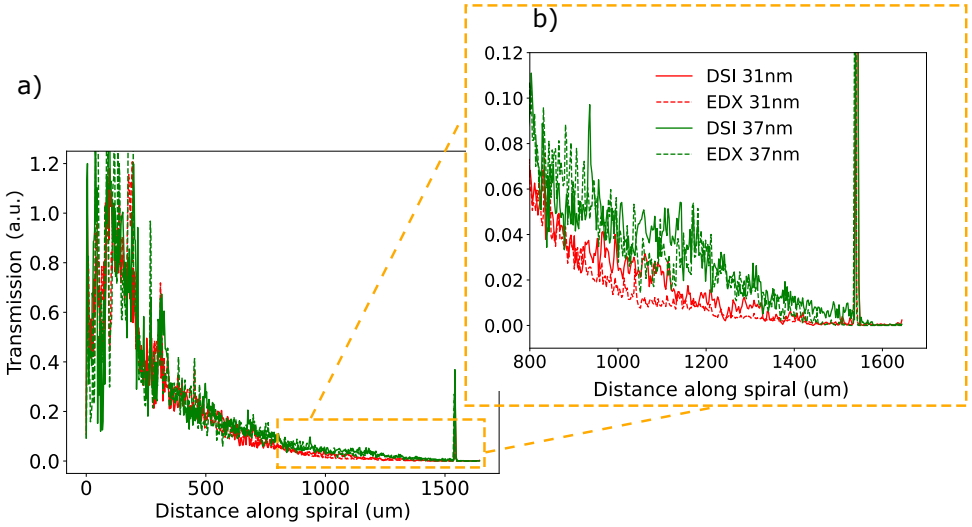

Figure 5.8: a) Comparison of the relative transmissivity along the spiral, as determined by DSI at 31 nm (red solid line) and 37 nm (green solid line) wavelength, and calculated from the layer thicknesses determined by EDX data for 31 nm (red dashed line) and 37 nm (green dashed line), respectively. b) Zoomed-in version of a) for the outer part of the spiral.

5.6.3 Expression for the extended scattering quotient

The scattering quotient can be applied to the case of multiple materials along the projection direction of the measurement. Starting from an incident field with amplitude E_0, the transmitted field behind the two-layer sample can be described by:

$$E(d_1, d_2) = E_0 \exp(-ik_1 d_1) \exp(-ik_2 d_2) \tag{5.8}$$

where d_1 and d_2 are the thicknesses of two different materials, respectively. The wavenumber $k_j = 2\pi n/\lambda$, with the refractive index of the material $n_j = 1 - \delta_j - i\beta_j$ and wavelength

λ_0. By inserting those parameters in Eq.5.8, the transmitted field can be written as:

$$E(d_1, d_2) = E_0 \exp(-\frac{2\pi}{\lambda_0}(\beta_1 d_1 + \beta_2 d_2)) \exp(-i\frac{2\pi}{\lambda_0}(\delta_1 d_1 + \delta_2 d_2)) \tag{5.9}$$

where the phase shift is taken relative to propagation in vacuum.

From Eq. 5.9 it directly follows that:

$$\ln A = \ln |E/E_0| = -\frac{2\pi}{\lambda_0}(\beta_1 d_1 + \beta_2 d_2)) \tag{5.10}$$

$$\phi = \frac{2\pi}{\lambda_0}(\delta_1 d_1 + \delta_2 d_2) \tag{5.11}$$

which can be combined and rearranged to give the expression for the extended scattering quotient in the main text, Eq. 5.5. The amplitude $|A| = |E/E_0|$ and phase of the electric field are both retrieved experimentally, allowing the calculation of the scattering quotient $f_q = \phi(x, y)/\ln(|A(x, y)|)$.

5.6.4 Thickness determination and error analysis

We rewrite Eqs. 5.10, 5.11 to separate the thickness terms:

$$\beta_1 d_1 + \beta_2 d_2 = -\frac{\lambda_0}{2\pi} \ln(|A|) = C_1 \tag{5.12}$$

$$\delta_1 d_1 + \delta_2 d_2 = \frac{\lambda_0}{2\pi}\phi = C_2 \tag{5.13}$$

From these equations, it is straightforward to isolate expressions for d_1 and d_2 in terms of the material constants, the wavelength and the measured amplitude and phase delay, given by Eqs. 5.6 and 5.7 in the main text.

An estimate of the accuracy of the thicknesses is given by an error analysis based on the uncertainties in the experimental parameters A and ϕ, which are included in C_1 and C_2. The standard deviation for thickness d_1 can be written as:

$$\sigma_{d_1} = \sqrt{(\frac{\partial d_1}{\partial C_1}\frac{\partial C_1}{\partial A}\sigma_A)^2 + (\frac{\partial d_1}{\partial C_2}\frac{\partial C_2}{\partial \phi}\sigma_\phi)^2} \tag{5.14}$$

where:

$$\begin{aligned}\frac{\partial d_1}{\partial C_1} &= \frac{\delta_2}{\beta_1\delta_2 - \beta_2\delta_1}\\ \frac{\partial d_1}{\partial C_2} &= \frac{\beta_2}{\beta_1\delta_2 - \beta_2\delta_1}\\ \frac{\partial C_1}{\partial A} &= -\frac{\lambda_0}{2\pi}\frac{1}{A}\\ \frac{\partial C_2}{\partial \phi} &= \frac{\lambda_0}{2\pi}\end{aligned} \tag{5.15}$$

and the standard deviations σ_A and σ_ϕ are determined from the distribution of experimentally retrieved values within a 5×5-pixel area as indicated by the white boxes in Fig. 5.6.

Chapter 6

Fast Spectroscopic Imaging Using Extreme Ultraviolet Interferometry

Hannah C. Strauch, Fengling Zhang, Stefan Mathias, Thorsten Hohage, Stefan Witte, and G. S. Matthijs Jansen. Optics Express **32**, 28644-28654 (2024).

Extreme ultraviolet pulses as generated by high harmonic generation (HHG) are a powerful tool for both time-resolved spectroscopy and coherent diffractive imaging. However, the integration of spectroscopy and microscopy to harness the unique broadband spectra provided by HHG is hardly explored due to the challenge to decouple spectroscopic and microscopic information. Here, we present an interferometric approach to this problem that combines Fourier transform spectroscopy (FTS) with Fourier transform holography (FTH). This is made possible by the generation of phase-locked pulses using a pair of HHG sources. Crucially, in our geometry the number of interferometric measurements required is at most equal to the number of high-harmonics in the illumination, and can be further reduced by incorporating prior knowledge about the structure of the FTH sample. Compared to conventional FTS, this approach achieves over an order of magnitude increase in acquisition speed for full spectro-microscopic data, and furthermore allows high-resolution computational imaging.

6.1 Introduction

Coherent extreme ultraviolet light produced by high-harmonic generation [232] provides a unique opportunity for the study of ultrafast dynamics in condensed matter at the nanoscale. On the one hand, the short wavelength yields a favourable Abbe resolution limit, and extreme ultraviolet (EUV) coherent diffractive imaging (CDI) nowadays enables imaging at nanometer-scale resolution [18, 233, 234]. On the other hand, the wide range of photon energies and ultrashort, attosecond (as) to femtosecond (fs) pulse durations of EUV light pulses from high-harmonic generation (HHG) provide access to a wide range of elemental absorption edges. Here, time-resolved spectroscopy yields a sensitive element-resolved probe of dynamics of the electrons, the spins and the lattice in optically excited matter [235–241]. The combination of both these approaches, namely nanometer-scale microscopic time-resolved EUV spectroscopy, is highly appealing, as it would enable the study of complex dynamics in nanoscale structures ranging from naturally-inhomogeneous quantum materials to fabricated heterostructures. However, such multi-dimensional measurements remain out of reach for HHG light sources as is, and can so far only be performed at significant experimental cost at accelerator-based EUV light sources [242, 243].

Holography plays an important role in the development of advanced EUV microscopy [30, 244–248]. For example, time-resolved EUV microscopy is commonly performed by combining Fourier-transform holography (FTH) with numerical phase retrieval [122, 243]. In FTH, the diffracted wave from the sample is interfered with a reference wave that is generated by a point-like structure (usually a pinhole in transmission geometry). The resulting fringe pattern in the far-field diffraction pattern allows for direct image reconstruction by a single Fourier transform. The single-shot nature of the FTH measurement is critical for the implementation of time-resolved studies, as it implies that only the pump-probe delay needs to be scanned during an experiment. In contrast, ptychography is a powerful imaging method that enables diffraction-limited resolution and can handle experimental challenges such as partial coherence, multi-spectral illumination and structured illumination profiles [18, 47, 249, 250]. To achieve this, ptychography relies on spatial scanning of the sample in overlapping steps such that the phase retrieval problem is sufficiently constrained. The need for overlap is significantly increased for multi-spectral illumination [18, 47, 48]. A full time- and spectrum-resolved ptychography measurement would therefore place significant requirements on the brightness and stability of the EUV light source. Thus, there is a clear need for a fast spectromicroscopy technique that reduces the data collection time for scanning in the spatial and spectral domains.

A promising alternative approach to solve this challenge is EUV Fourier transform spectroscopy (FTS) [251–254] using a pair of phase-locked HHG sources. Spatially resolved FTS enables spectral multiplexing: the full HHG spectrum can be used for imaging with no requirements or assumptions on the spectral response of the sample [220, 254, 255]. Since spectral resolution is achieved by interferometric delay scanning, however, it is not clear that the multiplexing advantage also leads to an increase in data acquisition rate.

Moreover, it is unclear how the two spatially separated HHG beams can be focused to the sample to make efficient use of the generated EUV flux.

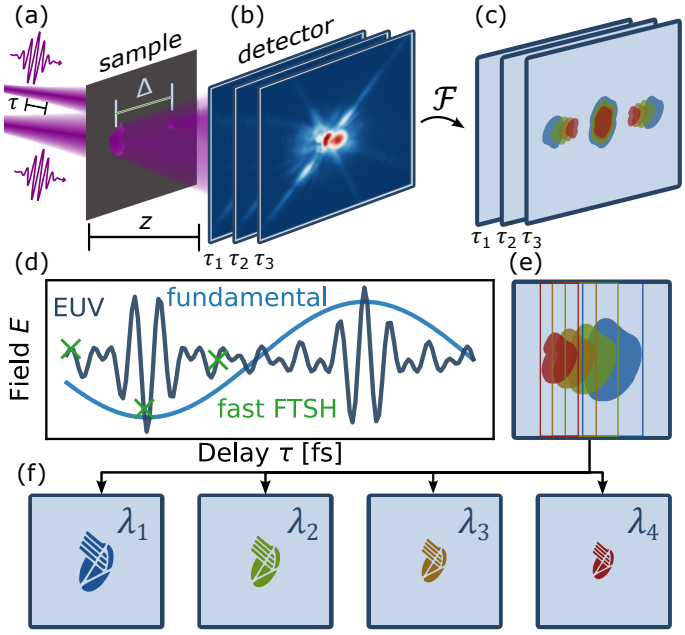

Figure 6.1: Overview of the Fourier transform spectroscopic holography (FTSH) workflow. (a) Two phase-locked polychromatic EUV beams from a pair of HHG sources illuminate the sample and reference structures. (b) The diffraction pattern is detected by a camera in the far-field. (c) As in conventional FTH, a single Fourier transform is used to analyze the interference pattern, however in this case the holograms of the individual photon energies are superimposed. (d) By time-shifting the reference wave, Fourier transform spectroscopy allows to measure the spectrum at each pixel. The necessary sampling for this measurement is significantly reduced when the multi-wavelength nature of the hologram (e) is considered, as the different spectral components are only partially overlapping. Thus, an HHG spectrum with N_λ harmonics requires at most N_λ and typically less measurements to fully recover a spectrally-resolved image (f).

In this Article, we demonstrate Fourier-transform spectroscopic holography (FTSH) (Fig. 6.1), which combines FTH with an interferometric FTS measurement. This directly improves photon efficiency, as the EUV beams can be focused to the sample and reference structures individually. More interestingly, we also find that this combination enables a direct reduction in experimental scanning: For an HHG spectrum with N_λ harmonics, FTSH requires at most N_λ measurements and this number can be further reduced by incorporating prior knowledge of the sample structure. To achieve this, we exploit the intrinsic coupling between spectral and spatial information in the FTH diffraction pattern. For our HHG spectrum (covering up to 11 harmonics from 80 to 29 nm, see Fig. 6.2b)

and sample geometry, we find that only 6 phase steps are necessary to recover all spectral components completely.

6.2 Theory

Fourier-transform spectroscopic holography (Figure 6.1) can be understood as an extension of FTH towards multiple wavelengths. For a single wavelength λ_i, the far-field diffraction pattern of an FTH sample can be expressed as $I_{\lambda_i}(k) = |\tilde{p}_i|^2 + |\tilde{r}_i|^2 + \tilde{p}_i\tilde{r}_i^* + \tilde{p}_i^*\tilde{r}_i$, where $\tilde{p}$ and $\tilde{r}$ are the electric fields at the detection plane due to the probed sample and reference, respectively, while k is the spatial frequency of the scattered wave. The fields $\tilde{p}$ and $\tilde{r}$ can be related to the fields p and r at the sample plane by optical propagation. For Fraunhofer diffraction, the propagation is given by a scaled Fourier transform, where the scale (i.e., the extent of the diffraction pattern on the camera) is proportional to the wavelength of illumination. Consequently, a Fourier transform ($\mathcal{F}$)

$$\mathcal{F}\{I_{\lambda_i}\}(x) = p_i * p_i^* + r_i * r_i^* + p_i * r_i^* + p_i^* * r_i \tag{6.1}$$

provides direct access to the holograms ($p_i * r_i^*$ and $p_i^* * r_i$) in the real-space coordinates x. It is well known that the resolution of these holograms is limited by the size of the reference r, and furthermore that the hologram appears separated from the autocorrelation terms ($p_i * p_i^*$ and $r_i * r_i^*$) at a distance Δ from the center that is equal to to the separation of p and r. In terms of pixels of the reconstructed image, the separation becomes $\Delta_{\mathrm{px}} = 2\Delta D/\lambda z$, where z is the distance and D the size of the detector. Notably, the numerical hologram separation Δ_{px} is inversely proportional to the wavelength as a consequence of the wavelength scaling of the Fraunhofer propagation operator.

While the precise position of the hologram in the frame is not important in monochromatic FTH, it becomes relevant for spectrally-resolved applications. If an FTH hologram is recorded using polychromatic radiation, a spatial Fourier transform of the data yields an image where the individual holograms are shifted according to the illuminating wavelength. This effect has been harnessed to perform single-shot spectrally resolved FTH using the individual high harmonics of a HHG light source [256]. However, this requires a specific experimental geometry: in order to fully separate the individual holograms, the sample width needs to be reduced significantly (or equivalently the Δ must be increased) by a factor that depends on the wavelength difference of neighbouring high harmonics. This drastically reduces the achievable field of view and limits the spectral resolution, altogether preventing the application to continuous (attosecond) EUV spectra. Therefore, another method is necessary to resolve the individual spectral components.

Fourier transform spectroscopy (FTS) is a powerful method that provides such a capability: analogous to FTH, interference of two pulses delayed in the time domain gives access to the spectrum by an inverse Fourier transform. FTS-based methods are already commonly used to perform hyperspectral imaging in the visible and infrared ranges (e.g., [257, 258]). In the last decade, FTS at extreme ultraviolet wavelengths has been enabled by the generation of phase-locked EUV pulse pairs by phase-locked laser pulses [253, 254].

Integrated in a CDI experiment, spatially-resolved FTS yields monochromatic diffraction patterns that can be used for numerical image reconstruction [255]. In order to satisfy the Nyquist-Shannon sampling theorem and to accurately measure the complete spectrum, however, typically a few hundred interferometric diffraction patterns at different delays must be measured.

Here, we show that the individual limitations of FTH and FTS can be lifted when they are combined in a HHG-based interferometric measurement (cf. Fig. 6.1). In particular, we propose to combine the FTSH measurement with prior knowledge of the experimental parameters. The generated wavelengths of a HHG source are generally known in advance to a good accuracy, e.g., from a prior spectroscopy measurement or from a measurement of the fundamental laser parameters. This knowledge can already significantly reduce the sampling requirements, but a further reduction is possible: Combined with knowledge of the FTH mask structure, it is possible to calculate which spectral components can contribute to each pixel in the FTH hologram. For comb-like HHG spectra spanning an octave or more, it is generally found that only a small number of harmonics contribute to each pixel in the multi-wavelength hologram.

It is instructive to consider the following example: an FTH sample containing a reference structure with negligible width and a sample with width W (along the sample-reference direction) with a sample-reference separation $\Delta = 2W$ is illuminated by a HHG spectrum containing the 9 odd harmonics 13 to 29 of a 1030 nm driving laser. In this case, the hologram of the 29$^{\text{th}}$ harmonic has significant overlap with the 27$^{\text{th}}$, successively less overlap with the 25$^{\text{th}}$, 23$^{\text{rd}}$ and 21$^{\text{st}}$ harmonic holograms, and no overlap with holograms of the 19$^{\text{th}}$ and lower high harmonics. In fact, no more than 6 high harmonics overlap at any point in the multi-wavelength hologram. This suggests that the sampling requirements in an FTS measurement can be reduced.

In FTSH, the reference beam is delayed by a time τ with respect to the probe beam. This leads to a measured intensity given by $I(k,\tau) = \sum_i^{N_\lambda} |\tilde{p}_i + \tilde{r}_i e^{-i2\pi c\tau/\lambda_i}|$. By applying a Fourier transform, we can express the measured multi-wavelength hologram $M(x',T)$ as

$$M(x',\tau) = \sum_i^{N_\lambda} p_i * p_i^* + r_i * r_i^* + (p_i * r_i^*)e^{-i2\pi c\tau/\lambda_i} + c.c., \tag{6.2}$$

where $c.c.$ indicates the complex conjugate and c is the speed of light. The coordinate x' is Fourier conjugate to the pixel coordinates of the camera, and can be related to the real-space coordinate by considering the wavelength-dependent resolution and shift Δ_{px}. It deserves emphasis that the *complex-valued* data $\sum_i^{N_\lambda}(p_i * r_i^*)e^{-i2\pi c\tau/\lambda_i}$ can be directly retrieved from the diffraction pattern measured at a single delay τ by spatially isolating the multi-wavelength hologram (see Fig. 6.1c, e).

The spectroscopic reconstruction problem can therefore be posed as follows: Given $M(x',\tau_j)$ for $j \in [1,N_\tau]$, find the complex-valued $p_i^* * r_i$ for each $i \in [1,N_\lambda]$ at each x'. For suitably chosen delays τ_j, this problem is well posed, and can be solved by matrix

inversion or least-squares methods. Ignoring prior knowledge of the shape of the holography sample there are at most $N_\lambda + 1$ unknown complex values for each x', indicating that at most $N_\tau = N_\lambda + 1$ measurements are required. This is reduced by 1 for sufficiently large Δ, since the autocorrelation terms can be filtered out spatially. A more dramatic reduction is achieved if the partial overlap of the monochromatic holograms is considered, as explained by the previous example.

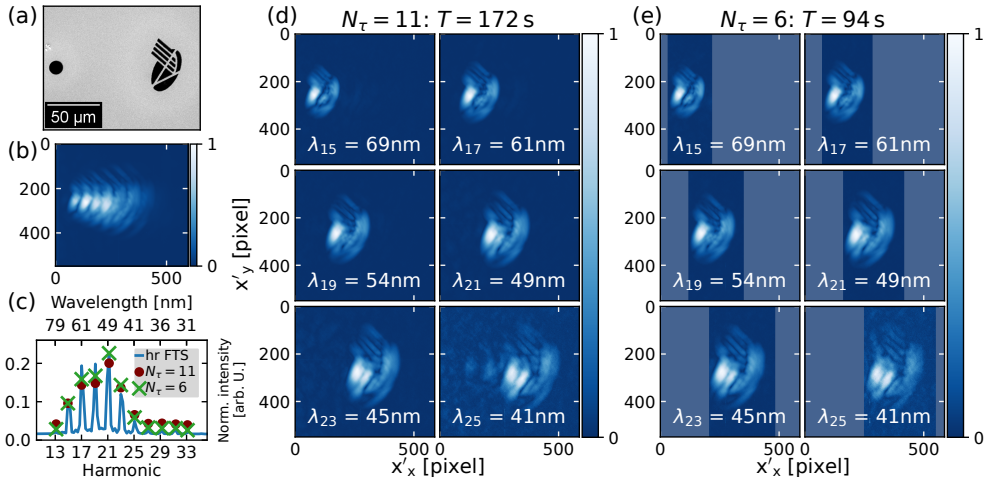

Figure 6.2: Fast Fourier-transform spectroscopic holography using minimal sampling. a) Scanning electron microscopy image of the FTH sample, which was made by focused ion beam milling of a gold-coated silicon nitride membrane. b) Exemplary amplitude $|M(x', T)|$ of the multi-wavelength hologram, showing that the different spectral components are partially overlapping. c) Extracted spectral intensity from the high resolution FTS scan, a dataset with $N_\tau = 11$ shots and $N_\tau = 6$ shots. The fundamental wavelength is 1030 nm. For comparison, the data was normalized to the total observed intensity. The small differences between the different datasets can be attributed to intensity drift and shot-to-shot variation in the HHG light source. d) Spectroscopic holography results from the $N_\tau = 11$ dataset for the 6 brightest high harmonics. e) The corresponding spectroscopic holography results from the $N_\tau = 6$ dataset. Although the resolution of these holograms is limited by the reference aperture size, they contain sufficient information to retrieve high-resolution reconstructions, as shown in Fig. 6.3.

6.3 Spectroscopic holography

In order to record FTSH data at EUV wavelengths, we employ an ultrastable birefringent common-path interferometer [253, 259] to split the output of a 1 kHz, 35 fs, 1030 nm laser (Light Conversion Pharos, compressed by cascaded nonlinear compression in 800 mbar

argon [260]) into phase-locked pulses with a controllable delay. By tilting one wedge of the common-path interferometer, these pulses are focused to two spots 200 μm apart in a Krypton gas cell, where they generate two phase-locked EUV beams. After a 200 nm Al filter to block the fundamental laser light, the high-harmonic spectrum of both pulses spans from 80 to 29 nm. At 94 cm after the HHG, we use a broadband curved multilayer mirror ($f = 25$ cm) to image the pulse pair onto the sample region. In the focus plane, the two EUV beams are separated by roughly 70 μm, and the diameter of the individual beams is roughly 25 μm. To facilitate a more homogeneous illumination of the sample, we place the FTH sample $\approx$5 mm downstream of the focus. As both the reference and sample structures are illuminated by focused EUV beams, FTSH can harness the available EUV flux more efficiently than comparable spectrally resolved CDI [255]. This advantage is further increased by the use of an extended reference (here, a disk with 12 μm diameter). The EUV camera (Andor IkonL, 13.5 micron pixel size) is placed 10 cm behind the sample.

In this geometry, we now record full FTSH data. Analysis of a high-resolution FTS scan with a time-step of 23 as over a range of 11.6 fs confirms that the HHG spectrum consists of 11 high harmonics with frequencies that match to the odd harmonics 13 to 33, with a typical upper limit on the line width of 0.5 eV. The oscillation period of these harmonics ranges from 262 as to 103 as. In the following, this dataset will serve as a reference and allows to benchmark the analysis results when only using few-delay subsets of the full data.

Next, we therefore subsample the full FTS scan in order to demonstrate the minimum sampling requirements for full spectroscopic image reconstruction. Specifically, we now consider interferometric diffraction patterns at $N_\tau = N_\lambda = 11$ equidistant delays in the range 0 - 1.7 fs (step size 190 as), which corresponds to a half cycle of the driving laser pulse. By the Nyquist theorem, the spectral resolution of the Fourier transform of this data exactly matches with the spacing of the high harmonics, namely twice the fundamental frequency. However, the sampling frequency is much lower than the highest frequency in the data, and we emphasize that the spectral amplitudes cannot be reconstructed using a Fourier transform. Instead, we solve (6.2) using the Newton conjugate-gradient method implemented in RegPy [261, 262], a Python-based toolbox for implementing and solving (potentially ill-posed) inverse problems. While the spectral reconstruction can also be achieved using other methods, this toolbox provides a number of advanced capabilities that we will exploit later.

For the case that $N_\tau = N_\lambda$, the reconstruction problem is fully constrained: for each pixel x' we have N complex-valued measurements and use these to determine N complex-valued amplitudes. This is also reflected in the measurement results: as shown in Fig. 6.2b-c, the $N_\tau = 11$ measurement allows to accurately extract the spectrally-resolved holograms from the data. This method already provides a powerful advantages over the full FTS scan: As a full FTS scan of the diffraction pattern requires to sample the highest harmonic with 2 points per oscillation and must also resolve the individual harmonics, the number of samples must be at least twice the order of the highest harmonic (i.e., 66 measurements for our spectrum with harmonics up to the 33$^{\text{rd}}$ order), the total number of measurements is dramatically reduced. In practice, the sampling advantage is around

an order of magnitude, as full FTS measurements in the EUV typically use hundreds of delays. In addition to a shorter measurement time, this implies that the short scan is much less sensitive to experimental drift, such as in the EUV beam pointing.

Next, we exploit the intrinsic wavelength-sensitivity of FTH, which leads to the relative displacement of the individual spectral components that was discussed earlier. Based on the known width (30 μm) and separation (100 μm) of the sample and reference, we construct a simple mask to constrain which spectral components can contribute to each pixel x'. From this analysis, we find that at no point more than 6 high harmonics contribute to the signal (and 99% of the pixels include contributions of ≤ 5 harmonics only). We therefore set $N_\tau = 6$ and use interference patterns spaced in delay by $1.7/5 = 0.34$ fs to again cover one half cycle of the driving laser pulse. The mask can be implemented conveniently into the RegPy reconstruction method. As shown in Fig. 6.2e, this approach enables spectroscopic imaging at a total measurement time of only 94 s. These results demonstrate that the temporal sampling requirements can be reduced by more than an order of magnitude compared to naive application of the Nyquist-Shannon limit, requiring in this case only 6 measurements instead of 66.

6.4 High-resolution spectromicroscopy

A limitation of FTH is the trade-off between resolution (requiring small reference structures) and signal strength (requiring large references). This is clearly seen in Fig. 6.2, where the spatial resolution is strongly limited by the 12 μm reference aperture. Hence, many FTH experiments use subsequent iterative phase retrieval to improve the spatial resolution and SNR [30, 247, 263]. In the following, we will demonstrate how iterative image reconstruction methods can be used to achieve a resolution in FTSH that is only limited by the numerical aperture of the scattered light. In a first step, it is useful to separate the delay-dependent and delay-independent contributions to the diffraction pattern. The delay-independent part has two contributions: $\sum_i^{N_\lambda} |\tilde{p}_i|^2$ and $\sum_i^{N_\lambda} |\tilde{r}_i|^2$. These terms each represent a conventional broadband diffraction pattern, for which it is known that image reconstruction is possible with strong prior knowledge of the spectral response of the object [172]. Reconstruction of the individual spectral components, however, is not generally possible. Also, the incoherent sum of both broadband diffraction patterns will complicate image reconstruction. Consequentially, we will focus in the following on the spectrally-resolved interference patterns that are retrieved from the FTSH analysis.

After applying a Fourier transform to the output of the FTSH analysis (such as shown in Fig. 6.2d, e), the monochromatic interference-diffraction patterns can be expressed as $m_\lambda(k) = \tilde{p}_\lambda \tilde{r}_\lambda^*(k)$. As this data already includes the phase, it is not necessary to implement phase retrieval algorithms as in monochromatic CDI. Instead, the image reconstruction of p_λ from m_λ can be posed as a deconvolution problem, where the point-spread function of the reference (r_λ) needs to be subtracted from the data. This can also be observed in the extracted monochromatic far-field interference pattern (Fig. 6.3a), where a clear imprint of the Airy pattern due to the 12 micron reference can be seen. We emphasize that the

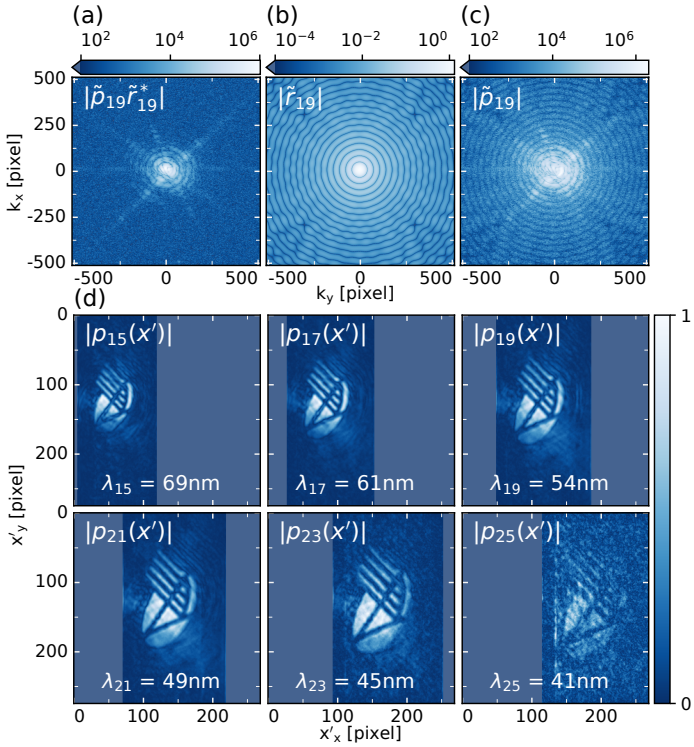

Figure 6.3: Diffraction-limited spectroscopic imaging based upon the $N_\tau = 6$ dataset with a total measurement time of 1m 34s. (a) Far-field interference pattern $|\tilde{p}_\lambda \tilde{r}^*_\lambda|$ of the 19$^{\text{th}}$ harmonic at 54 nm. (b) The far-field diffraction pattern (Airy pattern) of the reference structure at 54 nm. (c) Reconstructed far-field diffraction pattern $|\tilde{p}_\lambda|$ of the object, as extracted from (a). (d) Reconstructed images for the 15$^{\text{th}}$ to 25$^{\text{th}}$ harmonics, respectively.

clear visibility of the Airy rings is due to the direct illumination of both the reference and the sample using focused EUV beams. The shape of the observed Airy pattern matches well to the expected pattern (Fig. 6.3b) and allows us to verify the scaling of the reference aperture and the far-field propagation.

To reconstruct the diffraction-limited image from the monochromatic interferogram $m_\lambda(k)$ and the known reference r_λ, we use the Newton conjugate-gradient method to iteratively minimize $||\tilde{p}_\lambda \tilde{r}^*_\lambda(k) - m_\lambda(k)||$. In order to prevent overfitting to the noise, we use Morozov's discrepancy principle, i.e. we terminate the algorithm as soon as the residuals are on the order of the noise floor. This is commonly achieved after 11 to 15 Newton steps. Using this procedure, we find accurate image reconstructions for up to 6 high-harmonics, see Fig. 6.3, where the sample structure can now clearly be recognized. We also observe an intensity gradient and wavefront curvature that matches to the expected diverging EUV beam profile. Compared to the initial holograms that were limited by the 12 micron

diameter reference, this reconstruction procedure enables a dramatic increase in the resolution to a final resolution of approximately 1.5 micron, as determined by a line scan. This resolution corresponds to the numerical aperture of the observed reference diffraction. In following experiments, the implementation of smaller or structured references, placed directly in the focus of one of the EUV beams, can enhance the intensity of the scattered light at higher numerical aperture, and thereby optimize the resolution of the ultimately recovered images. The current experimental setup supports an Abbe-limited resolution of 150 nm for the 25^{th} harmonic at 41 nm. Also, the resolution and SNR can be improved by averaging of several consecutive measurements (see supplementary information). Finally, it is worth noting that this image reconstruction procedure does not depend on knowledge of the object support.

6.5 Discussion

Our results indicate that the sampling requirements in spatially-resolved Fourier transform spectroscopy, specifically when applied in combination with Fourier transform holography, is not determined by the well-known Nyquist-Shannon theorem applied to the HHG source spectrum, but it is rather determined by the total number of unknowns, which is in turn dependent on the FTH sample structure, the spectral resolution, and the bandwidth of the EUV spectrum. For typical HHG spectra spanning an octave or more and typical FTH sample structures, this leads to a significant reduction of the sampling requirements. In practice, the number of delay steps needed can be controlled by the sample-reference separation Δ. Increasing Δ at fixed sample width leads to a reduced overlap of the individual spectral components and consequentially a reduced number of steps. However, the increased Δ also implies that a larger total field of view must be considered in FTH. For diffraction-limited imaging at high numerical aperture, this can result in a reduction of the final image resolution. Thus, in general a trade-off between image acquisition speed, image quality and experimental parameters such as the illumination beamline must be found. An interactive notebook illustrating the connection between the separation Δ and the EUV spectral bandwidth can be found in Ref. [265].

To quantify the benefit of minimal sampling FTSH compared to high-resolution FTS, we carry out an analysis of the effective signal-to-noise (SNR) ratio of the reconstructed images in Fig. 6.8. Specifically, we compare the spectroscopic images retrieved from the $N_\tau = 6$ and $N_\tau = 11$ data sets to those from a full FTS measurement with $N_\tau = 75$. Strikingly, we observe that both the $N_\tau = 6$ and $N_\tau = 11$ show highly similar SNR to the $N_\tau = 75$ data. As exemplified in Fig. 6.8c-e, we also find no significant differences in the retrieved image resolution. Assuming that the SNR scales with $\sqrt{T}$, where T is the total measurement time, as for shot-noise-limited data, our results indicate an improvement in the SNR for $N_\tau = 6$ of almost an order of magnitude over $N_\tau = 75$ (see Fig. 6.8b). We tentatively attribute this difference to a reduced sensitivity to drifts in the EUV spectrum and beam pointing for the shorter FTSH measurement. This conclusion is also supported by an analysis of the SNR of the spectrally resolved low-resolution holograms (based on

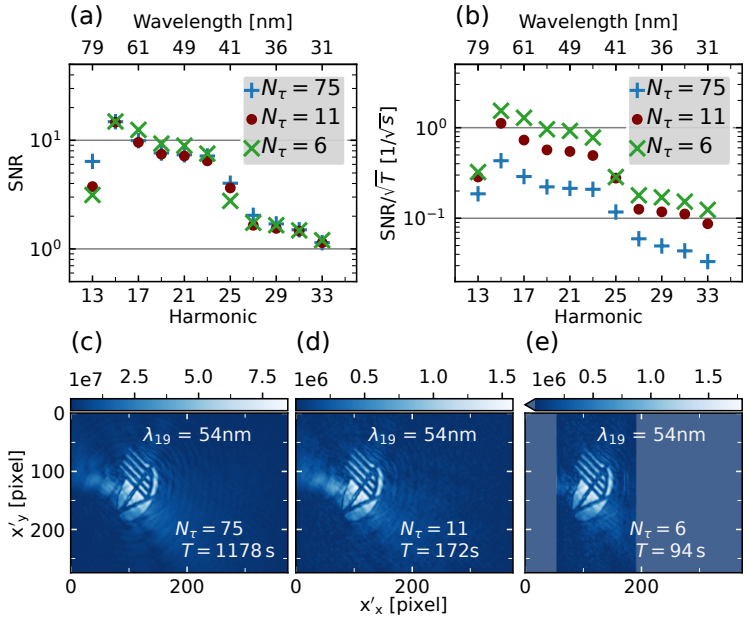

Figure 6.4: Comparison of image quality for minimally sampled FTSH compared to FTS with $N_\tau = 75$ covering a delay range of 3.48 fs. This is the minimum delay range that allows to separate the individual high harmonics by a Fourier transform. (a) The experimental signal-to-noise ratio (SNR), calculated by comparing the average logo intensity to the background, shows that all three methods yield highly similar SNR despite the large difference in total exposure time. (b) Under the assumption that the SNR is dominated by shot noise, scaling the SNR by $1/\sqrt{T}$, where T is the total measurement time, enables to predict the SNR at a longer (or shorter) total exposure time. In this manner, we find that the minimally sampled FTSH method with $N_\tau = 6$ yields almost an order of magnitude better data than classical FTS. (c-e) Exemplary spectrally-resolved holograms for the 19$^{\text{th}}$ harmonic at 54 nm for the $N_\tau = 75$, $N_\tau = 11$, and $N_\tau = 6$ data sets, respectively. Analysis of the spectrally resolved images by line scans and decorrelation analysis [264] confirm that the spatial resolution is comparable for each of the data sets.

Fig. 6.2d-e, see Supplementary Figure S4 for the SNR comparison), showing that the FTS scan yielded only marginally better holograms than minimally sampled FTSH. Thus, by enabling full spectral information within a shorter measurement time, high-quality FTSH data can be recorded straightforwardly by averaging many consecutive measurements (see Supplementary Information for an example).

The presented FTSH method relies on prior knowledge of the high-harmonic frequencies. Although these can be commonly estimated from the spectrum of the near-infrared driving pulse, the high-harmonic spectrum can be shifted due to various effects such as pulse chirp and intensity blue-shift [266, 267]. Therefore, we have performed an analysis

of frequency miss-estimation on the reconstructed electric fields, from which we find that a ±1% error in the fundamental frequency typically leads to an error of 10% (see Supplementary Information, section 3). Such errors can be completely avoided, however, by performing an extended measurement with at least one extra delay. The number of independent pixels is normally much larger than the number of spectral components (10^5 pixels and 11 frequency components in our work), and thus this extra image provides enough data to determine the high-harmonic frequencies precisely through iterative minimization. With regard to the measurement calibration, also sub-wavelength accuracy is required in the determination of the delays. This can for example be achieved using a stable interferometer [259] or through separate interferometric delay calibration [268]. An advantage of the minimally-sampled FTSH scheme for typical HHG spectra is that the necessary delay range covers less than one micrometer, thereby reducing the requirements on the interferometer.

Finally, we will shortly discuss the potential of FTSH for attosecond time-resolved studies. A crucial aspect here is the (quasi-)continuous EUV spectrum of attosecond EUV spectra. In the FTH multi-wavelength hologram, this leads to the superposition of a continuum of holograms [248], rather than a discrete set of wavelength components. Similarly, for HHG using few-cycle laser pulses, the broad line width of individual high harmonics can reduce the achievable resolution in diffractive imaging [172]. In either case, the delay sampling points can be adapted, extending the total time range to increase the spectral resolution as necessary. Crucially, assuming that the autocorrelation and hologram terms can be separated spatially, the number of delays N_τ is at most equal to the number of spectral components, and this can usually be reduced by considering the sample geometry and spectral bandwidth.

In summary, we have investigated the potential of Fourier-transform spectroscopic holography (FTSH), an interferometric technique that allows minute-scale spectromicroscopy at extreme ultraviolet photon energies. In the FTH geometry, prior knowledge of the illumination wavelengths allows a dramatic reduction in the sampling requirements. We have identified two sampling strategies for minimally sampled FTSH: (i) without assuming prior knowledge on the overlap of monochromatic holograms, the number of measurements can be reduced to the number of wavelength components in the illumination, and (ii) by incorporating such prior knowledge, a further reduction can be achieved. For our HHG spectrum and FTH sample, this reduces the number of measurements to 6, which is a typical value. Overall, this approach enables an order of magnitude reduction in the required sampling compared to full FTS sampling by the Nyquist-Shannon theorem, thereby speeding up the measurement dramatically. In the spectrally resolved holograms, we find that a higher SNR is achieved in equivalent time. This is made possible by the shorter measurement duration that reduces the effect of long-term drift and instability in the experimental setup. Finally, although the measurement is based on holography and intrinsically measures the convolution between sample and reference, FTSH does enable high spatial resolution through iterative image reconstruction. We expect that this method will contribute strongly to the implementation of table-top extreme ultraviolet spectromicroscopy, for example in time-resolved experiments where a fast measurement

is necessary to facilitate systematic studies.

6.6 Appendix

Here, we present additional figures with the Fourier transform spectroscopic holography results. Fig. 6.5 shows averaged spectrally separated reconstructions of the hologram for all wavelengths in the HHG spectrum. The corresponding averaged interferograms are given in Fig. 6.6 and the diffraction-limited image reconstructions are given in Fig. 6.7. Figs. 6.8, 6.9 and 6.10 discuss the signal-to-noise ratio of the low-resolution holograms that can be obtained from the FTSH experiment without relying on the iterative image reconstruction. Fig. 6.12 shows typical reconstructions that have been obtained using wrongly estimated frequencies, and thus discusses the sensitivity of the analysis to a correct estimation of the high harmonic center frequencies. Finally, Fig. 6.13 shows a FTSH simulation of a spectroscopically diverse object, highlighting the applicability of FTSH for spectroscopic applications.

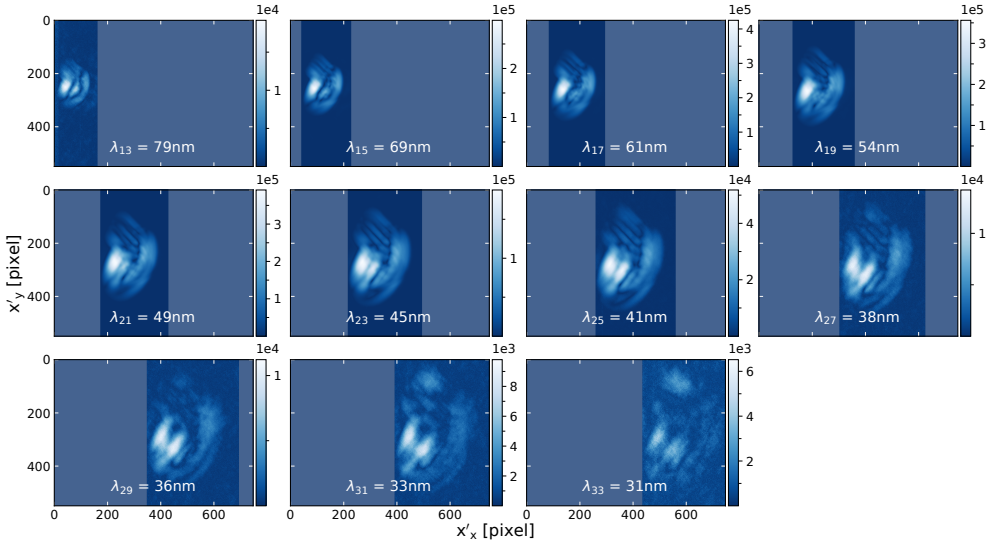

Figure 6.5: Spectroscopic holography result with a total measurement time of 2356 s. Here, 88 masked, $N_\tau = 6$ FTSH reconstructions from diffraction patterns at a total of 150 measured delays are averaged. For each $N_\tau = 6$ FTSH reconstruction 2 Newton steps are used.

6.6.1 FTSH results of averaged interferograms

The capability of Fourier-transform spectroscopic holography (FTSH) to achieve fully spectrally resolved image data from as little at 6 delay measurements does not only strongly reduce the total scan time for spatially resolved Fourier transform spectroscopy (FTS), but

it also provides another advantage: due to their shorter duration, FTSH measurements can more easily be repeated to achieve (pump-probe) time resolution or simply to improve the ultimate image quality. In Figs. 6.5, 6.6 and 6.7, we show the result of such an averaging procedure.

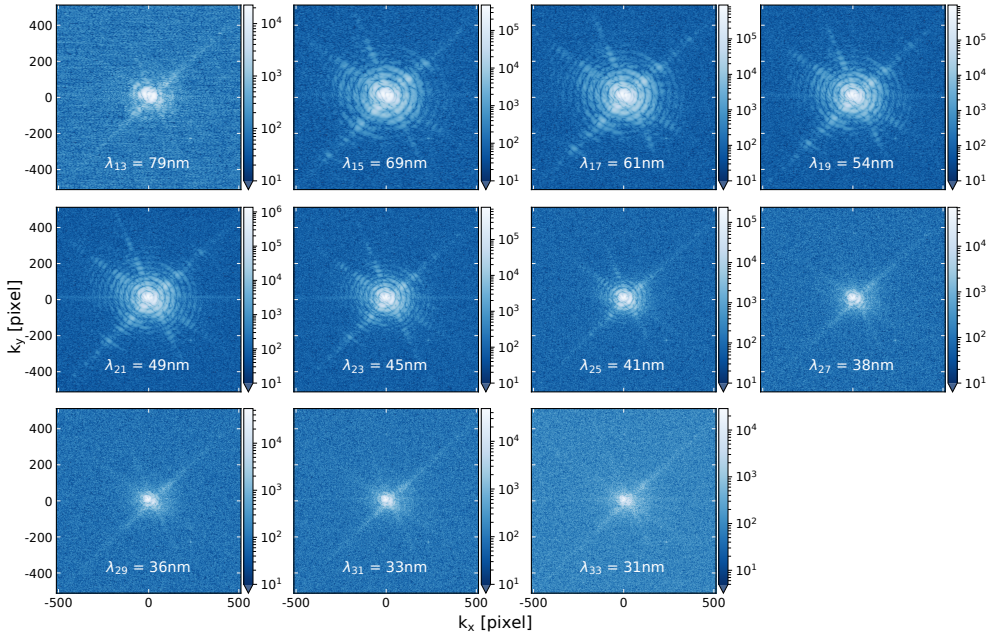

Figure 6.6: Amplitude of the the retrieved monochromatic interferograms $|m_\lambda(k)| = |\tilde{p}_\lambda \tilde{r}_\lambda^*|$ in the far field, i.e. the spatial Fourier transform of the data shown in Fig. 6.5. The k axes are given in camera pixels. To avoid potential artifacts due to the mask edge, a few-pixel cosine-tapered window function was applied before Fourier transformation.

The gain from averaging, here over 88 independent reconstructions with a total measurement time of 2356 seconds, shows up most clearly for the higher harmonics, where in the shorter, 94 seconds exposure no clear image could be resolved. In Fig. 6.5, the logo now becomes partially visible even for the highest harmonics which carry 100x less flux than the brightest harmonics. Furthermore, the still-low signal strength of these holograms does not prevent partial image reconstruction in Fig. 6.7.

6.6.2 SNR comparison for the low-resolution holograms

In Fig. 4 of the main article, the signal-to-noise ratio of the high-resolution reconstructed images for the $N_\tau = 6$ and $N_\tau = 11$ minimally sampled FTSH is compared to the result from a full FTS measurement. As the image quality as retrieved from the iterative reconstruction depends non-linearly on the signal-to-noise ratio of the low-resolution

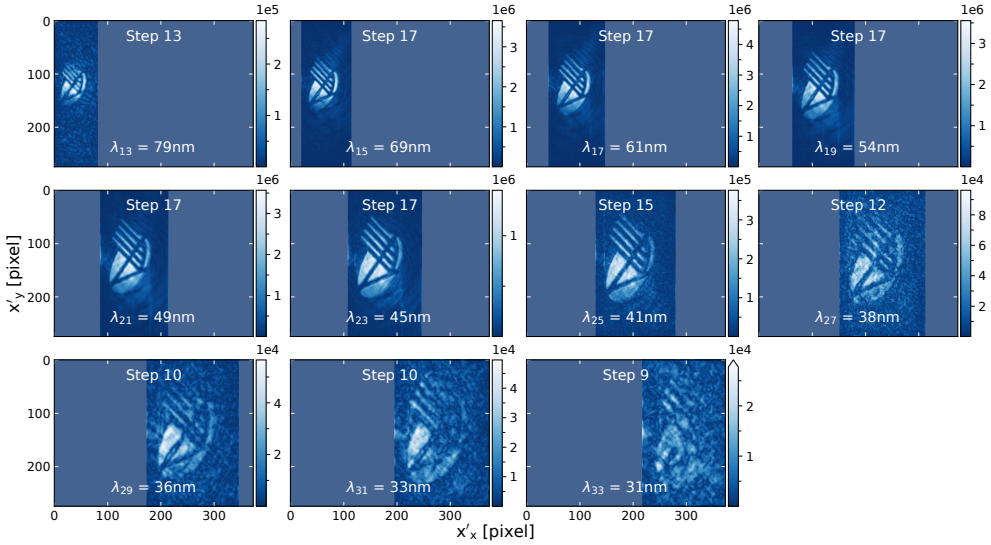

Figure 6.7: High-resolution reconstructions for all 11 high harmonics in the illumination, based on the data shown in Fig. 6.6. The number of used Newton steps iterations is indicated in each plot.

holograms, we present in Fig. 6.8 a comparison of the SNR based upon the low-resolution holograms that do not depend on this iterative procedure.

This analysis shows that, although the overall best SNR is achieved from the full FTS scan, the SNR is only ≈2x better than that of the $N_\tau = 11$ analysis, while the total exposure time was 7x longer. Assuming that the SNR of the minimally sampled reconstructions is limited by photon shot noise, minimally sampled FTSH is expected to yield a 2x higher SNR than the full FTS measurement for equal data acquisition time.

Comparing Fig. 4 and Fig. 6.8, we therefore find that the small increase in SNR for the $N_\tau = 75$ FTS scan does not translate to an improved image quality in the reconstructed images. This counter-intuitive observation nevertheless has a comparatively simple explanation: over the full duration of the 75-shot measurement, HHG source instability is non-negligible, leading to small contributions stemming from adjacent high harmonics in the monochromatized hologram. This can be observed for example in Fig. 6.8c just left of the main signal. These noise signals can not be explained by the forward model $\tilde{p}_\lambda \tilde{r}^*_\lambda(k)$, and therefore lead to a deterioration of the reconstructed image. Having much shorter measurement duration, both the $N_\tau = 6$ and $N_\tau = 11$ measurements do not suffer from this effect.

In Figs. 6.9 and 6.10, we furthermore present a similar analysis for the averaged data as shown in Fig. 6.5.

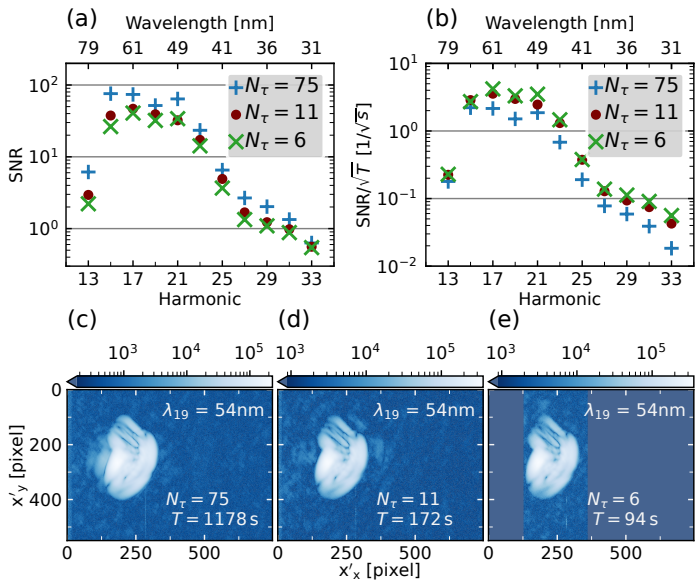

Figure 6.8: Comparison of the signal-to-noise ratio (SNR) of the low-resolution holograms for minimally sampled FTSH (see Fig. 2d-e) compared to FTS with $N_\tau = 75$ covering a delay range of 3.48 fs. This is the minimum delay range that allows to separate the individual high harmonics by a Fourier transform. (a) Experimental signal-to-noise ratio (SNR), calculated by comparing the average logo intensity to the background. (b) SNR scaled by $1/\sqrt{T}$, where T is the total measurement time. (c-e) Exemplary spectrally-resolved hologram for the 19$^{\text{th}}$ harmonic at 54 nm.

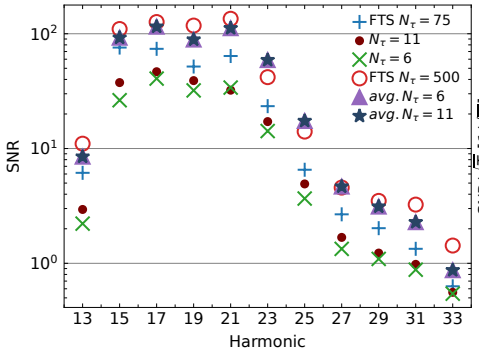

Figure 6.9: Comparison of the SNR of the low-resolution holograms obtained from various spectral analysis methods, comparable to Fig. 3a. In addition to the datasets presented in Fig. 6.8a, we also include the direct Fourier transform result of the full $N_\tau = 500$ dataset, which was recorded over a total time of 7838 s. Also shown are two results where we have averaged many minimally-sampled FTSH reconstructions (triangles and stars) extracted from a total of 150 delays, leading to a total measurement time of 2356 s. The averaged $N_\tau = 6$ data is shown in Fig. 6.5. Strikingly, the FTSH analysis based on 2356 s measurement time provides similar SNR to the 3-fold longer full FTS dataset.

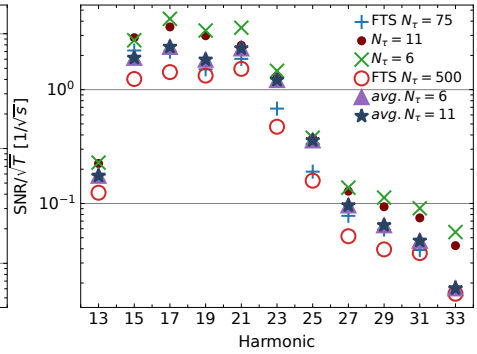

Figure 6.10: Comparison of the effective signal-to-noise ratio for various spectral analysis methods assuming shot-noise-limited data, comparable to Fig. 6.8b. Apart from the $1/\sqrt{T}$ scaling, with T being the total measurement time, the data and methods are identical to those presented in Fig. 6.9. It can be seen that the averaged images have slightly lower effective SNR than their non-averaged counterparts (i.e., the effective SNR for $N_\tau = 6$ is slightly higher than when measurement is repeated many times and subsequently averaged). This difference shows that the noise in these reconstructions is not fully shot-noise limited.

6.6.3 Effect of the frequency calibration

Maximal reduction of the sampling requirements in FTSH relies on accurate knowledge of the high harmonic frequencies. However, such information is not available in many cases. In Figs. 6.11 and 6.12, we consider a typical case: miss-estimation of the high harmonic frequencies by inaccurate determination of the fundamental frequency. Fig. 6.11 shows that in this case, the error scales approximately linear with the error in frequency, with an overall error of approximately 10% for a 1% calibration error. This is averaged over the full spectrum, and so comparatively weak high harmonics will be more strongly affected. This is also shown in Fig. 6.12: As seen clearly for the 15$^{\text{th}}$ and 25$^{\text{th}}$ harmonics at 1010 nm fundamental wavelength, the incorrect frequencies lead to an incomplete spectral separation, as signal from neighboring high harmonics remains visible in the

extracted hologram. Overall, we observe comparatively little effect on the intensity profile recovered for the bright 21st harmonic, while the relatively weaker harmonics 15 and 25 show a more dramatic effect. We therefore conclude that a miss-estimation of the high harmonic frequencies predominantly will affect the image observed for the weaker high harmonics.

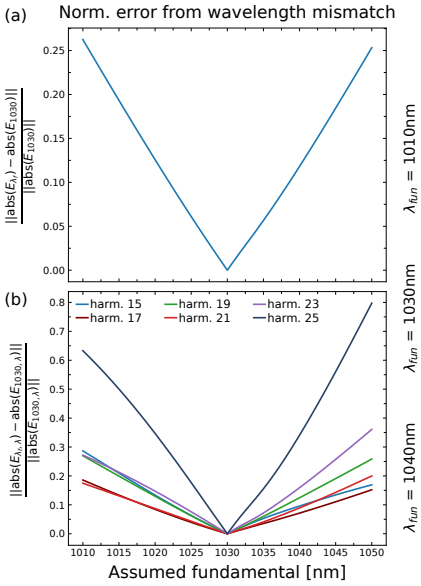

Figure 6.11: (a) Normalized difference between FTH reconstructions assuming various fundamental wavelengths and the FTH reconstruction assuming a fundamental wavelength 1030 nm of $N_\tau = 11$ as a function of assumed fundamental wavelength. (b) Normalized difference per harmonic of the harmonics 15-25. Exemplary depictions of the flawed reconstructions are given in Fig. 6.12.

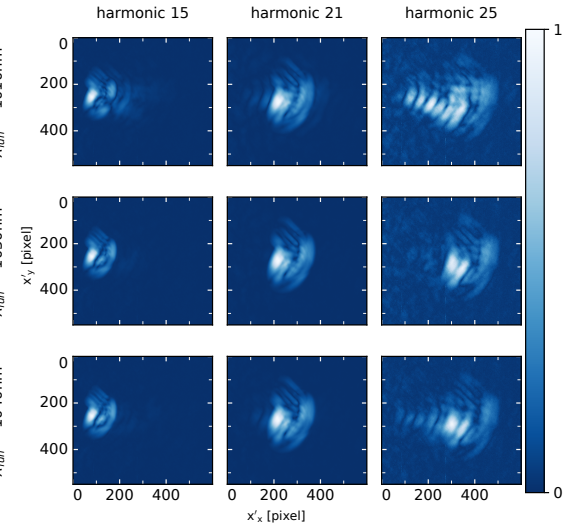

Figure 6.12: Exemplary spectrally resolved holograms calculated by assuming different fundamental wavelengths. Here, 1010 nm (top row) is significantly shorter than the expected true fundamental wavelength of 1030 nm (middle row). The bottom row shows 1040 nm, which is approximately 1% longer than expected. From left to right, the 15th, 21st and 25th harmonics are shown.

6.6.4 FTSH simulation using wavelength dependent input

To demonstrate the applicability to spectroscopic studies, we provide a few shot FTSH simulation using the same spectroscopic forward model and high resolution reconstruction code as used for the data analysis. A script producing similar output can be found as a LiveDoc jupyter notebook in Ref. [265].

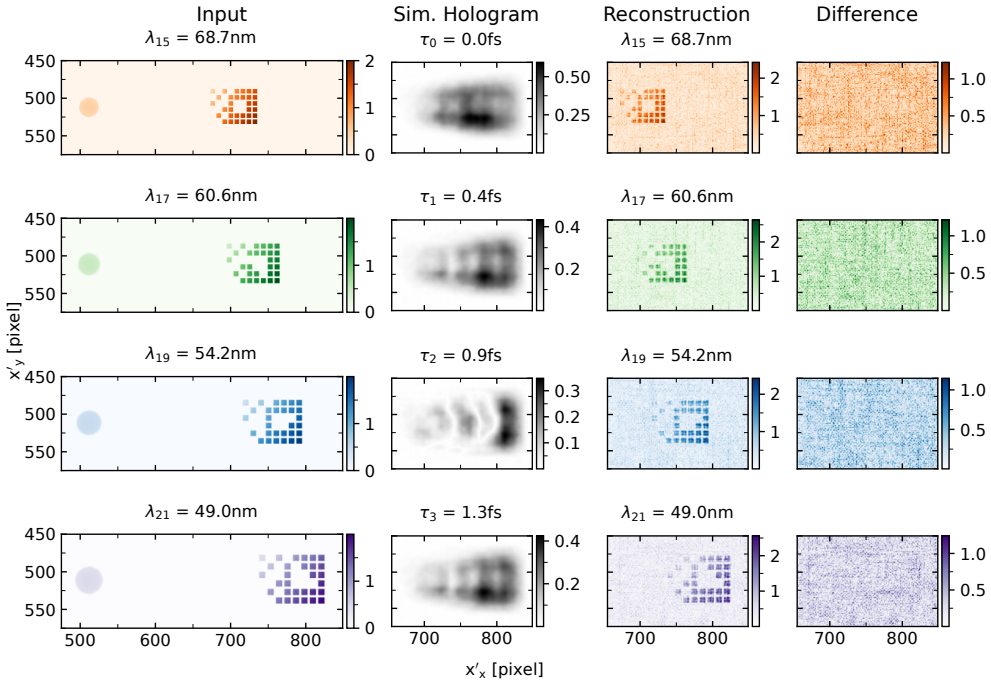

Figure 6.13: Simulation of FTSH using wavelength-dependent input. From left to right: A spectroscopically diverse object was simulated by clipping individual squares out of the logo of the Collaborative Research Center 'Mathematics of Experiment'. Multi-wavelength Fourier transform holography data were then simulated for $N_\tau = N_\lambda = 4$ delay steps, and the multi-wavelength holograms were calculated using a single Fourier transform. Poisson noise equivalent to 4×10^7 photons, i.e. 1×10^7 photons per delay step, was applied to the simulated diffraction patterns. The spectrally resolved reconstructed images clearly reproduce the distinct logos.

Chapter 7

Summary

The combination of HHG illumination with CDI marks the beginning of a new era in nanoscale imaging. After decades of continuous development, from early experiments relying on large-scale synchrotron facilities to today's compact tabletop HHG sources, CDI is evolving from a proof-of-concept technique into a practical imaging tool. HHG-CDI systems offer exceptional flexibility, low cost, compact footprint, and simple architecture, while moving closer to meeting the demands of next-generation nanoscale imaging: high resolution, aberration-free imaging, non-destructive and non-contact operation, high efficiency, 3D reconstruction, and dynamic imaging. Furthermore, these systems enable chemical composition and concentration mapping of samples. As a result, HHG-CDI techniques are beginning to find real-world applications in both scientific research and industrial settings, particularly in semiconductor inspection. In this thesis, we have explored and advanced the field of coherent EUV imaging through the development and application of tabletop HHG sources, ptychographic techniques, and Fourier transform holographic methodologies. Our work provides important steps towards high-resolution, material-sensitive, and spectrally resolved imaging for applications in materials science, nanotechnology, and semiconductor metrology.

Chapter 2 starts with an overview of the construction and optimization of tabletop HHG-based EUV sources. A detailed experimental setup is described, including high-intensity femtosecond laser systems, nonlinear post-compression techniques, and a vacuum-compatible EUV beamline. We emphasized the challenges in maintaining high brightness and stability in HHG sources, which are critical for achieving high-fidelity ptychographic reconstructions. We then introduce the fundamentals of ptychographic algorithms as robust solutions to the phase problem in lensless imaging and describe the key components of the experimental setup, with particular focus on diffraction pattern acquisition in both transmission and reflection geometries.

In Chapter 3, we demonstrate efficient post-compression of 2 mJ, 170 fs Yb-ion-doped laser pulses to 37 fs with over 90% flux efficiency, while maintaining good beam quality. This simple double-pass-based post-compression implementation enables significant spectral broadening via self-phase modulation, while effectively suppressing self-focusing and preserving favorable scaling toward higher pulse energies. SHG-FROG and PWFS measurements characterized the pulses in both time and space, revealing nonlinear effects and spatiotemporal aberrations at specific wavelengths. These findings highlight

the importance of wavelength-resolved diagnostics and demonstrate that CASCADE post-compression offers a simple, efficient, and scalable solution for high-flux HHG applications.

Chapter 4 then focused on the demonstration of broadband ptychographic imaging using spatially diverse, multi-wavelength illumination. We show that polychromatic illumination typically considered a challenge for coherent imaging can be transformed into an advantage through information multiplexing. By introducing structured and multi-wavelength illumination, we showed how the robustness and resolution of reconstructions can be significantly improved. The concept of Fisher information analysis was applied to quantify the sensitivity of the ptychographic inverse problem to variations in probe diversity, establishing a formal link between spatial mode structure and reconstruction fidelity. Our results show that structured illumination enables the separation of spectral components within a single diffraction pattern while also maximizing added information from each new scan positions. Our work can be anticipated as a starting point for high-fidelity polychromatic imaging of next-generation nanostructured devices at EUV and soft-X-ray wavelengths.

In Chapter 5, we characterize the structure and composition of a three-element spiral-shaped object in transmission using multi-wavelength diffractive shearing interferometry, as well as single-wavelength structured-illumination ptychography. We find that both methods are capable of retrieving element-resolved spatial images as well as local layer composition. DSI, based on Fourier-transform spectroscopy, enables spectrally resolved measurements and is naturally suited for multiwavelength analysis. In contrast, ptychography provides a robust framework for quantitative imaging by reconstructing both the amplitude and phase of the exit wave at a fixed wavelength. Future integration of both techniques, such as multiwavelength ptychography driven by temporally delayed HHG pulse pairs, could yield full spectrally resolved phase and amplitude information. Overall, this work demonstrates that EUV ptychography, in particular, offers a powerful and non-destructive tool for high-resolution, material-specific imaging, which is well-suited for advanced applications in nanolithography, semiconductor inspection, and multilayer thin film metrology.

In Chapter 6, we introduced Fourier Transform Spectroscopic Holography (FTSH), a novel and compact spectro-microscopic imaging technique that enables rapid acquisition of spatially and spectrally resolved information in the EUV regime. By applying a designed holographic mask into the phase-locking HHG pulse pairs, we minimize the number of required Fourier transform spectroscopy measurements. Specifically, we identified two optimized sampling strategies: (i) using the number of spectral components as the minimal number of sampling points, and (ii) further reducing this requirement by incorporating prior knowledge of the spectral overlap in the recorded holograms. The number of required measurements was reduced to 6, representing about an order of magnitude fewer compared to conventional Nyquist-limited sampling. FTSH thus presents a powerful solution for fast, table-top EUV spectromicroscopy and holds particular promise for time-resolved studies, where both high resolution and rapid acquisition are essential for tracking dynamic nanoscale processes.

Bibliography

[1] G. E. Moore, *Cramming more components onto integrated circuits*, Proceedings of the IEEE **86**, 82–85 (1998).

[2] R. Peeters, S. Lok, E. van Alphen, N. Harned, P. Kuerz, M. Lowisch, et al., *ASML's NXE platform performance and volume introduction*, in Extreme ultraviolet (euv) lithography iv, Vol. 8679 (International Society for Optics and Photonics, 2013), 86791F.

[3] E. Abbe, *Beiträge zur theorie des mikroskops und der mikroskopischen wahrnehmung*, Archiv für mikroskopische Anatomie **9**, 413–468 (1873).

[4] H. Lee, L.-E. Yu, S.-W. Ryu, J.-W. Han, K. Jeon, et al., *Sub-5nm all-around gate finfet for ultimate scaling*, in 2006 symposium on vlsi technology, 2006. digest of technical papers. (2006), pages 58–59.

[5] W. M. Arden, *The international technology roadmap for semiconductors- perspectives and challenges for the next 15 years*, Curr. Opin. Solid State Mater. Sci. **6**, 371–377 (2002).

[6] R. Paschotta, *Numerical aperture*, RP Photonics Encyclopedia, Available online at `https://www.rp-photonics.com/numerical_aperture.html`, 2005.

[7] W. T. Welford, *Aberrations of optical systems* (Routledge, 2017).

[8] P. V. Parimi, W. T. Lu, P. Vodo, and S. Sridhar, *Imaging by flat lens using negative refraction*, Nature **426**, 404–404 (2003).

[9] A. Shadfan, M. Pawlowski, Y. Wang, K. Subramanian, I. Gabay, A. Ben-Yakar, and T. Tkaczyk, *Design and fabrication of a miniature objective consisting of high refractive index zinc sulfide lenses for laser surgery*, Opt. Eng. **55**, 025107 (2016).

[10] P. Horowitz and J. A. Howell, *A scanning x-ray microscope using synchrotron radiation*, Science **178**, 608–611 (1972).

[11] S. W. Hell and J. Wichmann, *Breaking the diffraction resolution limit by stimulated emission: stimulated-emission-depletion fluorescence microscopy*, Opt. Lett. **19**, 780–782 (1994).

[12] E. Betzig, A. Lewis, A. Harootunian, M. Isaacson, and E. Kratschmer, *Near field scanning optical microscopy (nsom): development and biophysical applications*, Biophys. J. **49**, 269–279 (1986).

[13] M. J. Rust, M. Bates, and X. Zhuang, *Sub-diffraction-limit imaging by stochastic optical reconstruction microscopy (storm)*, Nat. Methods. **3**, 793–796 (2006).

[14] W. Denk, J. H. Strickler, and W. W. Webb, *Two-photon laser scanning fluorescence microscopy*, Science **248**, 73–76 (1990).

[15] D. L. Wokosin, V. E. Centonze, S. Crittenden, and J. White, *Three-photon excitation fluorescence imaging of biological specimens using an all-solid-state laser*, Bioimaging **4**, 208–214 (1996).

[16] B. R. Hunt, T. L. Overman, and P. Gough, *Image reconstruction from pairs of fourier-transform magnitude*, Opt. Lett. **23**, 1123–1125 (1998).

[17] J. Miao, P. Charalambous, J. Kirz, and D. Sayre, *Extending the methodology of x-ray crystallography to allow imaging of micrometre-sized non-crystalline specimens*, Nature **400**, 342–344 (1999).

[18] L. Loetgering, S. Witte, and J. Rothhardt, *Advances in laboratory-scale ptychography using high harmonic sources*, Opt. Express **30**, 4133–4164 (2022).

[19] J. Rothhardt and L. Loetgering, "Ultrafast nanoscale imaging with high harmonic sources", in *Structural dynamics with x-ray and electron scattering* (Royal Society of Chemistry, Dec. 2023).

[20] J. Miao, *Computational microscopy with coherent diffractive imaging and ptychography*, Nature **637**, 281–295 (2025).

[21] J. Rothhardt, G. K. Tadesse, W. Eschen, and J. Limpert, *Table-top nanoscale coherent imaging with xuv light*, J. Opt. **20**, 113001 (2018).

[22] W. Eschen, R. Klas, D. S. P. Molina, S. Fuchs, G. G. Paulus, J. Limpert, and J. Rothhardt, *Coherent nanoscale imaging and chemical mapping with compact extreme ultraviolet and soft x-ray sources: review and perspective*, APL Photonics **10**, 050901 (2025).

[23] J. I. Larruquert, "Chapter 7 - optical properties of thin film materials at short wavelengths", in *Optical thin films and coatings (second edition)*, edited by A. Piegari and F. Flory, Second Edition, Woodhead Publishing Series in Electronic and Optical Materials (Woodhead Publishing, 2018), pages 291–356.

[24] R. L. Sandberg, A. Paul, D. A. Raymondson, S. Hädrich, D. M. Gaudiosi, J. Holtsnider, R. I. Tobey, O. Cohen, M. M. Murnane, H. C. Kapteyn, C. Song, J. Miao, Y. Liu, and F. Salmassi, *Lensless diffractive imaging using tabletop coherent high-harmonic soft-x-ray beams*, Phys. Rev. Lett. **99**, 098103 (2007).

[25] H. N. Chapman, A. Barty, M. J. Bogan, S. Boutet, M. Frank, S. P. Hau-Riege, S. Marchesini, B. W. Woods, S. Bajt, W. H. Benner, et al., *Femtosecond diffractive imaging with a soft-x-ray free-electron laser*, Nat. Phys. **2**, 839–843 (2006).

[26] R. Neutze, R. Wouts, D. Van der Spoel, E. Weckert, and J. Hajdu, *Potential for biomolecular imaging with femtosecond x-ray pulses*, Nature **406**, 752–757 (2000).

[27] J. R. Fienup, *Phase retrieval algorithms: a comparison*, Appl. Opt. **21**, 2758–2769 (1982).

[28] J. R. Fienup, *Reconstruction of an object from the modulus of its fourier transform*, Opt. Lett. **3**, 27–29 (1978).

[29] S. Mustafi and T. Latychevskaia, *Fourier transform holography: a lensless imaging technique, its principles and applications*, in Photonics, Vol. 10, 2 (MDPI, 2023), page 153.

[30] V. T. Tenner, K. S. E. Eikema, and S. Witte, *Fourier transform holography with extended references using a coherent ultra-broadband light source*, Opt. Express **22**, 25397–25409 (2014).

[31] O. Kfir, S. Zayko, C. Nolte, M. Sivis, M. Möller, B. Hebler, S. S. P. K. Arekapudi, D. Steil, S. Schäfer, M. Albrecht, O. Cohen, S. Mathias, and C. Ropers, *Nanoscale magnetic imaging using circularly polarized high-harmonic radiation*, Sci. Adv. **3**, eaao4641 (2017).

[32] R. Klas, A. Kirsche, M. Gebhardt, J. Buldt, H. Stark, S. Hädrich, J. Rothhardt, and J. Limpert, *Ultra-short-pulse high-average-power megahertz-repetition-rate coherent extreme-ultraviolet light source*, PhotoniX **2**, 1–8 (2021).

[33] M. Odstrcil, P. Baksh, S. A. Boden, R. Card, J. E. Chad, J. G. Frey, and W. S. Brocklesby, *Ptychographic coherent diffractive imaging with orthogonal probe relaxation*, Opt. Express **24**, 8360–8369 (2016).

[34] P. D. Baksh, M. Ostrčil, M. Miszczak, C. Pooley, R. T. Chapman, A. S. Wyatt, E. Springate, J. E. Chad, K. Deinhardt, J. G. Frey, and W. S. Brocklesby, *Quantitative and correlative extreme ultraviolet coherent imaging of mouse hippocampal neurons at high resolution*, Sci. Adv. **6**, eaaz3025 (2020).

[35] W. Eschen, L. Loetgering, V. Schuster, R. Klas, A. Kirsche, L. Berthold, M. Steinert, T. Pertsch, H. Gross, M. Krause, J. Limpert, and J. Rothhardt, *Material-specific high-resolution table-top extreme ultraviolet microscopy*, Light Sci. Appl. **11**, 117 (2022).

[36] B. Wang, N. J. Brooks, P. Johnsen, N. W. Jenkins, Y. Esashi, I. Binnie, M. Tanksalvala, H. C. Kapteyn, and M. M. Murnane, *High-fidelity ptychographic imaging of highly periodic structures enabled by vortex high harmonic beams*, Optica **10**, 1245–1252 (2023).

[37] A. Pelekanidis, F. Zhang, M. Gouder, J. Seifert, M. Du, K. S. Eikema, and S. Witte, *Illumination diversity in multiwavelength extreme ultraviolet ptychography*, Photonics Res. **12**, 2757–2771 (2024).

[38] P. Thibault and A. Menzel, *Reconstructing state mixtures from diffraction measurements*, Nature **494**, 68–71 (2013).

[39] C. Liu, W. Eschen, L. Loetgering, D. S. Penagos Molina, R. Klas, A. Iliou, M. Steinert, S. Herkersdorf, A. Kirsche, T. Pertsch, et al., *Visualizing the ultra-structure of microorganisms using table-top extreme ultraviolet imaging*, PhotoniX **4**, 6 (2023).

[40] M. W. Jones, K. Elgass, M. D. Junker, M. B. Luu, M. T. Ryan, A. G. Peele, and G. A. Van Riessen, *Mapping biological composition through quantitative phase and absorption x-ray ptychography*, Sci. Rep. **4**, 6796 (2014).

[41] B. Zhang, D. F. Gardner, M. D. Seaberg, E. R. Shanblatt, H. C. Kapteyn, M. M. Murnane, and D. E. Adams, *High contrast 3d imaging of surfaces near the wavelength limit using tabletop euv ptychography*, Ultramicroscopy **158**, 98–104 (2015).

[42] R. M. Karl, G. F. Mancini, J. L. Knobloch, T. D. Frazer, J. N. Hernandez-Charpak, B. Abad, D. F. Gardner, E. R. Shanblatt, M. Tanksalvala, C. L. Porter, C. S. Bevis, D. E. Adams, H. C. Kapteyn, and M. M. Murnane, *Full-field imaging of thermal and acoustic dynamics in an individual nanostructure using tabletop high harmonic beams*, Sci. Adv. **4**, eaau4295 (2018).

[43] M. Tanksalvala, C. L. Porter, Y. Esashi, B. Wang, N. W. Jenkins, Z. Zhang, G. P. Miley, J. L. Knobloch, B. McBennett, N. Horiguchi, et al., *Nondestructive, high-resolution, chemically specific 3d nanostructure characterization using phase-sensitive euv imaging reflectometry*, Sci. Adv. **7**, eabd9667 (2021).

[44] E. R. Shanblatt, C. L. Porter, D. F. Gardner, G. F. Mancini, R. M. Karl Jr, M. D. Tanksalvala, C. S. Bevis, V. H. Vartanian, H. C. Kapteyn, D. E. Adams, et al., *Quantitative chemically specific coherent diffractive imaging of reactions at buried interfaces with few nanometer precision*, Nano Lett. **16**, 5444–5450 (2016).

[45] H. Lu, M. Odstrčil, C. Pooley, J. Biller, M. Mebonia, G. He, M. Praeger, L. Juschkin, J. Frey, and W. Brocklesby, *Characterisation of engineered defects in extreme ultraviolet mirror substrates using lab-scale extreme ultraviolet reflection ptychography*, Ultramicroscopy **249**, 113720 (2023).

[46] D. J. Batey, D. Claus, and J. M. Rodenburg, *Information multiplexing in ptychography*, Ultramicroscopy **138**, 13–21 (2014).

[47] B. Zhang, D. F. Gardner, M. H. Seaberg, E. R. Shanblatt, C. L. Porter, R. Karl, C. A. Mancuso, H. C. Kapteyn, M. M. Murnane, and D. E. Adams, *Ptychographic hyperspectral spectromicroscopy with an extreme ultraviolet high harmonic comb*, Opt. Express **24**, 18745–18754 (2016).

[48] L. Loetgering, X. Liu, A. C. C. D. Beurs, M. Du, G. Kuijper, K. S. E. Eikema, and S. Witte, *Tailoring spatial entropy in extreme ultraviolet focused beams for multispectral ptychography*, Optica **8**, 130–138 (2021).

[49] M. Du, X. Liu, A. Pelekanidis, F. Zhang, L. Loetgering, P. Konold, C. L. Porter, P. Smorenburg, K. S. Eikema, and S. Witte, *High-resolution wavefront sensing and aberration analysis of multi-spectral extreme ultraviolet beams*, Optica **10**, 255–263 (2023).

[50] X. Liu, A. Pelekanidis, M. Du, F. Zhang, K. S. Eikema, and S. Witte, *Observation of chromatic effects in high-order harmonic generation*, Phys. Rev. Res. **5**, 043100 (2023).

[51] A. Pelekanidis, F. Zhang, K. S. Eikema, and S. Witte, *Generation dynamics of broadband extreme ultraviolet vortex beams*, ACS photonics (2025).

[52] Y. Sun, N. Liu, and Y. Cui, *Promises and challenges of nanomaterials for lithium-based rechargeable batteries*, Nat. Energy. **1**, 1–12 (2016).

[53] A. Chatzimpinou, C. Funaya, D. Rogers, S. O'Connor, S. Kapishnikov, P. Sheridan, K. Fahy, and V. Weinhardt, *Dehydration as alternative sample preparation for soft x-ray tomography*, J. Microsc. **291**, 248–255 (2023).

[54] A. Maiden, G. Morrison, B Kaulich, A Gianoncelli, and J. Rodenburg, *Soft x-ray spectromicroscopy using ptychography with randomly phased illumination*, Nat. Commun. **4**, 1669 (2013).

[55] M. Du, L. Loetgering, K. S. Eikema, and S. Witte, *Ptychographic optical coherence tomography*, Opt. Lett. **46**, 1337–1340 (2021).

[56] T. Aidukas, N. W. Phillips, A. Diaz, E. Poghosyan, E. Müller, A. F. Levi, G. Aeppli, M. Guizar-Sicairos, and M. Holler, *High-performance 4-nm-resolution x-ray tomography using burst ptychography*, Nature **632**, 81–88 (2024).

[57] Y. Shao, S. Weerdenburg, J. Seifert, H. P. Urbach, A. P. Mosk, and W. Coene, *Wavelength-multiplexed multi-mode euv reflection ptychography based on automatic differentiation*, Light sci. appl. **13**, 196 (2024).

[58] D. F. Gardner, M. Tanksalvala, E. R. Shanblatt, X. Zhang, B. R. Galloway, C. L. Porter, R. Karl Jr, C. Bevis, D. E. Adams, H. C. Kapteyn, et al., *Subwavelength coherent imaging of periodic samples using a 13.5 nm tabletop high-harmonic light source*, Nat. Photonics **11**, 259–263 (2017).

[59] Z. Dong, M. Huo, J. Li, J. Li, P. Li, H. Sun, L. Gu, Y. Lu, M. Wang, Y. Wang, et al., *Visualization of oxygen vacancies and self-doped ligand holes in la3ni2o7- δ*, Nature **630**, 847–852 (2024).

[60] A. Zong, B. R. Nebgen, S.-C. Lin, J. A. Spies, and M. Zuerch, *Emerging ultrafast techniques for studying quantum materials*, Nat. Rev. Mater. **8**, 224–240 (2023).

[61] L. Loetgering, M. Baluktsian, K. Keskinbora, R. Horstmeyer, T. Wilhein, G. Schütz, K. S. Eikema, and S. Witte, *Generation and characterization of focused helical x-ray beams*, Sci. Adv. **6**, eaax8836 (2020).

[62] M. Ossiander, M. L. Meretska, H. K. Hampel, S. W. D. Lim, N. Knefz, T. Jauk, F. Capasso, and M. Schultze, *Extreme ultraviolet metalens by vacuum guiding*, Science **380**, 59–63 (2023).

[63] R Weissenbilder, S Carlström, L Rego, C Guo, C. Heyl, P Smorenburg, E. Constant, C. Arnold, and A L'huillier, *How to optimize high-order harmonic generation in gases*, Nat. Rev. Phys. **4**, 713–722 (2022).

[64] C. G. Schroer, P. Boye, J. M. Feldkamp, J. Patommel, A. Schropp, A. Schwab, S. Stephan, M. Burghammer, S. Schöder, and C. Riekel, *Coherent x-ray diffraction imaging with nanofocused illumination*, Phys. Rev. Lett. **101**, 090801 (2008).

[65] P Raimondi, N Carmignani, L. Carver, J Chavanne, L Farvacque, G Le Bec, D Martin, S. Liuzzo, T Perron, and S White, *Commissioning of the hybrid multibend achromat lattice at the european synchrotron radiation facility*, Phys. Rev. Accel. Beams. **24**, 110701 (2021).

[66] A McPherson, G Gibson, H Jara, U Johann, T. S. Luk, I. McIntyre, K. Boyer, and C. K. Rhodes, *Studies of multiphoton production of vacuum-ultraviolet radiation in the rare gases*, JOSA B. **4**, 595–601 (1987).

[67] J. L. Krause, K. J. Schafer, and K. C. Kulander, *High-order harmonic generation from atoms and ions in the high intensity regime*, Phys. Rev. Lett. **68**, 3535 (1992).

[68] P. B. Corkum, *Plasma perspective on strong field multiphoton ionization*, Phys. Rev. Lett. **71**, 1994 (1993).

[69] M. V. Ammosov, N. B. Delone, and V. P. Krainov, *Tunnel ionization of complex atoms and atomic ions in electromagnetic field*, High intensity laser processes **664**, 138–141 (1986).

[70] E Constant, D Garzella, P Breger, E Mével, C. Dorrer, C Le Blanc, F Salin, and P Agostini, *Optimizing high harmonic generation in absorbing gases: model and experiment*, Phys. Rev. Lett. **82**, 1668 (1999).

[71] I. J. Kim, C. M. Kim, H. T. Kim, G. H. Lee, Y. S. Lee, J. Y. Park, D. J. Cho, and C. H. Nam, *Highly efficient high-harmonic generation in an orthogonally polarized two-color laser field*, Phys. Rev. Lett. **94**, 243901 (2005).

[72] F. Brizuela, C. Heyl, P. Rudawski, D. Kroon, L. Rading, J. M. Dahlström, J. Mauritsson, P. Johnsson, C. Arnold, and A. L'Huillier, *Efficient high-order harmonic generation boosted by below-threshold harmonics*, Sci. Rep. **3**, 1410 (2013).

[73] C. M. Heyl, H. Coudert-Alteirac, M. Miranda, M. Louisy, K. Kovacs, V. Tosa, E. Balogh, K. Varjú, A. L'Huillier, A. Couairon, and C. L. Arnold, *Scale-invariant nonlinear optics in gases*, Optica **3**, 75–81 (2016).

[74] V. Nefedova, M. Albrecht, M. Kozlová, and J. Nejdl, *Development of a high-flux xuv source based on high-order harmonic generation*, Journal of Electron Spectroscopy and Related Phenomena **220**, Proceedings of the "39th International Conference on Vacuum Ultraviolet and X-ray Physics (VUVX-2016), 9–13 (2017).

[75] P. M. Paul, E. S. Toma, P. Breger, G. Mullot, F. Augé, P. Balcou, H. G. Muller, and P. Agostini, *Observation of a train of attosecond pulses from high harmonic generation*, Science **292**, 1689–1692 (2001).

[76] C. Spielmann, N. H. Burnett, S. Sartania, R. Koppitsch, M. Schnürer, C. Kan, M. Lenzner, P. Wobrauschek, and F. Krausz, *Generation of coherent x-rays in the water window using 5-femtosecond laser pulses*, Science **278**, 661–664 (1997).

[77] J. R. Sutherland, E. L. Christensen, N. D. Powers, S. E. Rhynard, J. C. Painter, and J. Peatross, *High harmonic generation in a semi-infinite gas cell*, Opt. Express **12**, 4430–4436 (2004).

[78] A. Rundquist, C. G. Durfee, Z. Chang, C. Herne, S. Backus, M. M. Murnane, and H. C. Kapteyn, *Phase-matched generation of coherent soft x-rays*, Science **280**, 1412–1415 (1998).

[79] R. A. Bartels, A. Paul, H. Green, H. C. Kapteyn, M. M. Murnane, S. Backus, I. P. Christov, Y. Liu, D. Attwood, and C. Jacobsen, *Generation of spatially coherent light at extreme ultraviolet wavelengths*, Science **297**, 376–378 (2002).

[80] C. M. Heyl, C. L. Arnold, A Couairon, and A L'Huillier, *Introduction to macroscopic power scaling principles for high-order harmonic generation*, J. Phys. B: At. Mol. Opt. Phys. **50**, 013001 (2016).

[81] G. Mourou, *Nobel lecture: extreme light physics and application*, Rev. Mod. Phys. **91**, 030501 (2019).

[82] H. Fattahi, H. G. Barros, M. Gorjan, T. Nubbemeyer, B. Alsaif, C. Y. Teisset, M. Schultze, S. Prinz, M. Haefner, M. Ueffing, et al., *Third-generation femtosecond technology*, Optica **1**, 45–63 (2014).

[83] T. Brabec and F. Krausz, *Intense few-cycle laser fields: frontiers of nonlinear optics*, Rev. Mod. Phys. **72**, 545 (2000).

[84] C. Jauregui, J. Limpert, and A. Tünnermann, *High-power fibre lasers*, Nat. Photonics **7**, 861–867 (2013).

[85] D. Rand, D. Miller, D. J. Ripin, and T. Y. Fan, *Cryogenic yb 3+-doped materials for pulsed solid-state laser applications*, Opt. Mater. Express. **1**, 434–450 (2011).

[86] F. X. Kärtner, *Few-cycle laser pulse generation and its applications* (Springer, 2004).

[87] P. Balla, A. B. Wahid, I. Sytcevich, C. Guo, A.-L. Viotti, L. Silletti, A. Cartella, S. Alisauskas, H. Tavakol, U. Grosse-Wortmann, et al., *Postcompression of picosecond pulses into the few-cycle regime*, Opt. Lett. **45**, 2572–2575 (2020).

[88] A Dubietis, G Jonušauskas, and A Piskarskas, *Powerful femtosecond pulse generation by chirped and stretched pulse parametric amplification in bbo crystal*, Opt. Commun. **88**, 437–440 (1992).

[89] R. Klas, W. Eschen, A. Kirsche, J. Rothhardt, and J. Limpert, *Generation of coherent broadband high photon flux continua in the xuv with a sub-two-cycle fiber laser*, Opt. Express **28**, 6188–6196 (2020).

[90] B. Zhu, Z. Fu, Y. Chen, S. Peng, C. Jin, G. Fan, S. Zhang, S. Wang, H. Ru, C. Tian, et al., *Spatially homogeneous few-cycle compression of Yb lasers via all-solid-state free-space soliton management*, Opt. Express **30**, 2918–2932 (2022).

[91] C. M. Heyl, M. Seidel, E. Escoto, A. Schönberg, S. Carlström, G. Arisholm, T. Lang, and I. Hartl, *High-energy bow tie multi-pass cells for nonlinear spectral broadening applications*, JPhys: Photonics **4**, 014002 (2022).

[92] Y. Pfaff, G. Barbiero, M. Rampp, S. Klingebiel, J. Brons, C. Y. Teisset, H. Wang, R. Jung, J. Jaksic, A. H. Woldegeorgis, et al., *Nonlinear pulse compression of a 200 mJ and 1 kw ultrafast thin-disk amplifier*, Opt. Express **31**, 22740–22756 (2023).

[93] D Herriott, H Kogelnik, and R Kompfner, *Off-axis paths in spherical mirror interferometers*, Appl. Opt. **3**, 523–526 (1964).

[94] A. Viotti, M. Seidel, E. Escoto, S. Rajhans, W. P. Leemans, I. Hartl, and C. M. Heyl, *Multi-pass cells for post-compression of ultrashort laser pulses*, Optica **9**, 197–216 (2022).

[95] M. Tsai, A. Liang, C. Tsai, P. Lai, M. Lin, and M. Chen, *Nonlinear compression toward high-energy single-cycle pulses by cascaded focus and compression*, Sci. Adv. **8**, eabo1945 (2022).

[96] J. W. Goodman, *Introduction to fourier optics* (Roberts and Company publishers, 2005).

[97] S. Marchesini, H. He, H. N. Chapman, S. P. Hau-Riege, A. Noy, M. R. Howells, U. Weierstall, and J. C. H. Spence, *X-ray image reconstruction from a diffraction pattern alone*, Phys. Rev. B **68**, 140101 (2003).

[98] R. Bates, *Uniqueness of solutions to two-dimensional fourier phase problems for localized and positive images*, Computer Vision, Graphics, and Image Processing **25**, 205–217 (1984).

[99] J. M. Rodenburg and H. M. L. Faulkner, *A phase retrieval algorithm for shifting illumination*, Appl. Phys. Lett. **85**, 4795–4797 (2004).

[100] U. Schnars, C. Falldorf, J. Watson, and W. Jüptner, "Fundamental principles of holography", in *Digital holography and wavefront sensing: principles, techniques and applications* (Springer Berlin Heidelberg, Berlin, Heidelberg, 2015), pages 5–38.

[101] G. Taylor, *The phase problem*, Biological Crystallography **59**, 1881–1890 (2003).

[102] R. Bates, *Astronomical speckle imaging*, Phys. Rep. **90**, 203–297 (1982).

[103] D. Sayre, *Some implications of a theorem due to shannon*, Acta Crystallographica **5**, 843–843 (1952).

[104] J. Miao, D. Sayre, and H. Chapman, *Phase retrieval from the magnitude of the fourier transforms of nonperiodic objects*, J. Opt. Soc. Am. A. **15**, 1662–1669 (1998).

[105] R. W. Gerchberg, *A practical algorithm for the determination of phase from image and diffraction plane pictures*, Optik **35**, 237–246 (1972).

[106] M. R. Teague, *Deterministic phase retrieval: a green's function solution*, J. Opt. Soc. Am. **73**, 1434–1441 (1983).

[107] D. R. Luke, *Relaxed averaged alternating reflections for diffraction imaging*, Inverse Probl. **21**, 37 (2004).

[108] V. Elser, I Rankenburg, and P Thibault, *Searching with iterated maps*, PNAS **104**, 418–423 (2007).

[109] J. Rodenburg and A. Maiden, "Ptychography", in *Springer handbook of microscopy*, edited by P. W. Hawkes and J. C. H. Spence (Springer International Publishing, Cham, 2019), pages 819–904.

[110] A. Maiden, D. Johnson, and P. Li, *Further improvements to the ptychographical iterative engine*, Optica **4**, 736–745 (2017).

[111] A. M. Maiden, M. J. Humphry, and J. M. Rodenburg, *Ptychographic transmission microscopy in three dimensions using a multi-slice approach*, J. Opt. Soc. Am. A **29**, 1606–1614 (2012).

[112] G. Zheng, R. Horstmeyer, and C. Yang, *Wide-field, high-resolution fourier ptychographic microscopy*, Nat. Photonics **7**, 739–745 (2013).

[113] W. Eschen, C. Liu, M. Steinert, D. S. P. Molina, T. Siefke, U. D. Zeitner, J. Kaspar, T. Pertsch, J. Limpert, and J. Rothhardt, *Structured illumination ptychography and at-wavelength characterization with an euv diffuser at 13.5 nm wavelength*, Opt. Express **32**, 3480–3491 (2024).

[114] D. S. P. Molina, L. Loetgering, W. Eschen, J. Limpert, and J. Rothhardt, *Broadband ptychography using curved wavefront illumination*, Opt. Express **31**, 26958–26968 (2023).

[115] A. de Beurs, L. Loetgering, M. Herczog, M. Du, K. S. Eikema, and S. Witte, *Apie: an angle calibration algorithm for reflection ptychography*, Opt. Lett. **47**, 1949–1952 (2022).

[116] M. Guizar-Sicairos, M. Holler, A. Diaz, J. Vila-Comamala, O. Bunk, and A. Menzel, *Role of the illumination spatial-frequency spectrum for ptychography*, Phys. Rev. B. **86**, 100103 (2012).

[117] H Niedrig and E. Rau, *Information depth and spatial resolution in bse microtomography in sem*, Nucl. Instrum. Methods Phys. Res., B **142**, 523–534 (1998).

[118] O. Stenzel, *Optical coatings: material aspects in theory and practice*, Springer Series in Surface Sciences (Springer Berlin Heidelberg, 2014).

[119] B. L. Henke, E. M. Gullikson, and J. C. Davis, *X-Ray Interactions: Photoabsorption, Scattering, Transmission, and Reflection at $E = 50$-$30{,}000$ eV, $Z = 1$-92*, Atomic Data and Nuclear Data Tables **54**, 181–342 (1993).

[120] P. Drude, *Zur elektronentheorie der metalle*, Annalen der Physik **306**, 566–613 (1900).

[121] D. Tomboulian, *The experimental methods of soft x-ray spectroscopy and the valence band spectra of the light elements*, Handbuch der Physik **6**, 246–304 (1957).

[122] S. Zayko, O. Kfir, M. Heigl, M. Lohmann, M. Sivis, M. Albrecht, and C. Ropers, *Ultrafast high-harmonic nanoscopy of magnetization dynamics*, Nat. Commun. **12**, 6337 (2021).

[123] G. Jansen, "Wavelength-resolved extreme ultraviolet lensless imaging and metrology", English, PhD-Thesis - Research and graduation internal (Vrije Universiteit Amsterdam, 2020).

[124] T. Ditmire, E. T. Gumbrell, R. A. Smith, J. W. G. Tisch, D. D. Meyerhofer, and M. H. R. Hutchinson, *Spatial coherence measurement of soft x-ray radiation produced by high order harmonic generation*, Phys. Rev. Lett. **77**, 4756–4759 (1996).

[125] R. A. Bartels, A. Paul, H. Green, H. C. Kapteyn, M. M. Murnane, S. Backus, I. P. Christov, Y. Liu, D. Attwood, and C. Jacobsen, *Generation of spatially coherent light at extreme ultraviolet wavelengths*, Science **297**, 376–378 (2002).

[126] R. Röhrich, A. F. Koenderink, S. Witte, and L. Loetgering, *Spatial coherence control and analysis via micromirror-based mixed-state ptychography*, New J. Phys. **23**, 053016 (2021).

[127] Y.-G. Jeong, R. Piccoli, D. Ferachou, V. Cardin, M. Chini, S. Hädrich, J. Limpert, R. Morandotti, F. Légaré, B. E. Schmidt, et al., *Direct compression of 170-fs 50-cycle pulses down to 1.5 cycles with 70% transmission*, Sci. Rep. **8**, 1–6 (2018).

[128] M. Kaumanns, D. Kormin, T. Nubbemeyer, V. Pervak, and S. Karsch, *Spectral broadening of 112 mj, 1.3 ps pulses at 5 khz in a lg 10 multipass cell with compressibility to 37 fs*, Opt. Lett. **46**, 929–932 (2021).

[129] V. S. Staels, E. C. Jarque, D. Carlson, M. Hemmer, H. C. Kapteyn, M. M. Murnane, and J. San Roman, *Numerical investigation of gas-filled multipass cells in the enhanced dispersion regime for clean spectral broadening and pulse compression*, Opt. Express **31**, 18898–18906 (2023).

[130] S. Tóth, R. S. Nagymihály, I. Seres, L. Lehotai, J. Csontos, L. T. Tóth, P. P. Geetha, T. Somoskői, B. Kajla, D. Abt, et al., *Single thin-plate compression of multi-TW laser pulses to 3.9 fs*, Opt. Lett. **48**, 57–60 (2023).

[131] M. Nisoli, S. Stagira, S. De Silvestri, O. Svelto, S Sartania, Z Cheng, M Lenzner, C. Spielmann, and F Krausz, *A novel-high energy pulse compression system: generation of multigigawatt sub-5-fs pulses.* Appl. Phys. B. **65** (1997).

[132] Z Pi, H. Kim, and E Goulielmakis, *Petahertz-scale spectral broadening and few-cycle compression of yb: kgw laser pulses in a pressurized, gas-filled hollow-core fiber*, Opt. Lett. **47**, 5865–5868 (2022).

[133] L. Chou, H. Hung, A. Liu, S. Wu, J. Jang, D. Zhong, H. Hsiao, and S. Chia, *Widely tunable femtosecond sources with continuously tailorable bandwidth enabled by self-phase modulation*, Laser Photonics Rev. **17**, 2200297 (2023).

[134] C. Lu, Y. Tsou, H. Chen, B. Chen, Y. Cheng, S. Yang, M. Chen, C. Hsu, and A. H. Kung, *Generation of intense supercontinuum in condensed media*, Optica **1**, 400–406 (2014).

[135] M. Hanna, F. Guichard, N. Daher, Q. Bournet, X. Délen, and P. Georges, *Nonlinear optics in multipass cells*, Laser Photonics Rev. **15**, 2100220 (2021).

[136] M. Ueffing, S. Reiger, M. Kaumanns, V. Pervak, M. Trubetskov, T. Nubbemeyer, and F. Krausz, *Nonlinear pulse compression in a gas-filled multipass cell*, Opt. Lett. **43**, 2070–2073 (2018).

[137] A. Viotti, C. Li, G. Arisholm, L. Winkelmann, I. Hartl, C. M. Heyl, and M. Seidel, *Few-cycle pulse generation by double-stage hybrid multi-pass multi-plate nonlinear pulse compression*, Opt. Lett. **48**, 984–987 (2023).

[138] S. Goncharov, K. Fritsch, and O. Pronin, *Few-cycle pulse compression and white light generation in cascaded multipass cells*, Opt. Lett. **48**, 147–150 (2023).

[139] M. Du, L. Loetgering, K. S. E. Eikema, and S. Witte, *Measuring laser beam quality, wavefronts, and lens aberrations using ptychography*, Opt. Express **28**, 5022–5034 (2020).

[140] N. Daher, F. Guichard, S. W. Jolly, X. Délen, F. Quéré, M. Hanna, and P. Georges, *Multipass cells: 1d numerical model and investigation of spatio-spectral couplings at high nonlinearity*, JOSA B. **37**, 993–999 (2020).

[141] S. A. Akhmanov, A. P. Sukhorukov, and R. V. Khokhlov, *Self-focusing and diffraction of light in a nonlinear medium*, Soviet physics USPEKHI **10**, 609 (1968).

[142] R. W. Boyd, S. G. Lukishova, and Y. R. Shen, *Self-focusing: past and present: fundamentals and prospects* (Springer, 2009).

[143] E. Nibbering, G Grillon, M. A. Franco, B. Prade, and A. Mysyrowicz, *Determination of the inertial contribution to the nonlinear refractive index of air, n 2, and o 2 by use of unfocused high-intensity femtosecond laser pulses*, JOSA B **14**, 650–660 (1997).

[144] M. Shaw, C. Hooker, and D. Wilson, *Measurement of the nonlinear refractive index of air and other gases at 248 nm*, Opt. Commun. **103**, 153–160 (1993).

[145] D. Shelton, *Nonlinear-optical susceptibilities of gases measured at 1064 and 1319 nm*, Phys. Rev. A. **42**, 2578 (1990).

[146] M Mlejnek, E. Wright, and J. Moloney, *Femtosecond pulse propagation in argon: a pressure dependence study*, Phys. Rev. E. **58**, 4903 (1998).

[147] G. P. Agrawal, *Nonlinear fiber optics*, 5th (Elsevier, 2013), pages 615–617.

[148] R. W. Boyd, A. L. Gaeta, and E. Giese, "Nonlinear optics", in *Springer handbook of atomic, molecular, and optical physics* (Springer, 2008), pages 1097–1110.

[149] J. D. Schmidt, *Numerical simulation of optical wave propagation with examples in matlab* (Spie, 2010).

[150] L. Silletti, A. Bin Wahid, E. Escoto, P. Balla, S. Rajhans, K. Horn, L. Winkelmann, V. Wanie, A. Trabattoni, C. M. Heyl, and F. Calegari, *Dispersion-engineered multipass cell for single-stage post-compression of an ytterbium laser*, Opt. Lett. **48**, 1842 (2023).

[151] M. Benner, M. Karst, C. Amaya Mendez, H. Stark, and J. Limpert, *Concept of enhanced frequency chirping for multi-pass cells to improve the pulse contrast*, JOSA B. **40**, 301 (2023).

[152] C. Y. Hémonnot and S. Köster, *Imaging of biological materials and cells by x-ray scattering and diffraction*, ACS nano **11**, 8542–8559 (2017).

[153] C. Porter et al., *Soft x-ray: novel metrology for 3d profilometry and device pitch overlay*, in Metrology, inspection, and process control xxxvii, Vol. 12496 (SPIE, 2023), pages 412–420.

[154] E. Abbe, *Beiträge zur theorie des mikroskops und der mikroskopischen wahrnehmung*, Archiv für mikroskopische Anatomie **9**, 413–468 (1873).

[155] M. Lewenstein, P. Balcou, M. Y. Ivanov, A. L'huillier, and P. B. Corkum, *Theory of high-harmonic generation by low-frequency laser fields*, Phys. Rev. A. **49**, 2117 (1994).

[156] R. A. Bartels, A. Paul, H. Green, H. C. Kapteyn, M. M. Murnane, S. Backus, I. P. Christov, Y. Liu, D. Attwood, and C. Jacobsen, *Generation of spatially coherent light at extreme ultraviolet wavelengths*, Science **297**, 376–378 (2002).

[157] K. Varju, P. Johnsson, J. Mauritsson, A. L'Huillier, and R. Lopez-Martens, *Physics of attosecond pulses produced via high harmonic generation*, American Journal of Physics **77**, 389–395 (2009).

[158] T. Popmintchev, M.-C. Chen, D. Popmintchev, P. Arpin, S. Brown, S. Ališauskas, G. Andriukaitis, T. Balčiunas, O. D. Mücke, A. Pugzlys, A. Baltuška, B. Shim, S. E. Schrauth, A. Gaeta, C. Hernández-García, L. Plaja, A. Becker, A. Jaron-Becker, M. M. Murnane, and H. C. Kapteyn, *Bright coherent ultrahigh harmonics in the kev x-ray regime from mid-infrared femtosecond lasers*, Science **336**, 1287–1291 (2012).

[159] I. Pupeza, C. Zhang, M. Högner, and J. Ye, *Extreme-ultraviolet frequency combs for precision metrology and attosecond science*, Nat. Photonics **15**, 175–186 (2021).

[160] J. Rodenburg, A. Hurst, and A. Cullis, *Transmission microscopy without lenses for objects of unlimited size*, Ultramicroscopy **107**, 227–231 (2007).

[161] M. D. Seaberg, B. Zhang, D. F. Gardner, E. R. Shanblatt, M. M. Murnane, H. C. Kapteyn, and D. E. Adams, *Tabletop nanometer extreme ultraviolet imaging in an extended reflection mode using coherent fresnel ptychography*, Optica **1**, 39–44 (2014).

[162] P. D. Baksh, M. Odstrčil, H.-S. Kim, S. A. Boden, J. G. Frey, and W. S. Brocklesby, *Wide-field broadband extreme ultraviolet transmission ptychography using a high-harmonic source*, Opt. Lett. **41**, 1317–1320 (2016).

[163] W. Eschen, C. Liu, D. S. P. Molina, R. Klas, J. Limpert, and J. Rothhardt, *High-speed and wide-field nanoscale table-top ptychographic euv imaging and beam characterization with a scmos detector*, Opt. Express **31**, 14212–14224 (2023).

[164] G. K. Tadesse, W. Eschen, R. Klas, M. Tschernajew, F. Tuitje, M. Steinert, M. Zilk, V. Schuster, M. Zürch, T. Pertsch, C. Spielmann, J. Limpert, and J. Rothhardt, *Wavelength-scale ptychographic coherent diffractive imaging using a high-order harmonic source*, Scientific Rep. **9**, 1735 (2019).

[165] H. Lu, M. Odstrčil, C. Pooley, J. Biller, M. Mebonia, G. He, M. Praeger, L. Juschkin, J. Frey, and W. Brocklesby, *Characterisation of engineered defects in extreme ultraviolet mirror substrates using lab-scale extreme ultraviolet reflection ptychography*, Ultramicroscopy **249**, 113720 (2023).

[166] P. Thibault, M. Dierolf, A. Menzel, O. Bunk, C. David, and F. Pfeiffer, *High-resolution scanning x-ray diffraction microscopy*, Science **321**, 379–382 (2008).

[167] A. Vila-Comamala Joan Diaz, M. Guizar-Sicairos, A. Mantion, C. M. Kewish, A. Menzel, O. Bunk, and C. David, *Characterization of high-resolution diffractive x-ray optics by ptychographic coherent diffractive imaging*, Opt. Express **19**, 21333–21344 (2011).

[168] Y. Yao, Y. Jiang, J. Klug, Y. Nashed, C. Roehrig, C. Preissner, F. Marin, M. Wojcik, O. Cossairt, and Z. Cai, *Broadband x-ray ptychography using multi-wavelength algorithm*, Journal of Synchrotron Radiation **28**, 309–317 (2021).

[169] S. Witte, V. T. Tenner, D. W. Noom, and K. S. Eikema, *Lensless diffractive imaging with ultra-broadband table-top sources: from infrared to extreme-ultraviolet wavelengths*, Light sci. appl. **3**, e163–e163 (2014).

[170] G. S. M. Jansen, A. d. Beurs, X. Liu, K. S. E. Eikema, and S. Witte, *Diffractive shear interferometry for extreme ultraviolet high-resolution lensless imaging*, Opt. Express **26**, 12479–12489 (2018).

[171] A. Rana, J. Zhang, M. Pham, A. Yuan, Y. H. Lo, H. Jiang, S. J. Osher, and J. Miao, *Potential of attosecond coherent diffractive imaging*, Phys. Rev. Lett. **125**, 086101 (2020).

[172] J. Huijts, S. Fernandez, D. Gauthier, M. Kholodtsova, A. Maghraoui, K. Medjoubi, A. Somogyi, W. Boutu, and H. Merdji, *Broadband coherent diffractive imaging*, Nat. Photon. **14**, 618–622 (2020).

[173] A. M. Maiden, J. M. Rodenburg, and M. J. Humphry, *Optical ptychography: a practical implementation with useful resolution*, Opt. Lett. **35**, 2585–2587 (2010).

[174] A. M. Maiden, M. J. Humphry, F. Zhang, and J. M. Rodenburg, *Superresolution imaging via ptychography*, J. Opt. Soc. Am. A **28**, 604–612 (2011).

[175] M. Odstrčil, M. Lebugle, M. Guizar-Sicairos, C. David, and M. Holler, *Towards optimized illumination for high-resolution ptychography*, Opt. Express **27**, 14981–14997 (2019).

[176] X. Ji, X. He, Z. Jiang, Y. Kong, S. Wang, and C. Liu, *Resolution enhancement with highly curved illumination in ptychography*, Appl. Opt. **61**, 10150–10158 (2022).

[177] M. Pancaldi, F. Guzzi, C. S. Bevis, M. Manfredda, J. Barolak, S. Bonetti, I. Bykova, D. De Angelis, G. De Ninno, M. Fanciulli, et al., *High-resolution ptychographic imaging at a seeded free-electron laser source using oam beams*, Optica **11**, 403–411 (2024).

[178] C. Guo, A. Harth, S. Carlström, Y.-C. Cheng, S. Mikaelsson, E. Marsell, C. Heyl, M. Miranda, M. Gisselbrecht, and M. B. Gaarde, *Phase control of attosecond pulses in a train*, J. Phys. B: At. Mol. Opt. Phys. **51**, 034006 (2018).

[179] R. Géneaux, A. Camper, T. Auguste, O. Gobert, J. Caillat, R. Taïeb, and T. Ruchon, *Synthesis and characterization of attosecond light vortices in the extreme ultraviolet*, Nat. Commun. **7**, 12583 (2016).

[180] C. Hernández-García, A. Picón, J. San Román, and L. Plaja, *Attosecond extreme ultraviolet vortices from high-order harmonic generation*, Phys. Rev. Lett. **111**, 083602 (2013).

[181] M Zürch, C Kern, P Hansinger, A Dreischuh, and C. Spielmann, *Strong-field physics with singular light beams*, Nature Physics **8**, 743–746 (2012).

[182] W. Paufler, B. Böning, and S. Fritzsche, *High harmonic generation with laguerre–gaussian beams*, Journal of Optics **21**, 094001 (2019).

[183] G. Gariepy, J. Leach, K. T. Kim, T. J. Hammond, E. Frumker, R. W. Boyd, and P. B. Corkum, *Creating high-harmonic beams with controlled orbital angular momentum*, Phys. Rev. Lett. **113**, 153901 (2014).

[184] L. Rego, K. M. Dorney, N. J. Brooks, Q. L. Nguyen, C.-T. Liao, J. S. Román, D. E. Couch, A. Liu, E. Pisanty, M. Lewenstein, L. Plaja, H. C. Kapteyn, M. M. Murnane, and C. Hernández-García, *Generation of extreme-ultraviolet beams with time-varying orbital angular momentum*, Science **364**, eaaw9486 (2019).

[185] K. M. Dorney, Laura, N. J. Brooks, J. San Román, C.-T. Liao, J. L. Ellis, D. Zusin, C. Gentry, Q. L. Nguyen, J. M. Shaw, A. Picón, L. Plaja, H. C. Kapteyn, M. M. Murnane, and C. Hernández-García, *Controlling the polarization and vortex charge of attosecond high-harmonic beams via simultaneous spin–orbit momentum conservation*, Nat. Photonics **13**, 123–130 (2019).

[186] F Sanson, A. Pandey, F Harms, G Dovillaire, E Baynard, J Demailly, O Guilbaud, B Lucas, O Neveu, M Pittman, et al., *Hartmann wavefront sensor characterization of a high charge vortex beam in the extreme ultraviolet spectral range*, Opt. Lett. **43**, 2780–2783 (2018).

[187] F Sanson, A. Pandey, I Papagiannouli, F Harms, G Dovillaire, E Baynard, J Demailly, O Guilbaud, B Lucas, and O Neveu, *Highly multimodal structure of high topological charge extreme ultraviolet vortex beams*, Opt. Lett. **45**, 4790–4793 (2020).

[188] L. Rego, J. San Román, A. Picón, L. Plaja, and C. Hernández-García, *Nonperturbative twist in the generation of extreme-ultraviolet vortex beams*, Phys. Rev. Lett. **117**, 163202 (2016).

[189] A. K. Pandey, A. de las Heras, T. Larrieu, J. San Román, J. Serrano, L. Plaja, E. Baynard, M. Pittman, G. Dovillaire, and S. Kazamias, *Characterization of extreme ultraviolet vortex beams with a very high topological charge*, ACS Photonics **9**, 944–951 (2022).

[190] Y. Iwasaki, A. G. Kusne, and I. Takeuchi, *Comparison of dissimilarity measures for cluster analysis of x-ray diffraction data from combinatorial libraries*, npj Computational Materials **3**, 1–9 (2017).

[191] L. Freisem, G. S. M. Jansen, D. Rudolf, K. S. E. Eikema, and S. Witte, *Spectrally resolved single-shot wavefront sensing of broadband high-harmonic sources*, Opt. Express **26**, 6860–6871 (2018).

[192] M. Van Heel and M. Schatz, *Fourier shell correlation threshold criteria*, Journal of Structural Biology **151**, 250–262 (2005).

[193] L. Loetgering, M. Du, D. B. Flaes, T. Aidukas, F. Wechsler, D. S. P. Molina, M. Rose, A. Pelekanidis, W. Eschen, J. Hess, T. Wilhein, R. Heintzmann, J. Rothhardt, and S. Witte, *Ptylab.m/py/jl: a cross-platform, open-source inverse modeling toolbox for conventional and fourier ptychography*, Opt. Express **31**, 13763–13797 (2023).

[194] Vortex Photonics, `https://www.vortex-photonics.de/`.

[195] A. M. Maiden and J. M. Rodenburg, *An improved ptychographical phase retrieval algorithm for diffractive imaging*, Ultramicroscopy **109**, 1256–1262 (2009).

[196] O. Bunk, M. Dierolf, S. Kynde, I. Johnson, O. Marti, and F. Pfeiffer, *Influence of the overlap parameter on the convergence of the ptychographical iterative engine*, Ultramicroscopy **108**, 481–487 (2008).

[197] S. M. Kay, *Fundamentals of statistical signal processing: estimation theory*, en (Prentice-Hall, Inc., 1993).

[198] D. Bouchet, S. Rotter, and A. P. Mosk, *Maximum information states for coherent scattering measurements*, en, Nat. Phys. **17**, 564–568 (2021).

[199] D. Bouchet, J. Seifert, and A. P. Mosk, *Optimizing illumination for precise multi-parameter estimations in coherent diffractive imaging*, en, Opt. Lett. **46**, 254–257 (2021).

[200] L. Loetgering, M. Du, K. S. E. Eikema, and S. Witte, *zPIE: an autofocusing algorithm for ptychography*, en, Opt. Lett. **45**, 2030–2033 (2020).

[201] D. Bouchet, J. Dong, D. Maestre, and T. Juffmann, *Fundamental bounds on the precision of classical phase microscopes*, Phys. Rev. Applied **15**, 024047 (2021).

[202] F. Zhang, A. Pelekanidis, M. Du, K. Eikema, and S. Witte, *Nonlinear compression of mj-level pulses via double-pass loose focusing in air*, in The european conference on lasers and electro-optics (Optica Publishing Group, 2023), cf_p_15.

[203] D. Paganin, *Coherent x-ray optics*, 6 (Oxford University Press, USA, 2006).

[204] optix fab, `http://www.optixfab.com/`.

[205] D. Malacara-Hernández and A. Gomez-Vieyra, *Optical design of systems with off-axis spherical mirrors*, in 22nd congress of the international commission for optics: light for the development of the world, Vol. 8011 (SPIE, 2011), pages 298–304.

[206] P. Li, "Investigations and improvements in ptychographic imaging", PhD thesis (University of Sheffield, 2016).

[207] J. M. Rodenburg, *Ptychography and related diffractive imaging methods*, Advances in imaging and electron physics **150**, 87–184 (2008).

[208] H. N. Chapman and K. A. Nugent, *Coherent lensless x-ray imaging*, Nat. Photonics **4**, 833–839 (2010).

[209] F. Pfeiffer, *X-ray ptychography*, Nat. Photonics **12**, 9–17 (2018).

[210] Y. Jiang, Z. Chen, Y. Han, P. Deb, H. Gao, S. Xie, P. Purohit, M. W. Tate, J. Park, S. M. Gruner, et al., *Electron ptychography of 2d materials to deep sub-ångström resolution*, Nature **559**, 343–349 (2018).

[211] W. Yang, H. Sha, J. Cui, L. Mao, and R. Yu, *Local-orbital ptychography for ultrahigh-resolution imaging*, Nature Nanotechnology **19**, 612–617 (2024).

[212] K. X. Nguyen, Y. Jiang, C.-H. Lee, P. Kharel, Y. Zhang, A. M. van der Zande, and P. Y. Huang, *Achieving sub-0.5-angstrom–resolution ptychography in an uncorrected electron microscope*, Science **383**, 865–870 (2024).

[213] A. V. Martin, F. Wang, N.-t. D. Loh, T. Ekeberg, F. R. Maia, M. Hantke, G. van der Schot, C. Y. Hampton, R. G. Sierra, A. Aquila, et al., *Noise-robust coherent diffractive imaging with a single diffraction pattern*, Opt. Express **20**, 16650–16661 (2012).

[214] G. Jansen, A de Beurs, X Liu, K. Eikema, and S Witte, *Diffractive shear interferometry for extreme ultraviolet high-resolution lensless imaging*, Opt. Express **26**, 12479–12489 (2018).

[215] A. C. C. de Beurs, X. Liu, G. S. M. Jansen, A. P. Konijnenberg, W. M. J. Coene, K. S. E. Eikema, and S. Witte, *Extreme ultraviolet lensless imaging without object support through rotational diversity in diffractive shearing interferometry*, Opt. Express **28**, 5257–5266 (2020).

[216] L Freisem, G. Jansen, K. Eikema, and S Witte, *Spectrally resolved single-shot wavefront sensing of broadband high-harmonic sources*, Opt. Express **26**, 6860–6871 (2018).

[217] V. Krasnov, I. Makhotkin, J. E. Scheerder, L. Loetgering, V. Soltwisch, P. A. van der Heide, and C. Fleischmann, *Soft x-ray chemically sensitive ptychographic imaging of 3d nano-objects*, Opt. Express **32**, 43788–43804 (2024).

[218] D. Attwood, *Soft x-rays and extreme ultraviolet radiation: principles and applications* (Cambridge university press, 2000).

[219] J. Kirz, C. Jacobsen, and M. Howells, *Soft x-ray microscopes and their biological applications*, Quarterly reviews of biophysics **28**, 33–130 (1995).

[220] S. Witte, V. T. Tenner, D. W. Noom, and K. S. Eikema, *Lensless diffractive imaging with ultra-broadband table-top sources: from infrared to extreme-ultraviolet wavelengths*, Light Sci. Appl. **3**, e163–e163 (2014).

[221] G. Jansen, K. Eikema, and S Witte, *Spatially resolved fourier transform spectroscopy in the extreme ultraviolet*, Optica **3**, 1122–1125 (2016).

[222] D. R. Austin, T. Witting, C. A. Arrell, F. Frank, A. S. Wyatt, J. P. Marangos, J. W. Tisch, and I. A. Walmsley, *Lateral shearing interferometry of high-harmonic wavefronts*, Opt. Lett. **36**, 1746–1748 (2011).

[223] C. Falldorf, C. von Kopylow, and R. B. Bergmann, *Wave field sensing by means of computational shear interferometry*, J. Opt. Soc. Am. A. **30**, 1905–1912 (2013).

[224] M. Riley and M. Gusinow, *Laser beam divergence utilizing a lateral shearing interferometer*, Appl. Opt. **16**, 2753–2756 (1977).

[225] A. P. Konijnenberg, A. C. C. de Beurs, G. S. M. Jansen, H. P. Urbach, S. Witte, and W. M. J. Coene, *Phase retrieval algorithms for lensless imaging using diffractive shearing interferometry*, J. Opt. Soc. Am. A **37**, 914–924 (2020).

[226] M. S. Wartak, *Computational photonics: an introduction with matlab* (Cambridge University Press, 2013).

[227] A. Pelekanidis, K. S. E. Eikema, and S. Witte, *Far-field optical propagators with user-defined object-plane pixel size for ptychography*, Opt. Continuum **4**, 804–825 (2025).

[228] F. Zhang, A. Pelekanidis, A. Karpavicius, M. Gouder, J. Seifert, K. Eikema, and S. Witte, *Characterizing post-compression of mj-level ultrafast pulses via loose focusing in a gas cell*, Opt. Express **32**, 40990–41003 (2024).

[229] R. A. Bartels, A. Paul, H. Green, H. C. Kapteyn, M. M. Murnane, S. Backus, I. P. Christov, Y. Liu, D. Attwood, and C. Jacobsen, *Generation of spatially coherent light at extreme ultraviolet wavelengths*, Science **297**, 376–378 (2002).

[230] F. Zhang, M. Gouder, A. Pelekanidis, K. S. Eikema, and S. M. Witte, *Wavelength-resolved ptychographic imaging using high-harmonic generation pulse pairs*, in Computational optics 2024 (SPIE, 2024), PC1302307.

[231] B. L. Henke, E. M. Gullikson, and J. C. Davis, *X-ray interactions: photoabsorption, scattering, transmission, and reflection at e= 50-30,000 ev, z= 1-92*, Atomic data and nuclear data tables **54**, 181–342 (1993).

[232] F. Krausz and M. Ivanov, *Attosecond physics*, Rev. Mod. Phys. **81**, 163 (2009).

[233] R. Battistelli, D. Metternich, M. Schneider, L.-M. Kern, K. Litzius, J. Fuchs, C. Klose, K. Gerlinger, K. Bagschik, C. M. Günther, D. Engel, C. Ropers, S. Eisebitt, B. Pfau, F. Büttner, and S. Zayko, *Coherent x-ray magnetic imaging with 5 nm resolution*, Optica **11**, 234 (2024).

[234] M. D. Seaberg, D. E. Adams, E. L. Townsend, D. A. Raymondson, W. F. Schlotter, Y. Liu, C. S. Menoni, L. Rong, C.-C. Chen, J. Miao, H. C. Kapteyn, and M. M. Murnane, *Ultrahigh 22 nm resolution coherent diffractive imaging using a desktop 13 nm high harmonic source*, Opt. Express **19**, 22470–22479 (2011).

[235] M. Schultze, K. Ramasesha, C. Pemmaraju, S. Sato, D. Whitmore, A. Gandman, J. S. Prell, L. J. Borja, D. Prendergast, K. Yabana, D. M. Neumark, and S. R. Leone, *Attosecond band-gap dynamics in silicon*, Science **346**, 1348–1352 (2014).

[236] F. Siegrist, J. A. Gessner, M. Ossiander, C. Denker, Y.-P. Chang, M. C. Schröder, A. Guggenmos, Y. Cui, J. Walowski, U. Martens, J. K. Dewhurst, U. Kleineberg, M. Münzenberg, S. Sharma, and M. Schultze, *Light-wave dynamic control of magnetism*, Nature **571**, 240–244 (2019).

[237] R. Geneaux, H. J. B. Marroux, A. Guggenmos, D. M. Neumark, and S. R. Leone, *Transient absorption spectroscopy using high harmonic generation: a review of ultrafast X-ray dynamics in molecules and solids*, Philos. Transact. A Math. Phys. Eng. Sci. **377**, 20170463 (2019).

[238] E. de Vos, S. Neb, A. Niedermayr, F. Burri, M. Hollm, L. Gallmann, and U. Keller, *Ultrafast Transition from State-Blocking Dynamics to Electron Localization in Transition Metal β-Tungsten*, Phys. Rev. Lett. **131**, 226901 (2023).

[239] T. Heinrich, H.-T. Chang, S. Zayko, K. Rossnagel, M. Sivis, and C. Ropers, *Electronic and Structural Fingerprints of Charge-Density-Wave Excitations in Extreme Ultraviolet Transient Absorption Spectroscopy*, Phys. Rev. X **13**, 021033 (2023).

[240] C. Möller, H. Probst, G. S. M. Jansen, M. Schumacher, M. Brede, J. K. Dewhurst, M. Reutzel, D. Steil, S. Sharma, and S. Mathias, *Verification of ultrafast spin transfer effects in iron-nickel alloys*, Commun. Phys. **7**, 1–6 (2024).

[241] H. Probst, C. Möller, M. Schumacher, T. Brede, J. K. Dewhurst, M. Reutzel, D. Steil, S. Sharma, G. S. M. Jansen, and S. Mathias, *Unraveling femtosecond spin and charge dynamics with extreme ultraviolet transverse MOKE spectroscopy*, Phys. Rev. Res. **6**, 013107 (2024).

[242] A. S. Johnson, J. V. Conesa, L. Vidas, D. Perez-Salinas, C. M. Günther, B. Pfau, K. A. Hallman, R. F. Haglund, S. Eisebitt, and S. Wall, *Quantitative hyperspectral coherent diffractive imaging spectroscopy of a solid-state phase transition in vanadium dioxide*, Sci. Adv. **7**, eabf1386 (2021).

[243] A. S. Johnson, D. Perez-Salinas, K. M. Siddiqui, S. Kim, S. Choi, K. Volckaert, P. E. Majchrzak, S. Ulstrup, N. Agarwal, K. Hallman, R. F. Haglund, C. M. Günther, B. Pfau, S. Eisebitt, D. Backes, F. Maccherozzi, A. Fitzpatrick, S. S. Dhesi, P. Gargiani, M. Valvidares, N. Artrith, F. de Groot, H. Choi, D. Jang, A. Katoch, S. Kwon, S. H. Park, H. Kim, and S. E. Wall, *Ultrafast X-ray imaging of the light-induced phase transition in VO_2*, Nat. Phys. **19**, 215–220 (2023).

[244] I. McNulty, J. Kirz, C. Jacobsen, E. H. Anderson, M. R. Howells, and D. P. Kern, *High-Resolution Imaging by Fourier Transform X-ray Holography*, Science **256**, 1009–1012 (1992).

[245] H. He, U. Weierstall, J. C. H. Spence, M. Howells, H. A. Padmore, S. Marchesini, and H. N. Chapman, *Use of extended and prepared reference objects in experimental Fourier transform x-ray holography*, Appl. Phys. Lett. **85**, 2454–2456 (2004).

[246] S. Marchesini, S. Boutet, A. E. Sakdinawat, M. J. Bogan, S. Bajt, A. Barty, H. N. Chapman, M. Frank, S. P. Hau-Riege, A. Szöke, C. Cui, D. A. Shapiro, M. R. Howells, J. C. H. Spence, J. W. Shaevitz, J. Y. Lee, J. Hajdu, and M. M. Seibert, *Massively parallel X-ray holography*, Nat. Photon. **2**, 560–563 (2008).

[247] J. Geilhufe, B. Pfau, C. M. Günther, M. Schneider, and S. Eisebitt, *Achieving diffraction-limited resolution in soft-X-ray Fourier-transform holography*, Ultramicroscopy **214**, 113005 (2020).

[248] W. Eschen, S. Wang, C. Liu, R. Klas, M. Steinert, S. Yulin, H. Meißner, M. Bussmann, T. Pertsch, J. Limpert, and J. Rothhardt, *Towards attosecond imaging at the nanoscale using broadband holography-assisted coherent imaging in the extreme ultraviolet*, Commun. Phys. **4**, 1–7 (2021).

[249] P. Thibault, M. Dierolf, A. Menzel, O. Bunk, C. David, and F. Pfeiffer, *High-Resolution Scanning X-ray Diffraction Microscopy*, Science **321**, 379–382 (2008).

[250] A. Rana, J. Zhang, M. Pham, A. Yuan, Y. Lo, H. Jiang, S. J. Osher, and J. Miao, *Potential of Attosecond Coherent Diffractive Imaging*, Phys. Rev. Lett. **125**, 086101 (2020).

[251] D. Descamps, C. Lyngå, J. Norin, A. L'Huillier, C.-G. Wahlström, J.-F. Hergott, H. Merdji, P. Salières, M. Bellini, and T. W. Hänsch, *Extreme ultraviolet interferometry measurements with high-order harmonics*, Opt. Lett. **25**, 135–137 (2000).

[252] M. Kovačev, S. V. Fomichev, E. Priori, Y. Mairesse, H. Merdji, P. Monchicourt, P. Breger, J. Norin, A. Persson, A. L'Huillier, C.-G. Wahlström, B. Carré, and P. Salières, *Extreme Ultraviolet Fourier-Transform Spectroscopy with High Order Harmonics*, Phys. Rev. Lett. **95**, 223903 (2005).

[253] G. S. M. Jansen, D. Rudolf, L. Freisem, K. S. E. Eikema, and S. Witte, *Spatially resolved Fourier transform spectroscopy in the extreme ultraviolet*, Optica **3**, 1122–1125 (2016).

[254] Y. Meng, C. Zhang, C. Marceau, A. Y. Naumov, P. B. Corkum, and D. M. Villeneuve, *Octave-spanning hyperspectral coherent diffractive imaging in the extreme ultraviolet range*, Opt. Express **23**, 28960–28969 (2015).

[255] G. S. M. Jansen, A. C. C. d. Beurs, X. Liu, K. S. E. Eikema, and S. Witte, *Diffractive shear interferometry for extreme ultraviolet high-resolution lensless imaging*, Opt. Express **26**, 12479–12489 (2018).

[256] G. O. Williams, A. I. Gonzalez, S. Künzel, L. Li, M. Lozano, E. Oliva, B. Iwan, S. Daboussi, W. Boutu, H. Merdji, M. Fajardo, and P. Zeitoun, *Fourier transform holography with high harmonic spectra for attosecond imaging applications*, Opt. Lett. **40**, 3205–3208 (2015).

[257] S. G. Kalenkov, G. S. Kalenkov, and A. E. Shtanko, *Hyperspectral holography: an alternative application of the Fourier transform spectrometer*, JOSA B **34**, B49–B55 (2017).

[258] A. Genco, C. Cruciano, M. Corti, K. E. McGhee, B. Ardini, L. Sortino, L. Hüttenhofer, T. Virgili, D. G. Lidzey, S. A. Maier, A. Bassi, G. Valentini, G. Cerullo, and C. Manzoni, *K-Space Hyperspectral Imaging by a Birefringent Common-Path Interferometer*, ACS Photonics **9**, 3563–3572 (2022).

[259] D. Brida, C. Manzoni, and G. Cerullo, *Phase-locked pulses for two-dimensional spectroscopy by a birefringent delay line*, Opt. Lett. **37**, 3027–3029 (2012).

[260] M.-S. Tsai, A.-Y. Liang, C.-L. Tsai, P.-W. Lai, M.-W. Lin, and M.-C. Chen, *Nonlinear compression toward high-energy single-cycle pulses by cascaded focus and compression*, Sci. Adv. **8**, eabo1945 (2022).

[261] M. Hanke, *Regularizing properties of a truncated newton-cg algorithm for nonlinear inverse problems*, Numer. Funct. Anal. Optim. **18**, 971–993 (1997).

[262] S. Maretzke, M. Bartels, M. Krenkel, T. Salditt, and T. Hohage, *Regularized newton methods for x-ray phase contrast and general imaging problems*, Opt. Express **24**, 6490–6506 (2016).

[263] F. Capotondi, E. Pedersoli, M. Kiskinova, A. Martin, M. Barthelmess, and H. N. Chapman, *A scheme for lensless x-ray microscopy combining coherent diffraction imaging and differential corner holography*, Opt. Express **20**, 25152–25160 (2012).

[264] A. Descloux, K. S. Grußmayer, and A. Radenovic, *Parameter-free image resolution estimation based on decorrelation analysis*, Nat. Methods. **16**, 918–924 (2019).

[265] *CRC 1456 / LiveDocs / RG - EUV spectroscopic imaging · GitLab*, en, `https://gitlab.gwdg.de/crc1456/livedocs/rg-euv-spectroscopic-imaging`, June 2024.

[266] Z. Chang, A. Rundquist, H. Wang, I. Christov, H. C. Kapteyn, and M. M. Murnane, *Temporal phase control of soft-x-ray harmonic emission*, Phys. Rev. A **58**, R30–R33 (1998).

[267] H. J. Shin, D. G. Lee, Y. H. Cha, J.-H. Kim, K. H. Hong, and C. H. Nam, *Nonadiabatic blueshift of high-order harmonics from Ar and Ne atoms in an intense femtosecond laser field*, Phys. Rev. A **63**, 053407 (2001).

[268] Y. Meng, C. Zhang, C. Marceau, A. Y. Naumov, P. B. Corkum, and D. M. Villeneuve, *Interferometric time delay correction for Fourier transform spectroscopy in the extreme ultraviolet*, J. Mod. Opt. **63**, 1661–1667 (2016).

List of Publications

Chapter 3

F. Zhang, A. Pelekanidis, A. Karpavicius, M. Gouder, J. Seifert, K. S. E. Eikema, and S. Witte, *Characterizing post-compression of mJ-level ultrafast pulses via loose focusing in a gas cell*, Opt. Express **32**, 40990-41003 (2024).

Chapter 4

A. Pelekanidis*, **F. Zhang***, M. Gouder, J. Seifert, M. Du, K. S. E. Eikema, and S. Witte, *Illumination diversity in multiwavelength extreme ultraviolet ptychography*, Photon. Res. **12**, 2757-2771 (2024).

* These authors contributed equally.

Chapter 5

F. Zhang, X. Liu, A. Pelekanidis, M. Gouder, K. S. E. Eikema, and S. Witte, *Material-resolved and thickness-sensitive lensless imaging using high-harmonic generation: from diffractive shear interferometry to ptychography*, *submitted*.

Chapter 6

H. C. Strauch, **F. Zhang**, S. Mathias, T. Hohage, S. Witte, and G. S. M. Jansen, *Fast spectroscopic imaging using extreme ultraviolet interferometry*, Opt. Express **32**, 28644-28654 (2024).

The author has also contributed to the following publication:

A. Pelekanidis, **F. Zhang**, K. S. E. Eikema, and S. Witte, *Generation Dynamics of Broadband Extreme Ultraviolet Vortex Beams*, ACS. Photonics **12**, 1638-1649 (2025).

X. Liu, A. Pelekanidis, M. Du, **F. Zhang**, K. S. E. Eikema, and S. Witte, *Observation of chromatic effects in high-order harmonic generation*, Phys. Rev. Research **5**, 043100 (2023).

M. Du, X. Liu, A. Pelekanidis, **F. Zhang**, L. Loetgering, P. Konold, C. L. Porter, P. Smorenburg, K. S. E. Eikema, and S. Witte, *High-resolution wavefront sensing and aberration analysis of multi-spectral extreme ultraviolet beams*, Optica **10**, 255-263 (2023).